Utrecht University

Koninklijk Nederlands Meteorologisch Instituut
Ministerie van Infrastructuur en Waterstaat

Rotation and divergence biases between scatterometer wind observations and model fields

Faculty of Science

Master Thesis

Utrecht University & KNMI

Climate Physics

Jelle Steenge

Student Nr.: 6526497

Supervisors:

Dr. R.H. Giesen
KNMI

Dr. A. Stoffelen
KNMI

Dr. M.L.J. Baatsen
IMAU

Prof. Dr. M.R. van den Broeke
IMAU

July 9, 2024

Abstract

Many atmospheric processes can be characterized by the rotation and divergence of the surface wind field. An accurate portrayal of these phenomena is very important for numerical weather prediction. This project focused on the global and regional model bias between the rotation and divergence of near-surface ocean wind observations, measured by satellite scatterometers, and numerical model fields of the European Center for Medium-range Weather Forecasting operational model (ECMWF-Ops) for the year 2022. The observations of two different scatterometer types are used over a total of five satellites: ASCAT (MetOp-B and -C) and HSCAT (HY-2B, -2C and -2D).

On global and yearly time scales, modelled wind convergence is weaker than convergence found in the observations. Also, the bias in the wind rotation is minor, less than 10 % of the mean values. However, on some occasions, regional biases are significant.

Turbulent island wakes are one of the features that show a significant bias in wind rotation, with an overestimation in strength for the modelled wake near Madagascar and a slightly different orientation for the modelled wakes of Hawaii, which are most likely caused by smoothing of the island topography in ECMWF-Ops.

The gap wind in South Mexico, the Tehuano Wind, is well represented in ECMWF-Ops, both in the wind divergence and rotation, resulting in no significant biases. Yet, the gap winds near Hawaii show a positive bias in the divergence fields as well as the wind vector field, likely a result of the much smaller scale of the gaps with respect to the Tehuano Wind.

The most significant bias in the wind rotation is located over the Gulf Stream in the Western North Atlantic. Here, ASCAT wind observations show a dual curl-band over the Gulf Stream, with negative rotations on the west-side and positive rotations on the east-side. These rotations, caused by the surface winds responding to large sea surface temperature gradients, are not seen in the model fields, resulting in a large bias. This demonstrates that ECMWF-Ops does not fully resolve air-sea coupling at smaller scales.

Overall, HSCAT observations correlate better with ECMWF-Ops compared to ASCAT observations. Correlations are stronger at mid-latitudes and over significant weather phenomena, otherwise they are highly variable.

Finally, it is demonstrated that an extra interpolation step in the collocated model data results in a little more smoothing of the fields, but to no significant changes. Simultaneously, the necessity of collocation of the model fields with the observations is demonstrated using the temporal mean of the complete ECMWF-Ops dataset.

Cover figure: Artist's impression of ESA's Meteorological operational Satellite series. [ESA/AOES Medialab]

Contents

1 Introduction **1**
1.1 General circulation . . . 2
1.1.1 Atmospheric circulation . . . 2
1.1.2 Ocean circulation . . . 3
1.2 Divergence and rotation . . . 5
1.3 Turbulent fluid dynamics . . . 6
1.3.1 Turbulent wakes and vortices . . . 7
1.4 Weather patterns and phenomena . . . 8
1.4.1 Mountain-gap winds . . . 8
1.4.2 Fronts and depressions . . . 9
1.4.3 Air-sea interactions and SST-surface wind coupling . . . 10
1.5 Satellite measurements and scatterometers . . . 11
1.5.1 Polar satellites . . . 11
1.5.2 Scatterometers . . . 11
1.5.3 Relevant satellites . . . 12
1.5.4 Recent scatterometer research . . . 14
1.6 Numerical weather prediction models . . . 15

2 Project objectives **16**
2.1 Biases in the curl and divergence . . . 16
2.2 Causes of these biases . . . 16
2.3 Summary . . . 17

3 Data and methods **18**
3.1 Data . . . 18
3.1.1 Scatterometer data products . . . 18
3.1.2 Data processing and model collocation . . . 19
3.1.3 SST datasets . . . 20
3.1.4 ETOPO . . . 20
3.1.5 Additional ECMWF-Ops data . . . 20
3.2 Methods . . . 21
3.2.1 Region and time range selection . . . 21
3.2.2 Statistics and bias calculation . . . 22
3.2.3 Data processing . . . 24

4 Results **25**
4.1 Global bias . . . 25
4.1.1 Zonal means . . . 25
4.1.2 Temporal mean and eddy flow . . . 26
4.2 Temporal correlations . . . 30
4.3 Case: North Madagascar . . . 31
4.3.1 General patterns . . . 32
4.4 Case: South of Mexico . . . 33

4.4.1 General patterns . . . 33
4.4.2 Specific coordinate analysis . . . 33
4.4.3 SST: Coastal upwelling . . . 36
4.5 Case: Hawaii . . . 38
4.5.1 General patterns . . . 38
4.5.2 Specific coordinate analysis . . . 40
4.5.3 Model Topography . . . 42
4.6 Case: The Western North Atlantic . . . 44
4.6.1 General patterns . . . 44
4.6.2 Specific coordinate analysis . . . 46
4.6.3 SST: air-sea coupling . . . 46
4.7 Interpolation analysis . . . 51

5 Discussion **54**
5.1 Limitations . . . 54
5.2 Further research . . . 55

6 Conclusions **56**

Bibliography **I**

A Global distributions **IV**

B Regional yearly mean rotation fields **VI**

C Western North Atlantic: Valid data points **VIII**

D Western North Atlantic: SST-gradient **IX**

1 Introduction

Accurate knowledge of the surface winds is important for understanding many processes, as they transport heat, momentum, moisture and myriads of chemical compounds around the globe. Surface winds also play a significant role in many ocean processes, as it influences the mass, momentum and energy fluxes between the ocean and the lower atmosphere.

The general patterns of the surface winds include the eastward trade winds around the equator and the westerlies at mid-latitudes, and are relatively well understood. They drive the main ocean currents and are responsible for the Earth's climate. Yet, surface winds also show a very large variability in space and time. Weather phenomena like fronts, (extra)tropical cyclones or (turbulent) flows due to topography are just a few examples of the changeability of the surface winds.

To accurately make a weather forecast, intricate knowledge of the surface winds is needed. Yet due to their variability in space and time, Numerical Weather Prediction (NWP) models sometimes fail to accurately predict surface winds, which can cause various problems for society. A prime example is the the flood of Venice in November 2019, where a combination of extreme high tides (Aqua Alta) and an approaching storm resulted in the water level reaching 1.89 m, flooding over 50% of the city. [Cavaleri et al., 2020] The official forecast created by the European Center for Medium-range Weather Forecasts (ECMWF) made an underestimation in the water level of almost 40 cm, resulting in the city not being as prepared as necessary. [von Schuckmann et al., 2021]

In the past, wind observations over the vast oceans were only done by buoys, which are few and far between, or ships, which move over time. Luckily, in recent times, satellites have been able to accurately measure the ocean surface winds using scatterometers, which send radar waves to the surface and measure the backscatter resulting from capillary waves on the sea surface.

These satellite data can be used to evaluate the NWP-models, indicating where the biases in the surface winds are largest (and thus where the model is weakest). This information can then be used to improve and calibrate the forecast models, which would certainly help in the prediction of extreme weather events, such as the Venice Floods. Therefore, in this research, the biases in rotation and divergence of the near-surface ocean winds will be studied for various regions which show interesting wind phenomena. The aim of this project is twofold: first, to study the bias in the rotation and divergence of the surface wind for the different regions and second, to try and understand why these biases occur.

The regions of interest for this study are diverse, but all show pronounced and specific patterns in the wind vorticity and divergence. The first feature focuses on the patterns of wind wakes behind mountainous islands, with Hawaii and Madagascar as main examples. Furthermore, this research focuses on the patterns of mountain-gap winds, specifically the Mexican Tehuano Wind. The last process of focus for this study is the interaction between the ocean and atmosphere near western boundary currents, focusing on the Gulf Stream.

This chapter will introduce the necessary theory and processes to get a basic understanding of all the wind dynamics involved in this study. Furthermore, the fundamentals of satellite observations, scatterometers and NWP-models will also be presented.

1.1 General circulation

1.1.1 Atmospheric circulation

The global wind patterns and atmospheric circulation are extensively studied and thus well understood. It's main drivers are the uneven heating of the Earth's surface and its rotation, but the land-sea distribution and differences in heat capacity of land and sea also play a role.

The global wind patterns are divided into the Hadley, Ferrel and polar cells (Fig. 2). The Hadley cells are a closed circulation loop that can be found around the equator on either side of the Intertropical Convergence Zone (ITCZ). Here, the solar irradiation is most intense, causing the Earth's surface to heat up. The moist air near the surface warms, decreases its density and starts to rise, creating a low pressure zone. The rising air is then transported poleward, cooling down in the process. Around 30° latitude, the cooled down air starts to descend, creating a high pressure area near the surface. The descended air is then transported back towards the ITCZ (equatorwards) along the surface.

Due to the rotation of the Earth, fluids are deflected by the Coriolis acceleration. On the Northern Hemisphere (NH), the deflection is to the right, while on the Southern Hemisphere (SH), the deflection is to the left. Southward moving surface air is thus deflected westwards while northward moving air is deflected eastwards. These two processes together create the trade winds, the dominant surface winds in this region, blowing from the northeast on the NH and from the southwest on the SH. Note that the ITCZ moves with the seasons, being just north of the equator during NH summer and south of the equator during NH winter.

The polar cell is very similar to the Hadley cell. At 60° latitude convection occurs and surface air rises. It is then transported poleward, where the air mass is cooled from above by radiation loss to space. The cooled air descends, creating a cold high pressure area around the

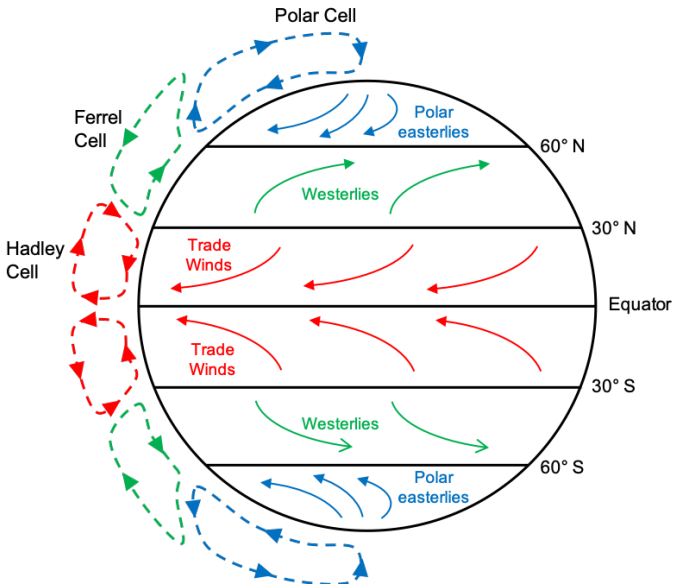

Figure 2: Schematic overview of the global atmospheric circulation.

poles. The air then moves equatorward along the surface, whilst being deflected westward due to the Coriolis acceleration (these are known as polar easterlies), until it reaches 60° latitude and starts to rise again, completing the cell.

The Ferrel cell is located between 30° and 60° on both hemispheres. It is driven by the divergence of rising air at the 60° latitude which travels equatorward until it collides with the high-level air of the Hadley cell at 30° and descends. Near the surface, the air is transported poleward again whilst being deflected eastward by the Coriolis acceleration, creating the westerlies, blowing from the southwest on the NH and from the northwest on the SH. The Ferrel cells are relatively weak, being forced by the stronger Hadley and polar cells on either side, since it has neither a strong source of heat nor a sink. As such, the westerlies are only a prevailing wind and can be disrupted, while the trade winds (and polar easterlies) are a much more dominant feature. [Dunlop, 2017]

1.1.2 Ocean circulation

The global ocean circulation can be divided into two main components: the dynamic wind-driven surface circulation (Fig. 3) and the slow density-driven deep circulation, also known as the thermohaline circulation (Fig. 4). Both currents are superimposed, with the wind-driven currents feeding the deep-water currents at the poles, where net cooling or evaporation of seawater increases its density and starts to sink. This initiates a slow convection where the cold and dense deep seawater is transported equatorward with a speed of about 1 cm/s. Slow upwelling of the deep seawater occurs mainly in the Pacific and Indian Oceans.

The surface currents are mainly wind-driven. As such, they largely follow the same patterns of the surface winds from the general atmospheric circulation. The main features are the eastward equatorial currents, the West Wind drift around Antarctica (also known as the Antarctic Circumpolar Current) and subtropical gyres. These gyres are driven by the trade winds and the westerlies. They rotate clockwise (anticlockwise) on the NH (SH), such that the poleward flow of these gyres is always on the west-side of the basin. These currents are thus known as western boundary currents (WBC's). WBC's (flow speed $O(1)$ m/s) are much stronger than their eastern counterparts ($O(0.1)$ m/s), because they function as a return flow of the net equatorward (Sverdrup) transport of seawater which is spread out over most of the gyre. (WBC's are formed on the west-side of the basin because of the conservation of relative vorticity over the whole basin). WBC's transport warm seawater from the equator northward near the western boundary of the ocean. [Cenedese and Gordon, 2024]

The Gulf Stream in the North Atlantic is arguably the strongest WBC, with an average near-surface flow speed of 2.5 m/s. It is located just off the east coast of the United States (US) in North America. The high sea surface temperature (SST) of the Gulf Stream compared to the surrounding ocean has major impacts on the air-sea interactions of the North Atlantic and the climate on the surrounding continents, especially Western Europe. There, it results in much milder winters than one would expect compared to other regions at similar latitudes.

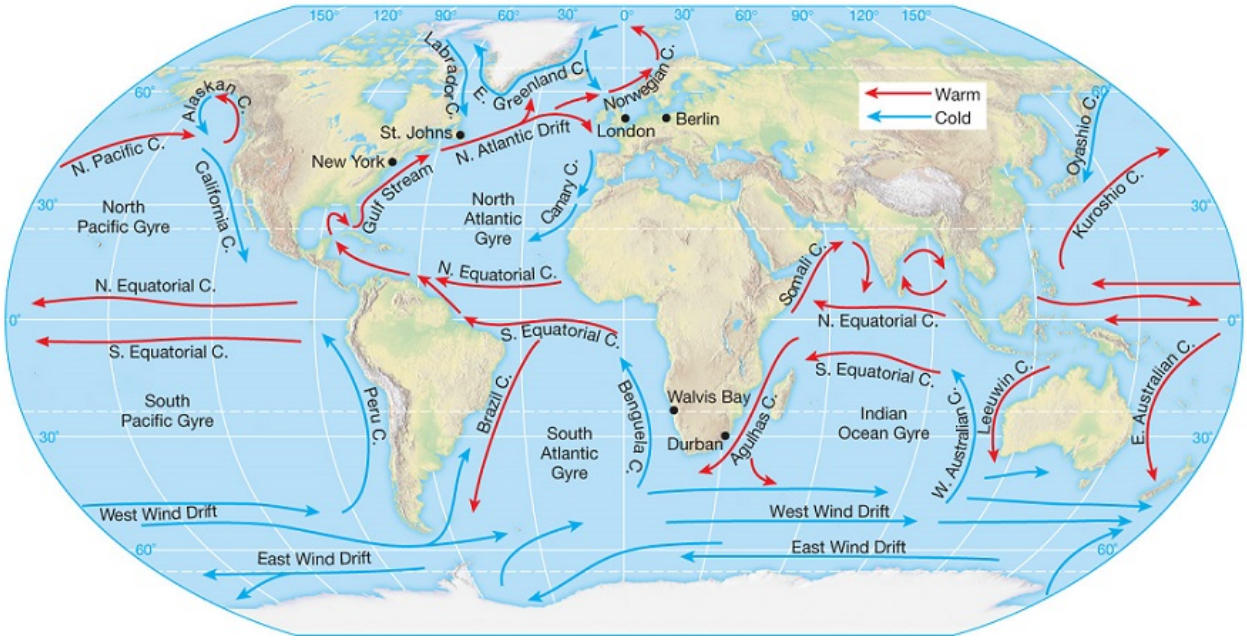

Figure 3: Overview of the main wind-driven ocean currents. [Offshore123, 2021]

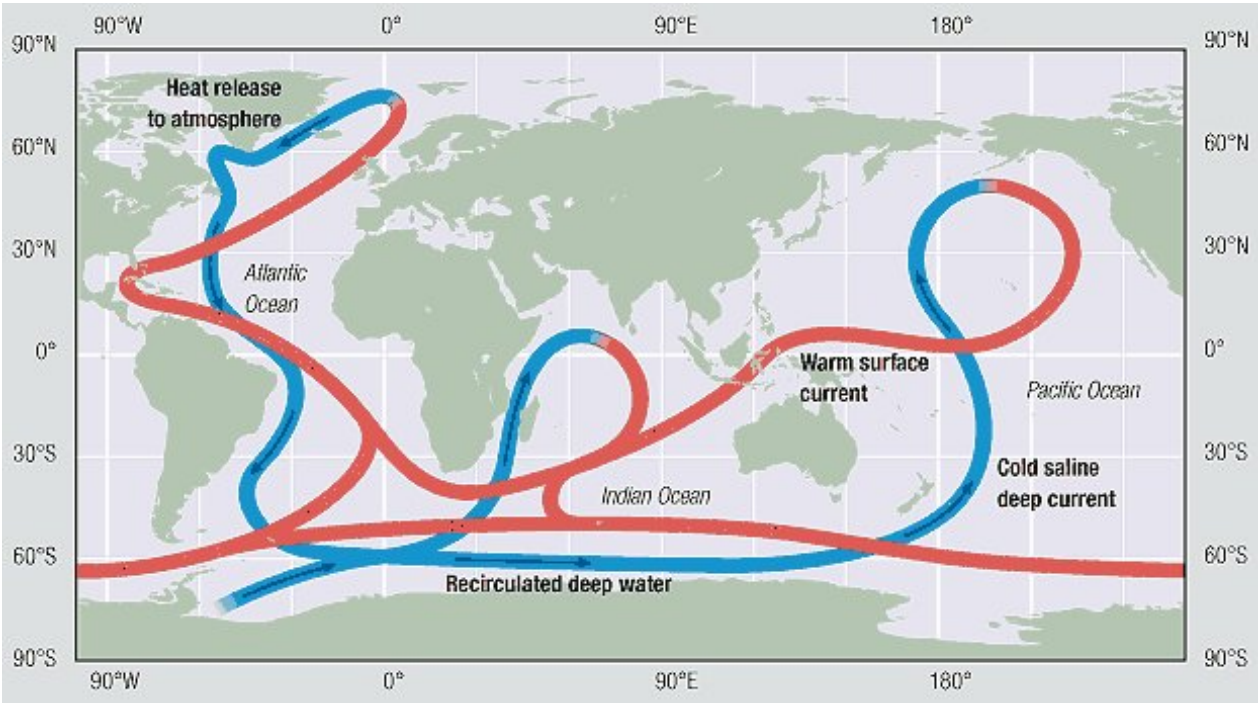

Figure 4: Schematic representation of the thermohaline circulation. The blue current is the dense deep-water current, while the red current is part of the wind-driven surface current. [Tange, 2020]

1.2 Divergence and rotation

This study focuses on both the divergence and rotation of the near-surface wind field. The main reason for this is that divergence and rotation are important indicators of various meteorological and atmospheric processes. Another reason is that the divergence and rotation of the wind field are not as extensively studied as the wind field itself.

- **Divergence**
  The horizontal divergence of a vector field is defined as

$$\nabla \cdot \boldsymbol{U}(x,y) = \frac{\partial u}{\partial x} + \frac{\partial v}{\partial y}, \tag{1}$$

  where $\boldsymbol{U}(x,y) = (u(x,y), v(x,y))$ indicates the vector wind field, of which u and v are the zonal (x-direction) and meridional (y-direction) components.

  Divergence ($\nabla \cdot \boldsymbol{U} > 0$) and convergence ($\nabla \cdot \boldsymbol{U} < 0$) of surface winds are coupled with pressure gradients and temperature. They are an indicator of how much mass flows into a certain area (Fig. 5a).
  When there is a net divergence or outflow of the surface wind, more mass leaves a certain area in the horizontal plane than it enters. Using the conservation of mass, one can quickly see that this outflow of surface air needs to be supplied by the descent of air from the higher atmospheric layers. Positive divergence thus is an indicator of descending air or a high pressure area.
  The opposite is true for convergence: in this case, there is a net inflow of mass over the surface, the accumulating air can move nowhere but up and thus starts to lift. Convergence (or negative divergence) thus indicates rising air and low pressure areas (Fig. 5d).

- **Rotation**
  Horizontal curl (also known as wind rotation or vorticity) is defined as

$$\nabla \times \boldsymbol{U}(x,y) = \left(\frac{\partial v}{\partial x} - \frac{\partial u}{\partial y} \right) \hat{\boldsymbol{z}}. \tag{2}$$

  The result of this equation is a vector, which is oriented perpendicular to the wind vector field (and in the case of a horizontal wind field, the surface).
  It indicates whether a circulation or rotation is present in the vector field (Fig. 5b). A positive curl ($\nabla \times \boldsymbol{U} > 0$, vector pointing upward) indicates an anticlockwise rotation of a vector field while a negative curl ($\nabla \times \boldsymbol{U} < 0$) indicates a clockwise rotation.

Both the curl and divergence of the surface wind field indicate important meteorological phenomena. An important example is the cyclonic winds around an atmospheric low pressure area (Fig. 5c). In geostrophic conditions, the pressure gradient force is balanced by the the Coriolis force, causing air to flow anticlockwise around the low pressure area, making it a pure rotation. But due to surface wind drag, the winds get deflected towards the center of the low pressure system, adding a (negative) divergence as well. (So, an atmospheric low pressure system on the NH consists of a negative divergence and positive rotation.) Other examples which either contain a strong rotation or divergence or both include tropical cyclones, weather fronts, topography-induced turbulence etc.

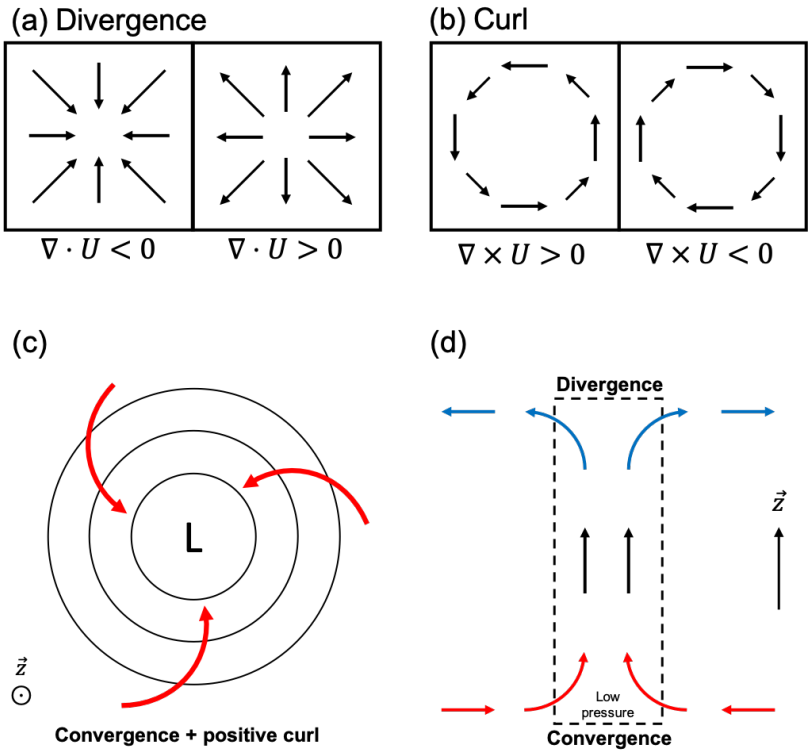

Figure 5: Standard vector field for divergence (a) and rotation (b) as well as a meteorological example of a low pressure system on the NH, as seen in the horizontal plane (c) and the vertical plane (d).

1.3 Turbulent fluid dynamics

The motion of fluids is very complicated to describe, since it consists of the interactions of billions of different molecules that can move (more or less) independent of each other. The intricacies of fluid dynamics are largely outside of the scope of this study. The essentials about about how the Earth's topography affects the near surface winds, however, need to be addressed.

Two types of flow can be distinguished, laminar and turbulent flow. The nature of the flow is determined by the Reynolds number, which is the ratio between inertial forces and viscous forces within a fluid. The Reynolds number (Re) is defined as

$$Re = \frac{UL}{\nu} = \frac{\rho UL}{\mu}, \tag{3}$$

where U is the flow speed of the fluid, L the characteristic length or dimension and $\nu = \frac{\mu}{\rho}$ the kinematic viscosity, defined as the dynamic viscosity, μ, divided by the fluid density, ρ.

For laminar flows (Fig. 6a), the viscous forces dominate over the inertial forces, resulting in a smooth and constant fluid motion. A low Reynolds number ($Re < 1$) indicates a laminar flow.
For a turbulent flow (Fig. 6b/c), indicated by a large Reynolds number, the inertial forces

dominate the viscous forces, which result in the formation of eddies, vortices and other chaotic flow instabilities.

1.3.1 Turbulent wakes and vortices

When an object is placed in a steady fluid flow, the fluid is forced to flow around it. In a laminar flow regime, the fluid just bends around the object. The viscous forces are stronger than the inertial forces, keeping the fluid flowing as one while mitigating the deceleration of the flow bending around the object due to friction forces. For fluids with a low viscosity or with a high flow speed, such as air, a turbulent flow regime is predominant. The fluid flowing around the object is slowed down due to friction, creating a shear in the fluid, due to different flow velocities within the fluid. This shear creates a pressure gradient, resulting in a reverse flow just behind the object and the subsequent formation of a vortex or eddy, where the flow moves in a chaotic circular motion.

The von Kármán vortex street (Fig. 6c) is a special case of a turbulent wake. It can be formed behind (relatively) symmetric blunt objects, such as a cylinder. The vortex street is created by a process known as vortex shedding, where low-pressure vortices are created behind the object periodically from either side, before shedding and being transported downstream, creating a chain of vortices.

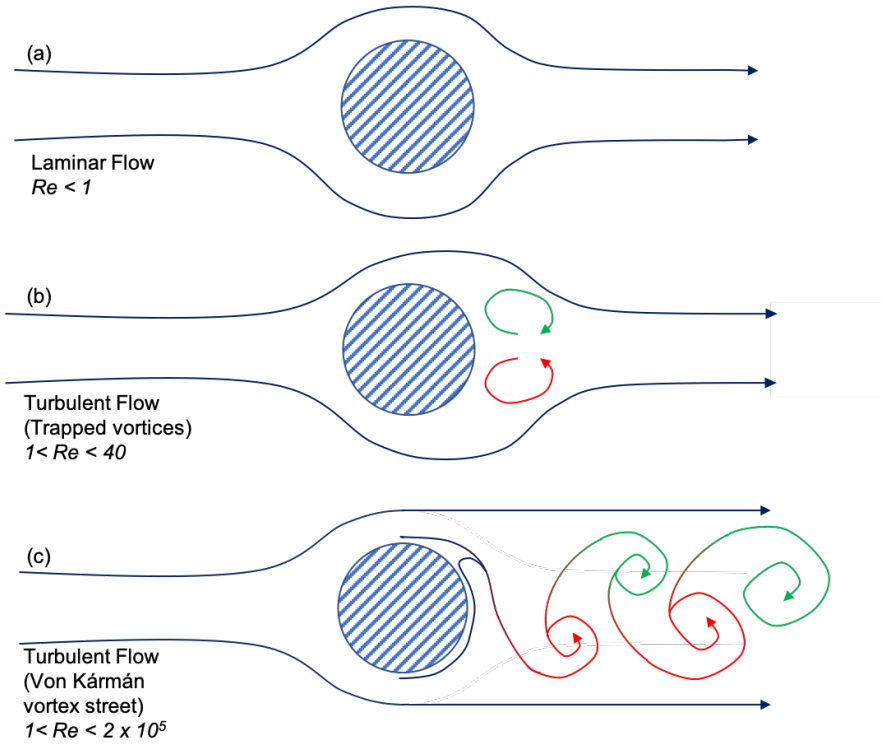

Figure 6: Schematic representation of different fluid flow types: laminar (a), trapped turbulence (b) and von Kármán vortices (c). The colors of the vortices indicate a positive (red) and negative (green) rotation.

In atmospheric dynamics, turbulent wakes and vortex streets are most common behind lone mountains or islands in the middle of the ocean, like the Hawaiian Archipelago, which is a focus area for this study.

1.4 Weather patterns and phenomena

To fully understand and interpret the motions of the near-surface ocean wind, a general understanding of some common weather patterns and phenomena is necessary. For the Gulf Stream region, this mainly involves a basic understanding of fronts and depressions.

1.4.1 Mountain-gap winds

An important weather phenomenon for this study is the mountain-gap wind, specifically the gap wind located near the Gulf of Tehuantepec near the South Coast of Mexico, called the Tehuano Wind by locals (Fig. 7).

The Tehuano Wind is formed when cold air outbreaks over the Great Plains of the US trigger air pressure differences that flow southward over Eastern Mexico and the Gulf of Mexico. This creates a high pressure area north of the Sierra Madre Mountains with lower pressures over the subtropical Pacific Ocean, the air is forced through the narrow Chivela Pass, accelerating and focusing the wind like a jet to speeds in excess of 20 m/s.

The gap wind can extend over hundreds of kilometers into the Pacific Ocean, pushing the surface water away from the coast, resulting in the upwelling of cold and nutrient-rich waters from the deep ocean, creating an ideal fish habitat. Locals have used the Tehuano Winds and the resulting nutrient-rich waters to catch fish for hundreds of years. [Smith, 2015]

The Tehuano Wind is most common between October and February, with minimal occurrences in July.

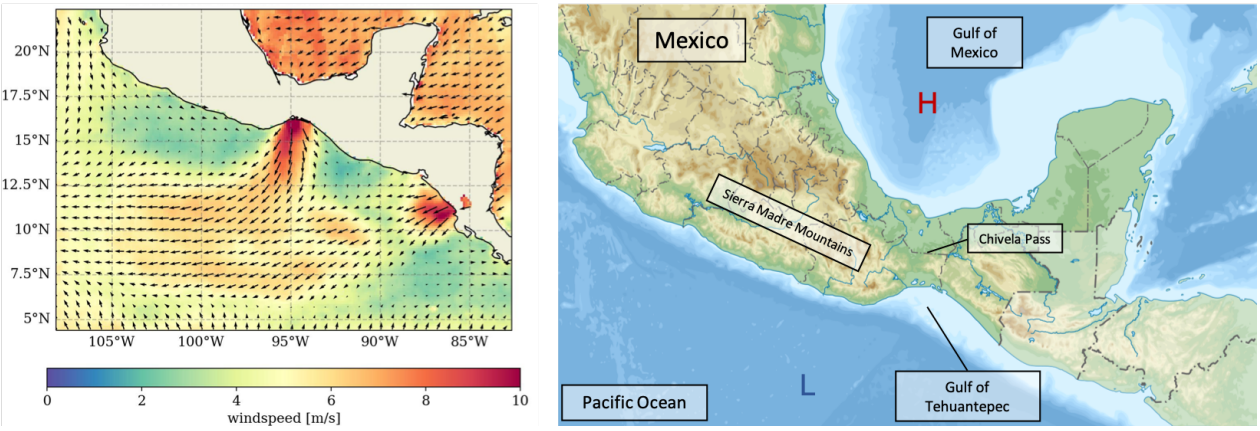

Figure 7: Left: The monthly mean wind field of January 2022, measured by MetOp-B and C. The Tehuano wind is clearly visible just south of the Chivela Pass. Right: Topographical map of the South of Mexico.

1.4.2 Fronts and depressions

At temperate latitudes, the most significant changes in temperature, humidity, rainfall or wind speed and direction are caused by the passage of fronts or depressions. Depressions are low-pressure systems, and are more formally known as extra-tropical cyclones. They are the end product of the cyclogenesis process, developing from a combination of fronts.

A front is a boundary between two air masses with significantly different temperatures and humidities. There are three different types of fronts: warm, cold and occluded. With a warm front, the warm air mass is advancing on the cold air mass (Fig. 8, bottom). The warm air moves over the cold air and creates a wide band of precipitation along the frontal zone. For a cold front, the cold air mass advances on the warm air mass, undercutting the warm air mass and pushing it up, creating a band of convective clouds with heavy rainfall (Fig. 8, top). An occluded front is formed when a cold front overtakes a warm front. Depending on which air mass is the coldest, either a warm occluded or cold occluded front is formed. When practically the whole warm front is overtaken by the cold front, the occluded front starts to decay. The central pressure increases and the depression is fully formed. [Dunlop, 2017]

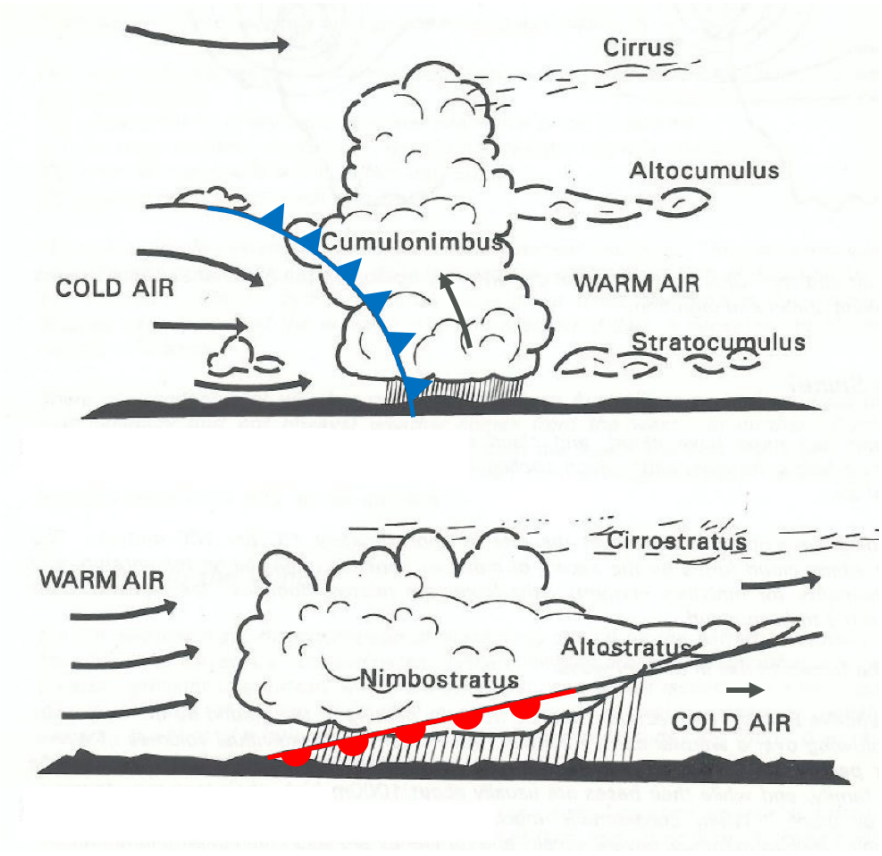

Figure 8: Schematic representation of a cold (top) and warm front (bottom), the symbols point in the direction the front is moving. [BoM-AG, 2021]

1.4.3 Air-sea interactions and SST-surface wind coupling

The air-sea interface is an interface between two fluids with different densities and viscosities. Over this interface friction creates a shear, and different forms of energy are exchanged. Kinetic energy from the air is transported into the sea, for example through the formation of waves and currents, while in some situations, the ocean exchanges heat with the atmosphere, altering its flow pattern. The exchange in kinetic energy and the formation of waves and currents is universal and happens nearly anywhere at the air-sea interface. Outside of the tropical regions, where tropical cyclones are generated, a strong atmospheric effect of the heat exchange between the atmosphere and the ocean happens only in places where the SST gradient is significant. This is mainly the case near the WBC's, where the focus of this research shall lie on the Gulf Stream.

The horizontal gradient in the SST (T) is defined as

$$Grad(T) = \nabla T = \left(\frac{\partial T}{\partial x}, \frac{\partial T}{\partial y} \right). \tag{4}$$

The SST-gradient is a vector and indicates the rate of change in the SST in the zonal ($\frac{\partial T}{\partial x}$) and meridional ($\frac{\partial T}{\partial y}$) directions.

The mechanism behind the SST-wind coupling can be summarized as a stability-adjustment of the marine atmospheric boundary layer. The SST influences the near-surface air density,

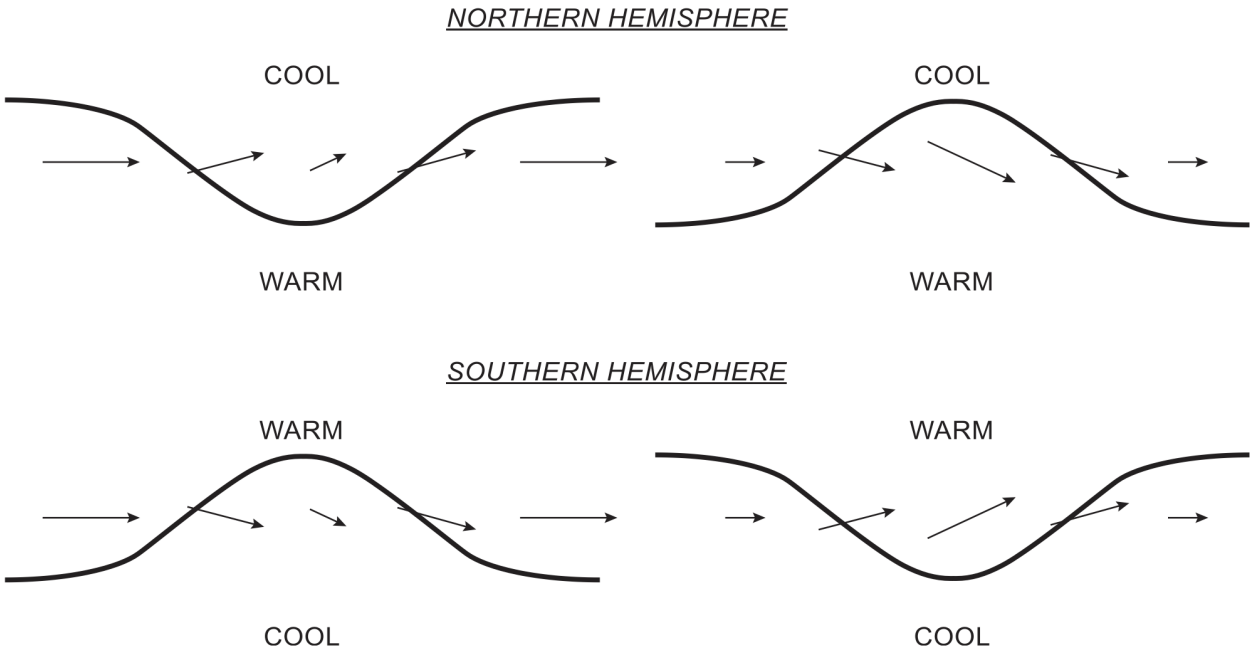

Figure 9: Schematic of the wind vector response to an SST front for the NH and SH. The solid curves indicate an SST-front (strong SST-gradient) while the vectors represent the surface winds. [O'Neill et al., 2010]

with higher (lower) densities over colder (warmer) parts of the ocean. This in turn induces pressure gradients to which the surface winds respond. On the Northern Hemisphere, the winds decelerate and undergo a positive rotation when they pass over an SST-front from warmer to cooler waters. When they pass from cooler waters to warmer waters, the surface winds accelerate and undergo a negative rotation. On the SH the rotations switch sign, but the effects on the wind speed remains the same. [O'Neill et al., 2010]

1.5 Satellite measurements and scatterometers

In the present day, most observations of the Earth's atmosphere and ocean are made by satellites. Satellites are kept in orbit around the Earth because the centripetal force on the satellite balances the gravitational force that the Earth exerts on the satellite. There are several different types of orbits. For example, for geostationary orbits, the satellite's orbital period is the same as the Earth's rotation, resulting in a satellite that appears stationary with respect to a fixed location on the Earth's surface. These satellites have an altitude of 35 786 km.

The type of orbit that is most often used for Earth observations, and is most important for this study, is the polar orbit, which will be discussed in the next section.

1.5.1 Polar satellites

Satellites with a polar orbit usually have a north-south orientation, passing roughly over the Earth's poles during each period. Polar orbits are a type of low Earth orbit, as they have an altitude of less than 1000 km. They have an orbital period of about 100 minutes (depending on the altitude) and thus travel around the Earth more than 10 times a day, which is ideal for scanning the Earth, making measurements and observations throughout the day. [ESA, 2020]

A special type of polar orbit is the Sun-synchronous orbit (SSO). In this orbit, the satellite is positioned such that it is synchronised to always have the same position relative to the Sun. As a result, the satellite observes a location on the Earth's surface at the same local solar time each day, which is advantageous for observing processes at each location over time at the same local time.

Usually, satellites in a SSO are synchronised in such a way that they constantly observe the morning/evening. In this case, the satellite will never have the Sun at an angle that the Earth shadows them, which could result in power or imaging problems.

1.5.2 Scatterometers

Satellite observations of near-surface ocean winds are done by scatterometers. A scatterometer is a type of active measurement instrument, mounted on a satellite, which sends radar waves (microwaves) to the Earth's surface and measures the backscatter reflected on the ocean surface.

The mechanism of scatterometers (see Fig. 10) is based on the relation between the sea surface roughness and the intensity of backscatter. Near-surface winds generate small capillary

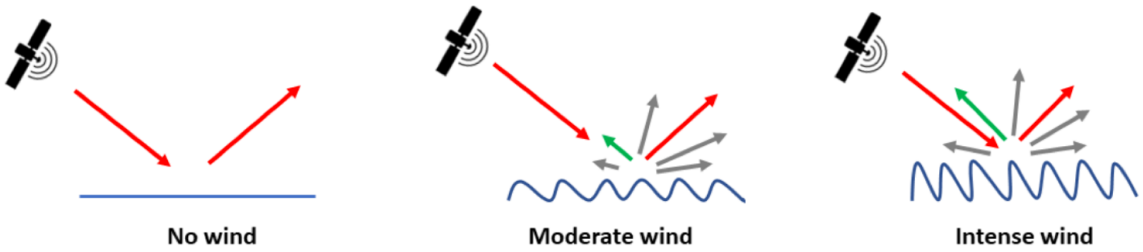

Figure 10: Schematic illustration of the mechanism behind a satellite scatterometer for different wind intensities. [Miguel Fernández, 2023]

waves on the ocean surface, because of the shear between the two fluids. Stronger near-surface winds generate more and stronger capillary waves, increasing the roughness of the sea surface and intensifying the backscatter of the microwaves sent by scatterometers.

The physical variable measured is the normalised radar cross-section of the ocean surface, σ_0, which depends on the surface wind speed and direction. Other factors influence σ_0 too, such as the radar frequency and polarisation, incidence and azimuth angle, as well as the reflectivity of the surface or the presence of land or sea ice.

As said before, σ_0 is the normalised radar cross-section, defined as the backscattered power divided by the emitted power flux of the instrument.

$$\sigma_o = \frac{(4\pi)^3 R^4 P_R}{\lambda^2 F P_T}. \tag{5}$$

Here, P_T is the microwave pulse power, P_R the backscattered power received by the scatterometer, λ the wavelength of the emitted radar waves, F the footprint area covered by the satellite and R the distance between the satellite and the target. [EUMeTrain] [Stoffelen, 1998]

The processing of σ_0 to obtain the near-surface wind field is done by using the empirical Geophysical Model Function (GMF), which yields the stress-equivalent wind field ($\boldsymbol{u_{10,s}}$) at 10 m height. The GMF requires σ_0, the incidence angle θ, the relative azimuth angle ϕ, the wavelength and the polarisation of the beam as input, before it yields the stress-equivalent wind speed and direction.

1.5.3 Relevant satellites

This research focuses on the year 2022 and uses two types of satellites, consisting of in total five satellites. The reason for choosing 2022 is that this is the first full year that five advanced scatterometer satellites observe the Earth.

The first type of satellite is the Meteorological operational Satellite (MetOp for short) and currently consists of two satellites (MetOp-B and -C). They are commissioned by the European Organisation for the Exploitation of Meteorological Satellites (EUMETSAT) and built by the European Space Agency (ESA). Both satellites have sun-synchronous orbits, with

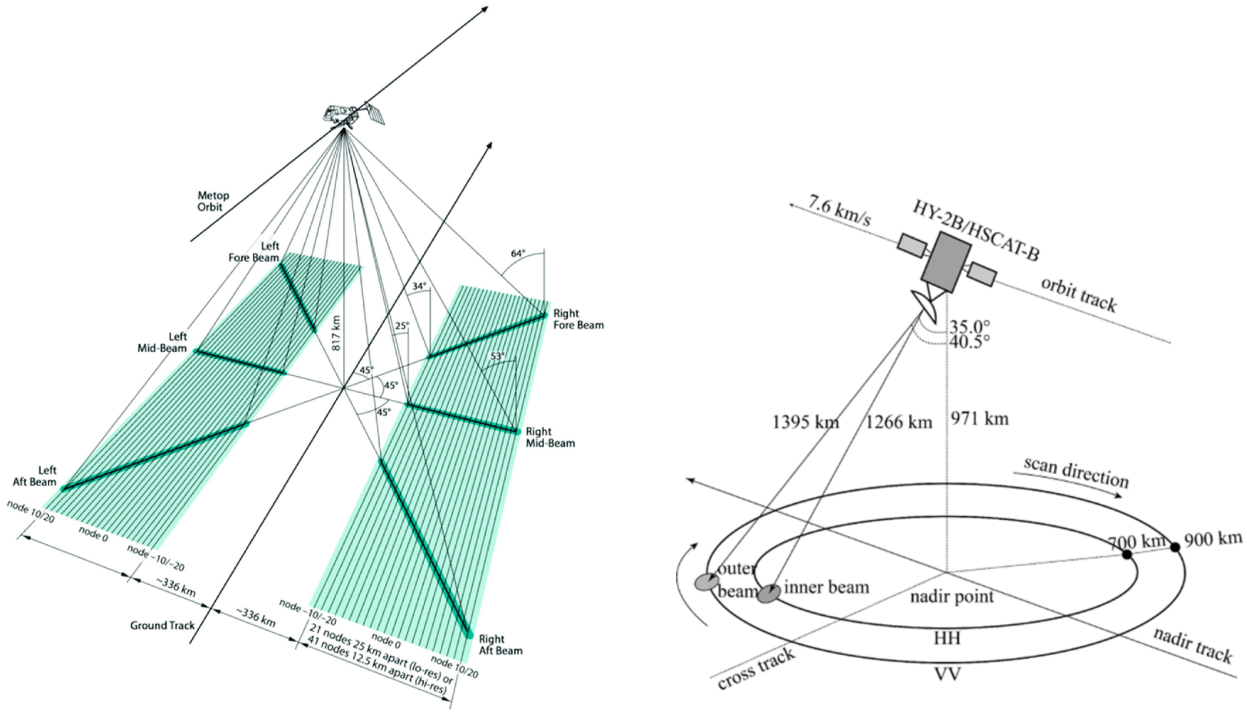

(a) Fixed fan-beam (b) Rotating pencil-beam

Figure 11: Schematics of (a) the ASCAT-instrument (MetOp), with a fixed fan-beam antenna [Nekrasov et al., 2019] and (b) the HSCAT-instrument (HY), with a rotating pencil-beam antenna. [Zhang et al., 2021]

MetOp-C trailing closely behind MetOp-B.

The scatterometer instrument the MetOp satellites use is the ASCAT-instrument (Fig. 11a), which emits radar waves in the C-band frequency (5.255 GHz). The ASCAT-instrument uses a set of six fixed fan-beam antennas, which are oriented in each direction, except the direction of motion, with a 45° angle between each antenna. It scans the sea surface in two swaths of 550 km wide which are 672 km apart. Each point in the swath is scanned by three antennas in a short period of time. [Nekrasov et al., 2019]

The second set of satellites are the Haiyang satellites (HY for short), of which there currently are three: HY-2B, -2C and -2D, the last of which was launched in 2021. They are commissioned and operated by the Chinese National Satellite Ocean Application Service (NSOAS) and built by the China Academy of Space Technology (CAST). Of the three satellites, HY-2B is the only one with a sun-synchronous orbit. The other two have a polar inclined orbit covering 74° N to 74° S.

The instrument HY uses is called HSCAT (Fig. 11b), which utilizes a rotating pencil-beam antenna at a K_u-band frequency (13.4 GHz). This 1 m long parabolic antenna has two offset feeds creating an inner and outer beam, rotating in the plane parallel to the surface. The swath is 1800 km wide and each point is scanned up to four times, twice by the inner beam and twice by the outer. In contrast to the ASCAT-instrument, the HSCAT-instrument uses a fixed horizontal polarisation for the inner beam and vertical polarisation for the outer

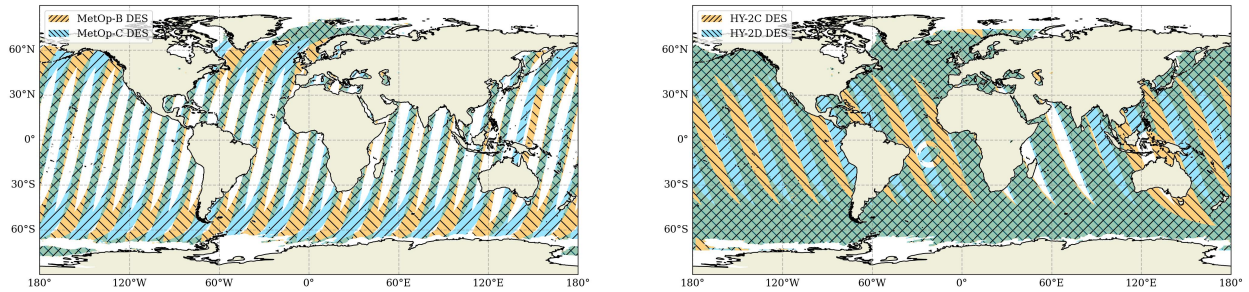

(a) MetOp-B and MetOp-C, descending orbits

(b) HY-2C and HY-2D, descending orbits

Figure 12: Sample of the daily surface coverage of the scatterometer instruments of the MetOp satellites (a) and HY-2C and -2D (b) for their descending orbits.

beam, resulting in four independent measurements of the swath area. The higher frequency of HSCAT is a result of the length of the antenna being a limiting factor. This has as a result that HSCAT is sensitive to rain and higher wind speeds. [Zhang et al., 2021]

As mentioned before, both MetOp satellites have a Sun-synchronous orbit, passing the equator at 9:30 (AM and PM) local time each day. They also follow the same orbit, with MetOp-C trailing approximately 50 minutes behind MetOp-B, resulting in a lot of overlap between their swaths (Fig. 12a).

HY-2B is also Sun-synchronous, but passes each point at 6:00 AM/PM local solar time instead. HY-2C and -2D are just in a polar orbit, meaning that they pass a certain location a little earlier each day and do not cover the whole Earth daily, which makes them more suitable for studying diurnal and daily cycles than satellites in SSO. They also complement each other, with a time difference between HY-2C and -2D of exactly 6 hours (Fig. 12a).

1.5.4 Recent scatterometer research

Since their inception, scatterometers have been extensively used to study the near-surface ocean winds. Due to their near global coverage, clever positioning of satellites and high resolution, a lot of data has been collected that is simply not possible with in situ measurements. This data has been used to study wind phenomena like the Tehuano Wind [Smith, 2015], wind wakes near Hawaii [Yang et al., 2008] or tracing tropical cyclones [Soisuvarn and Oudomying, 2018].

Additionally, scatterometer data is also used to initiate runs of numerical weather forecast models. Comparisons between scatterometer and model fields also reveal where the numerical models are sub-optimal [Belmonte Rivas and Stoffelen, 2019] and use this data to further improve these models.

1.6 Numerical weather prediction models

Ever since the 1920's, scientists have tried to numerically predict the weather based on current weather conditions, a very important factor for aviation and sea traffic. This, however, was unsuccessful until the arrival of the computer.

Numerical weather prediction (NWP) models are forecast models that simulate all the physical processes that occur in the atmosphere, and its interactions with land and oceans, and thus make a prediction of the weather for the coming (5 to 10) days. They are initiated using synoptic data from satellites and in-situ observations.

NWP models usually consist of a set of interdependent models that simulate the atmosphere, the ocean, waves and surface/soil processes. These models are all governed by a set of physical laws, like momentum, mass and energy conservation, the Navier-Stokes equations and a whole range of fluxes (heat, radiation, moisture). All these physical laws result in a set of interdependent non-linear differential equations, which produce variables as temperature, wind speed and direction, moisture content, cloud cover, and so on. These equations are exceedingly complicated and cannot be solved analytically. Even to solve these equations numerically, the model needs to be discretized, spatially into grid cells and temporally into finite time steps, since even the most advanced super computers do not have infinite computational power.

Many physical processes, like the formation of clouds, take place on spatial scales much smaller than the size of a grid cell, and thus cannot be solved explicitly in the discretized NWP models. To still include these processes as best as possible, they are approximated using parameterizations. [DWD]

Since the atmosphere is a chaotic system, and the discretized NWP models will inevitably result in small inaccuracies/errors, the forecast will eventually become very inaccurate. Most current forecast models can reliably predict the weather for the coming three days, before rapidly becoming inaccurate. To mitigate this, one can perform an ensemble forecast, where multiple runs with slightly different initial conditions are executed. When the individual runs are very similar, the forecast can be perceived as accurate. [Dunlop, 2017]

2 Project objectives

This study focuses on the rotation and divergence of the near-surface ocean wind field, measured by scatterometers. Analyses will be performed on both global and regional scales and for several different time scales. The observational data will be compared with collocated model data from the ECMWF Operational model to calculate the bias. The aim of this study is twofold: first to identify strong persistent regional biases in the rotation and divergence of the near-surface wind field, and secondly to further understand why these biases occur and find the limitations of the model.

2.1 Biases in the curl and divergence

A large part of this study consists of analysing the biases in the divergence and rotation of the near-surface ocean wind field. This is done by first looking at the most global scales and subsequently focusing on more specific regions and smaller timescales. The regions selected all have interesting flow patterns, caused by either topography or meteorology (or a combination thereof) and can be found below.

- **Northern Madagascar**: site of a strong turbulent island wake due to strong trade winds;
- **The south of Mexico**: location of a very strong mountain-gap wind (the Tehuano Wind);
- **Hawaii**: island chain in the Pacific ocean, causing disturbances in the wind field. Mainly gap winds and turbulent island wakes (often in the form of the von Kármán vortex street);
- **The Western North Atlantic**: Location of the Gulf Stream. Many fronts and depressions as well as strong air-sea interactions are present in this area.

The first objective of this study is to answer the question: *What are the patterns and biases for the mean and eddy flow?*

This will be done for a global scale and for four different regions and for three different timescales:

- yearly (general patterns);
- monthly (main focus on January, April, July and October, representing all seasons);
- daily timescale.

2.2 Causes of these biases

The second objective of this research is to determine why the biases found occur. This will be done by analysing the most relevant parameters and influences for each region. The following topics will be discussed:

- the interpolation scheme of model data to the scatterometer grid. Comparison of collocated model winds with hourly ECMWF-Ops data, which is also an indication of scatterometer sampling effects;
- physical modelling limitations (mainly coupling with SST and topography);
- how well does the model handle synoptic events?

2.3 Summary

To summarize, the main goal for this study is to answer the following research questions:

- What are the main biases in the wind rotation and divergence for each region and timescale?
  - Where/when are the biases strongest/weakest?
  - What dominates, biases in the mean or eddy flow?
- What are the main causes of the model biases for each region and timescale?

3 Data and methods

This chapter introduces the datasets and products used for this study, and discusses the methods used for further data processing and choices made along the way.

3.1 Data

3.1.1 Scatterometer data products

The most important datasets for this research are the Level 3 scatterometer wind products processed and provided by the Royal Netherlands Meteorological Institute (KNMI). The processing level, ranging from 0 to 4, determines to what extent the data have been processed. A short description of each processing level can be found in Table 1.

Table 1: Brief description of the processing levels for satellite data acquisition. [NASA, 2021]

Level	**Description**
0	Raw data, unprocessed, reconstructed and at full instrument resolution.
1A	L0 data that are time-referenced and annotated with additional information, including radiometric and geometric calibration coefficients and georeferencing parameters.
1B	L1A data, processed to sensor units (not all instruments have L1B source data).
1C	L1B data, including new variables to describe the spectra.
2	Derived geophysical variables with the same resolution and location as the L1 data.
3	Geophysical variables mapped on uniform space-time grid scales, usually with some completeness and consistency.
4	Model output or results from lower-level data analysis (variables derived from multiple measurements), variables mapped on non-uniform grids or higher-level data products (maps and animations).

The focus of this project is on the year 2022. The data from MetOp satellites is available in 1/4° (25 km) and 1/8° (12.5 km) resolution, while the HY-satellites provide a 1/4° (25 km) and 1/2° (50 km) resolution. Because of the higher resolution and lower sensitivity to rain, the main analysis will be done using data from the MetOp satellites, with the HY-satellites providing support for the smaller time scales.

For the global scale, the 0.25° resolution data is used due to large dataset sizes. For regional scales, the highest resolution available per satellite is used. On regional scales, the data are analysed for specific months with features of interest (Section 3.2.1). Table 2 shows an overview of the selected resolutions and time ranges per satellite.

The main variables provided by the Level 3 product are the stress-equivalent eastward and northward wind (u and v, respectively), the curl and divergence of the wind field, as well as the observational measurement time for each data point, given in UTC.

Table 2: Overview of Level 3 data used per satellite, including the resolution and time range. All data is from the year 2022 and also contains hourly collocated ECMWF-Ops data.

Satellite	Resolution	Time range
MetOp-B	Global: 0.25° Regional: 0.125°	Global: year Regional: Jan, Apr, Jul, Oct
MetOp-C	Global: 0.25° Regional: 0.125°	Global: year Regional: Jan, Apr, Jul, Oct
HY-2B	0.25°	Jan, Apr, Jul, Oct
HY-2C	0.25°	Jan, Apr, Jul, Oct
HY-2D	0.25°	Jan, Apr, Jul, Oct

3.1.2 Data processing and model collocation

The cornerstone of this research is the comparison between scatterometer observations and model data fields. It is therefore required to collocate the model fields to the observations in space and time. The model used for the comparison is the Operational Model of the Integrated Forecasting System (IFS), specifically the HRES forecasts, developed by the European Center for Medium-Range Weather Forecasts (ECMWF), further indicated as ECMWF-Ops. Given that the observations are from the year 2022, cycle 47r3 of the operational model is used for collocation. [ECMWF, 2023]

The collocation of the model fields consists of both spatial and temporal averaging, such that the output matches the spatial and temporal grid of the observations. The spacial resolution of the ECMWF-Ops is 9 km and the collocation is done by KNMI when the product is still in its Level 2 phase. The spacial collocation is done by selecting the four nearest neighbours of the grid point of collocation, then averaging their values, using weighted averaging as $1/r^2$. This already results in some smoothing of the values. Given that the spatial resolutions of the satellites in their Level 2 phase is 25 km (both HY and MetOp) or 12 km (MetOp), the reduction of the model resolution will not have a significant impact. Furthermore, the actual resolution of ECMWF-Ops over the ocean is of the order around 100-150 km, since most of the processes are on larger scales.

The operational model is run once every 12 hours and yields its output on an hourly temporal scale (3-hourly for 25 km MetOp), while observations are measured in real time. So, for the temporal collocation, a linear interpolation is performed between the two closest forecasts of the selected data point, making sure that the two forecasts are from the same model run.

After the collocation process, the product is further processed to Level 3. The processing from Level 1 to 3 of the scatterometer wind products has been done by KNMI, which includes some data validation and masking of unreliable data. Further information of the processing can be found in the product user manual (OSI SAF, 2022). Note that the datasets used in this study vary slightly compared to the documentation. The HY data is processed with a newer processor and both HY and MetOp observations are collocated with hourly ECMWF-Ops data, instead of 3-hourly data.

The data is provided in NetCDF format. The dataset is divided per day and direction of the orbit (ascending and descending). This subdivision per orbit is done to avoid overlapping data for some areas and is especially important for the satellites in SSO, given that the direction of the orbit is linked with the local measurement time.

3.1.3 SST datasets

MetOp-B also contains a sensor, the Advanced Very High Resolution Radiometer (AVHRR), that can measure the sea surface temperature (SST) at a resolution of 1/20°. For the analysis of the SST-surface wind coupling, the data from this sensor is also used. (Level 3 Sea Surface Temperature product processed by CMEMS, for January and April 2022) [C3S, 2024]

3.1.4 ETOPO

Since some of the wind phenomena studied in this research are related to the topography, a high resolution orography is also needed. The ETOPO Global Relief Mode (version 2022) is a high resolution rendering of the geophysical characteristics of the Earth's surface, including the orography and bathymetry. It has a resolution of 1/60° and is developed by the National Oceanic and Atmospheric Administration (NOAA). [NOAA-NCEI, 2022]

3.1.5 Additional ECMWF-Ops data

Additional datasets from the ECMWF-Ops are also used in this study. These datasets contain hourly model fields on a reduced Gaussian grid and are interpolated to a regular 0.125° grid (Table 3). The dataset containing the wind field variables is used to analyse the interpolation scheme. The sea-surface temperature (SST) is used for model collocation with the SST-observations from MetOp-B, and the analysis of the SST-surface wind coupling. Finally, the geopotential is used to determine the topography used by the operational model.

The geopotential is the (potential) energy needed to lift an object of 1 kg to a certain height with respect to the Earth's mean sea level (where the geopotential is zero). Taking the surface value of the geopotential and dividing it with the gravitational acceleration constant ($g = 9.80665$ m/s^2) yields the ECMWF-Ops orography, which is then compared with the high resolution ETOPO orography.

Table 3: Overview of the ECMWF-Ops datasets used. All datasets cover 2022 and are interpolated to a 0.125° regular lat-lon grid.

variable	**Time range**
wind field (u, v, curl and divergence)	Jan, Apr, Jul, Oct
SST	Jan, Apr, Jul, Oct
Geopotential	Jan 1st

3.2 Methods

In this section, the reasons for selecting specific regions and time ranges are covered. Furthermore, the definitions of the relevant statistical parameters are discussed as well as the method of bias calculation. Finally, whenever required, the further processing of the data is discussed.

3.2.1 Region and time range selection

For the analysis of global patterns in the scatterometer fields, the yearly average is used. The global analyses are used to identify interesting phenomena that occur on regional and smaller time scales. For each focus region, a specific month is chosen for further analysis, based on the characteristics of the phenomena to be investigated.

Table 4: Coordinates of the boundaries for each region.

Number	Region	Domain [West, East, South, North]	Focus month
1.	North Madagascar	[38° E, 58° E, 18.5° S, 3° S]	October
2.	South Mexico	[-165° E, -153° E, 16° N, 24° N]	January
3.	Hawaii	[-165° E, -153° E, 16° N, 24° N]	July
4.	Gulf Stream	[-82.5° E, -50° E, 22.5° N, 50° N]	April

As specified in Section 2.1 The focus regions are defined near Hawaii, the south of Mexico, the Gulf Stream area (Western North Atlantic) and North Madagascar (Fig. 13). Table 4 lists the coordinates of the boundaries of each domain, as well as the month of focus for each region.

1. **The north of Madagascar**: Strong trade winds from the southeast are deflected by the mountains of Northern Madagascar, resulting in a turbulent island wake. The trades are most dominant in this region in October.

2. **The south of Mexico**: Just south of Mexico one of the strongest mountain-gap winds is located: the Tehuano Wind (Section 1.4.1). These gap winds are semi-regular events that occur most often during the winter months. Hence, the focus month for this region is January.

3. **Hawaii**: The mountainous island chain of Hawaii lies in the middle of the Pacific Ocean, in the path of the strong trade winds coming from the northeast. The interaction between the trade winds and the islands results in a combination of turbulent island wakes and gap winds on the lee-side of the Hawaiian Archipelago. Occasionally, the island wakes behind the islands develop into a Von Kármán vortex street. The focus for this region will be on July, since the trade winds are strongest during the summer months, causing the strongest bouts of turbulence.

4. **The Gulf Stream area**: Initial analysis of the scatterometer data shows that some of the largest biases in the curl of the surface wind field occur near the Gulf Stream.

The strong air-sea interactions and the relatively weak Ferrel Cell result in some very interesting weather phenomena in this region. During spring, temperature differences between land and sea as well as the SST gradient itself are relatively strong, resulting in a strong rotation bias in these months. Hence the focus month for this region is April.

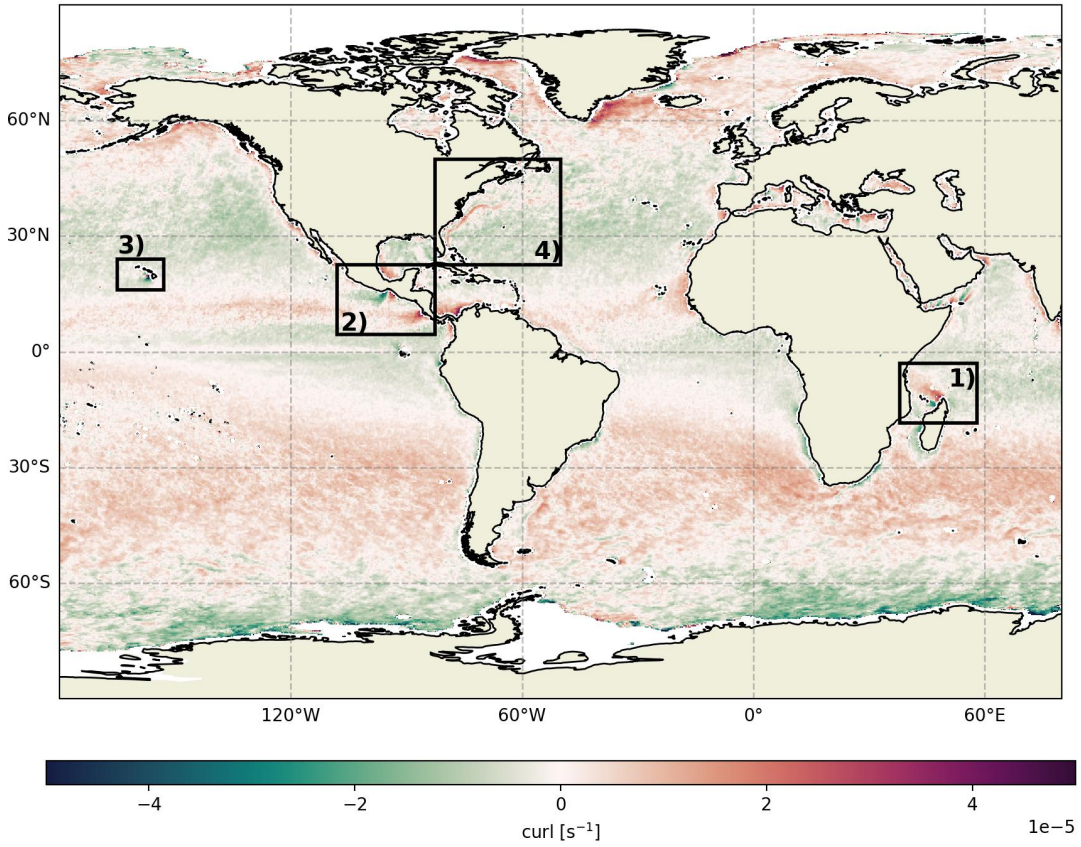

Figure 13: The four different domains chosen for this study: 1) the north of Madagascar, 2) South Mexico, 3) Hawaii and 4) the Gulf Stream region. The background shows the yearly mean curl for the descending orbit of MetOp-B for 2022.

3.2.2 Statistics and bias calculation

For the accurate quantitative analysis of the differences between satellite observations and model fields, or between different datasets, the use of some statistics is required. This section introduces the calculation of the mean and eddy flows (standard deviation for curl and divergence), as well as the definition of the bias. Note that the definitions of the mean, eddy flow and bias are the same as in Belmonte Rivas and Stoffelen [2019].

- **Mean**
  Generally, when the word 'mean' is used in this research, the temporal average of a value each grid point is intended. The temporal mean of a variable q with coordinates (x, y) over a period (T) is defined as

$$\bar{q}(x, y, T) = \frac{1}{T} \sum_{t=1}^{T} q(x, y, t). \tag{6}$$

  Additionally, the zonal mean is briefly discussed. For the zonal mean, the averaging is not only done over time, but also over all longitudes (x)

$$\bar{q}(y, T) = \frac{1}{T} \frac{1}{X} \sum_{t=1}^{T} \sum_{x=1}^{X} q(x, y, t). \tag{7}$$

- **Standard deviation**
  The standard deviation indicates the variability of a certain dataset around the mean. With respect to fluid flows, the standard deviation is usually signified as the eddy or transient flow. The standard deviation is defined as

$$\sigma(x, y) = \sqrt{\frac{1}{T} \sum_{t=1}^{T} \left(q(x, y, t) - \bar{q}(x, y, T)\right)^2}. \tag{8}$$

  In case the eddy flow is calculated for the yearly scale, a running mean is used for each month of the year. This means that for example, for the month January, the mean value of that month is used in the calculation of the eddy flow, changing into the mean of February as the data progresses to February. This is done to filter out any seasonal effects on the eddy flow, showing the true variability of the flow compared to its mean value.

- **Bias**
  The bias (δq) of a variable is defined as the difference between a (satellite) observation and the corresponding value of the NWP model fields according to

$$\delta q(x, y, t) = q_{scat}(x, y, t) - q_{NWP}(x, y, t), \tag{9}$$

  where q_{scat} is the observation and q_{NWP} the model value. Calculation of a bias is an efficient way to analyse whether a model under- or over-performs compared to observations. Note that a positive (negative) bias indicates that the model values are too low (high) compared to the observations.

- **Correlation coefficient**
  The (Pearson) correlation coefficient (r) is a measure to determine the linear relation between two different datasets of the same length. It is defined as the ratio between

the covariance of the two datasets (p and q) and the products of the two standard deviations:

$$r(x,y) = \frac{\frac{1}{T}\sum_{t=1}^{T}(p(x,y,t) - \bar{p}(x,y))(q(x,y,t) - \bar{q}(x,y))}{\sigma_p(x,y)\sigma_q(x,y)}. \tag{10}$$

The values of the correlation coefficient range between -1 and 1, with 1 meaning that the two datasets perfectly correlate, 0 meaning there is no correlation, and -1 meaning that the two datasets perfectly anticorrelate.

Along with the correlation coefficient, there are two more parameters that determine the relation between datasets in a linear regression fit: the slope parameter (α), indicating how much variable p increases as q increases, and an independent constant (β), which is the independent bias of p with respect to q.

$$X_p = \alpha X_q + \beta. \tag{11}$$

In case a linear fit is used to evaluate observations with model values, the ideal result would be a high correlation coefficient, a slope parameter around 1 and an independent constant around 0.

3.2.3 Data processing

Most of the data processing is relatively straightforward. The scatterometer datasets are recombined into larger NetCDF files, still subdivided in orbital direction, but now containing all data for a specific time range and region. Doing so makes it easier to calculate the various statistics necessary for the data analysis.

The observational SST-data from MetOp-B and the ETOPO orography data from NOAA, however, have both a resolution that is too high for good comparison with the observations and model data at a 0.125° grid. Thus, these datasets are reshaped to a regular 0.125° grid using a simple spatial averaging scheme: taking the spatial mean of all the data points that are closest to a selected grid point on the 0.125° grid. These datasets are then saved into new NetCDF files and used in further processing.

For the analysis of the SST and the interpolation scheme for the scatterometer wind fields, ECMWF model data that is already processed to a regular 0.125° grid is collocated to the observations using the same method as is used in the Level 3 wind products: linear interpolation.

4 Results

This chapter presents the main results of this study. First, the global distribution of the wind field rotation and divergence, and their biases, are discussed. Then, the focus will be directed at the specific regions which have been selected on the basis of the global maps. After discussing the general and more specific patterns of the wind divergence and/or rotation, possible causes for the rotation and/or divergence biases found will be considered. The final part of this chapter focuses on the effects of collocation and multiple interpolation steps on the model datasets.

4.1 Global bias

Before the focus shifts to regional biases, it is important to understand the global patterns, both in the observations and biases. So in this section, the global patterns will be introduced, first generally by discussing the zonal means, then more closely by looking at their spatial patterns. From these results, four different cases are selected which show interesting patterns and biases. These regions will be discussed in the rest of this chapter.

4.1.1 Zonal means

To quickly get an overview of the global distribution of the surface wind rotation and divergence, it is useful to make a zonal average, since climate zones mainly vary with latitude. Figure 14 shows the zonal averages of the yearly, January-March and July-September mean observed surface wind rotation and divergence for 2022, as well as their computed biases with respect to the ECMWF operational model. The observations originate from MetOp-C and are comprised of both the ascending and descending orbit.

To start with the rotation, Figure 14a shows that for the mid-latitudes (30°-60°) the dominant rotation is negative (clockwise) for the Northern Hemisphere (NH) and positive (anticlockwise) for the Southern Hemisphere. This is corroborated by the deflection of the Coriolis force, which is to the right (left) on the NH (SH). During the summer and winter months, the trade winds pass the equator in their approach to the ITCZ and the Coriolis deflection changes sign, resulting in a net negative curl when the ITCZ is positioned on the NH (Jul-Sept) and a net positive curl when the ITCZ is located south of the equator (Jan-Mar).

The bias of the zonal mean wind curl (Fig. 14b) averages around zero and shows little seasonal variability. It does show a lot of local variability, however, which is largest for the NH summer months north of 30° N, probably due to less ocean coverage on the NH. Furthermore, towards the poles, the bias becomes slightly positive (SH) or slightly negative (NH). This means that the model slightly underrepresents the surface wind rotation at mid-latitudes, yet slightly overrepresents the rotation at higher latitudes.

For the surface wind divergence (Fig. 14c), it can be seen that the strongest net convergence (negative divergence) takes place just north of the equator throughout the year and at higher latitudes (polewards of 60°). Convergence is generally stronger than net divergence, which is spread out over a larger area around the mid-latitudes. The exception is at the equator itself,

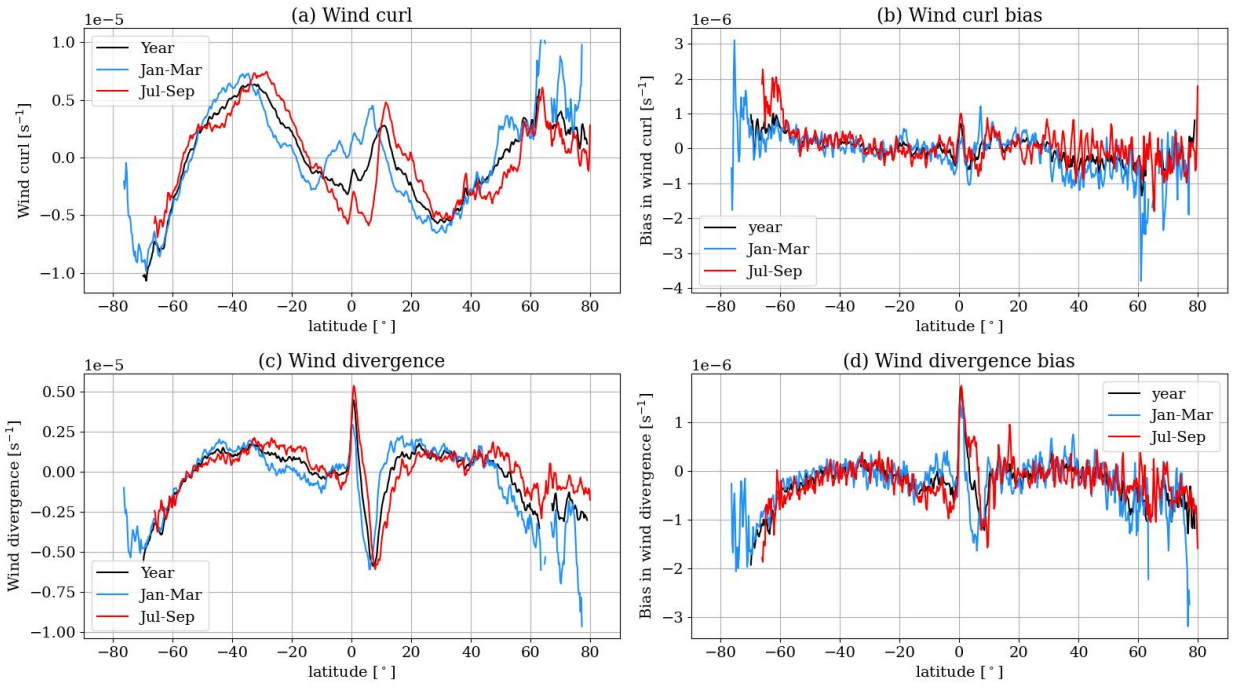

Figure 14: The zonally averaged observed wind curl (a) and divergence (c), and their biases (b) and (d) respectively. The black lines show the result for yearly averages, the blue lines for the months January to March and the red lines the months July to September. The observations originate from MetOp-C, encompassing both orbits. For the yearly plots, a minimum threshold is set on 50 data points, while for the seasonal plots this threshold is set on 10 data points.

where there is a sharp divergence peak. The positioning of the convergence and divergence areas agrees with the general circulation: net convergence just north of the equator (yearly mean position of the ITCZ) and at 60° N/S due to the atmospheric lows and divergence in between. The sharp divergence peak directly over the equator is caused by the fact that there is no Coriolis acceleration at 0° and the wind blows from east to west. Hence, a small perturbation north (south) of the equator causes a parcel of wind to deflect northward (southward) due to the shifting signs of the Coriolis force.

The bias of the zonal mean wind divergence is mainly negative (Fig. 14d). It is small around the divergence areas at the mid-latitudes and becomes more negative towards the poles and equator. There is only one narrow positive peak of the bias, directly over the equator. Again, the signal shows notable variability, mainly at the NH. A negative bias around the convergence areas indicates that the operational model underestimates the convergence compared to observations. A similar conclusion can be drawn for the sharp positive bias peak around the equator, where the divergence is underestimated.

4.1.2 Temporal mean and eddy flow

Figure 15 displays the spatial distribution of the mean and transient surface wind rotation for 2022. The observations (a) and (b) are again from MetOp-C for both orbit directions.

The model fields are shown in (c) and (d) while the biases can be found in (e) and (f).

The wind curl (Fig. 15e) overall displays a fairly low bias in the global spatial distribution. There is quite a bit of local variability again, particularly at higher latitudes, but this can be explained by the fact that the model rotation field is smoother than the observations (compare Fig. 15a with 15c). There are a few regions, however, where the bias is still strong. (For a larger plot of the global mean rotation bias see Appendix A) This is mainly the case for the Western North Atlantic, close to the US East Coast, just north of Madagascar and just southwest of Hawaii. There is also a stronger mean bias directly over the equator in the eastern part of the Pacific Ocean.

The spatial distribution of the 2022 eddy flow of the wind curl (Fig. 15b) shows that most of the variability can be found at the mid- and higher latitudes, with lower values in the subtropical Pacific and Atlantic Oceans. This is to be expected, since fronts and depressions are most common at higher latitudes. Fig. 15f shows that the flow variability is underestimated by the model globally, but mainly in the tropics around the ITCZ, where observations show moderate variability and the model low variability.

These results are in line with the previous work of Belmonte Rivas and Stoffelen [2019], who studied the bias of the ASCAT-A surface wind (from the now retired MetOp-A satellite, 25 km resolution) with the ERA-Interim (resolution 79 km, 3-hourly) and ERA5 (resolution 31 km, 1-hourly) models for the annual mean and eddy flows of 2016. Comparing their results for the 2016 wind stress curl, it can be seen that, even though the general patterns are very similar, both the ASCAT data-resolution and the model have improved. Especially at higher latitudes, the biases of ECMWF-Ops are smaller than those of ERA-Interim and ERA5.

Regarding the spatial distribution of the 2022 mean and transient wind divergence (Fig. 16), it can be seen that overall, the spatial distributions of the observations and model match relatively well. The data also matches the results from the zonal means (Fig. 14c), with a strong convergence zone just north of the equator, and an area of strong divergence directly over the equator, which are most dominant in the Pacific, yet are also present in the Atlantic. The mean bias is, as expected, strong over the ITCZ and over the equator, again mainly in the Pacific. There is also a considerable mean bias present southwest of Hawaii.

The transient wind divergence is significantly larger in observations (Fig. 16b) than in the model fields (Fig. 16d). The distribution is similar, yet the model shows less variability in the divergence. The divergence is most variable around the ITCZ and near the WBC's. It is moderate at mid- and higher latitudes and is weakest in the subtropics.

The results for the divergence are again in line with Belmonte Rivas and Stoffelen [2019]. The mean patterns are very similar yet the observational data resolution has again increased and the biases of ASCAT observations with ECMWF-Ops are smaller than the biases of ASCAT-A with ERA-Interim and ERA5. The eddy wind divergence for 2016 is very similar to the results of 2022, and the ASCAT-A bias with ERA5 is very similar to the eddy bias seen in the 2022 results (Fig. 16f).

From the global mean wind rotation fields, three regions with large global mean biases were selected: North Madagascar, Hawaii and the Gulf Stream area in the Western North Atlantic. The region south of Mexico was also added since it is one of the few places where a rotational dipole (strong negative and positive rotation close together) is visible on a global scale. These

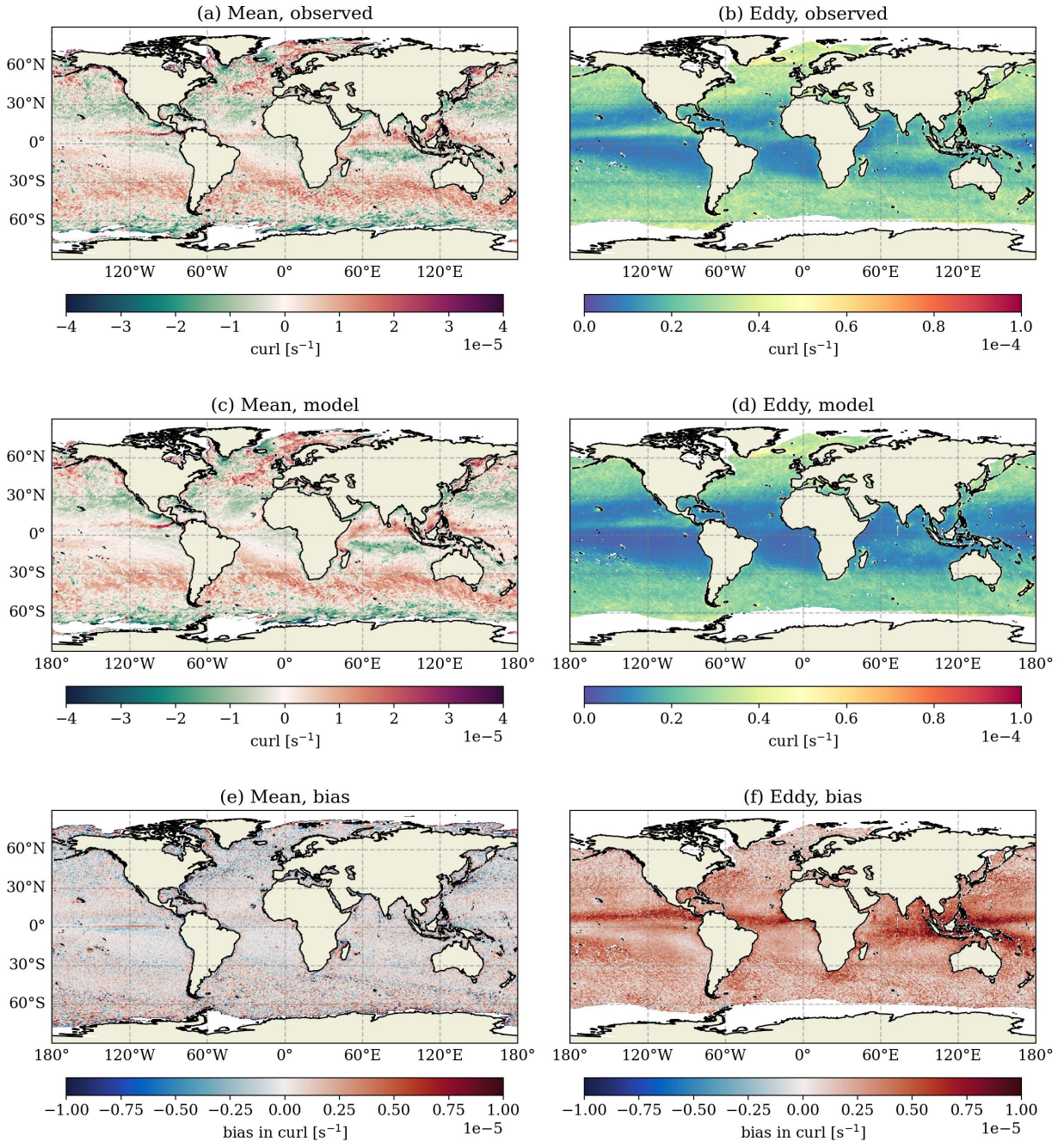

Figure 15: 2022 yearly mean and transient values of the wind curl from MetOp-C observations (a and b), collocated data from the ECMWF operational model (c and d) and their corresponding biases (e and f).

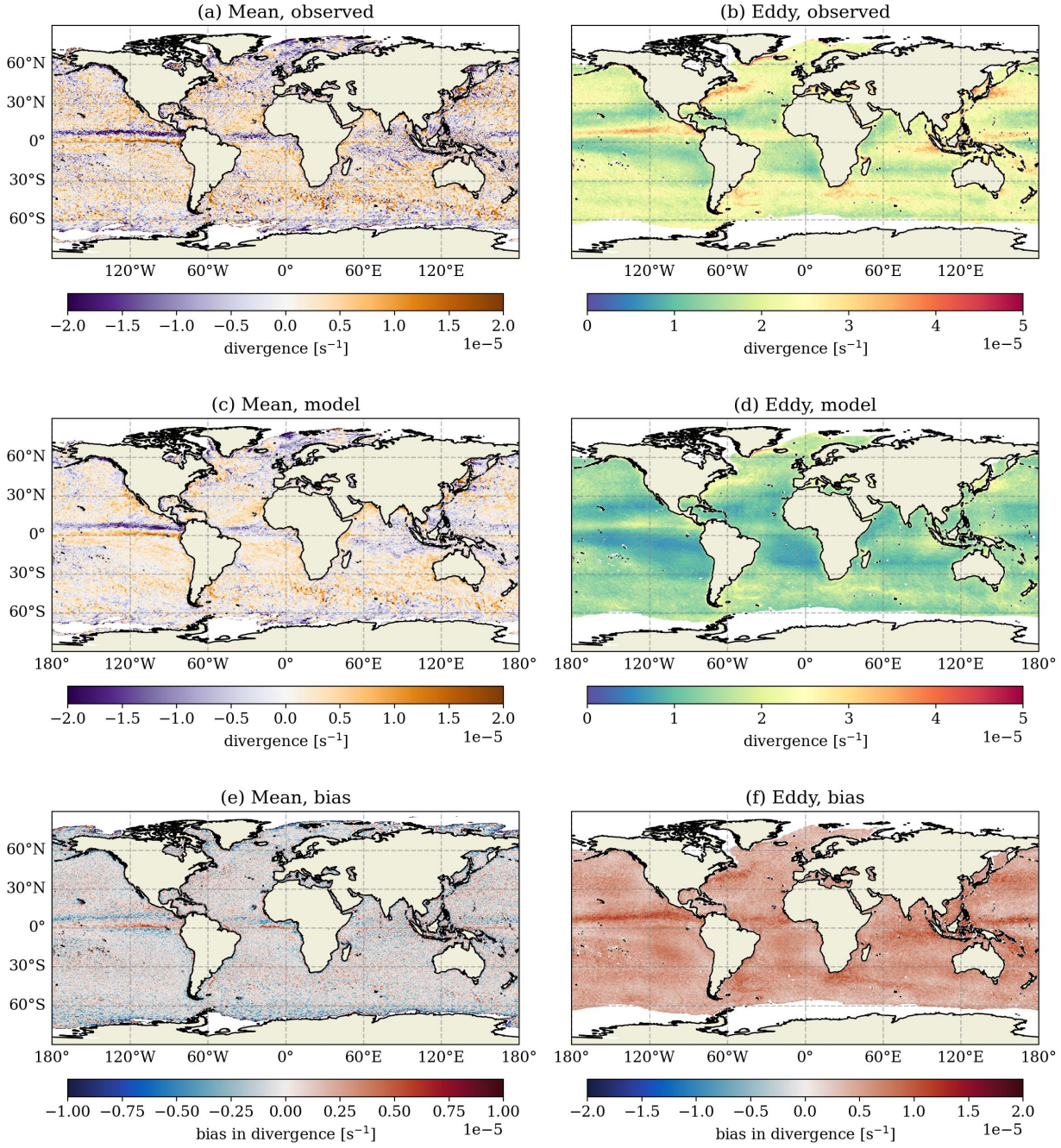

Figure 16: 2022 yearly mean and transient values of the wind divergence from MetOp-C observations (a and b), collocated data from the ECMWF operational model (c and d) and their corresponding biases (e and f).

four cases are further discussed in the following sections.

4.2 Temporal correlations

A quick way to get a grasp of a model's effectiveness to reproduce the observations is to calculate the correlation coefficient. For large climatological datasets, it is most useful to study the spatial distributions of the temporal correlation between observations and the collocated model fields. Please note that a high correlation does not necessarily mean that there is no model bias, since a high correlation only means that the observations and model follow the same patterns, but there can still be a systematic bias present.

This section discusses the correlation of the wind rotation of the four selected regions in their focus month, as an introduction to the model validation, before the focus shifts to each case individually. All observations are done by ASCAT on MetOp-C, distinguishing between the ascending and descending orbits for the calculation of the correlation coefficient.

The first thing of note in the spatial distributions of the correlation coefficient per region (Figs. 17a-17d) is that over large parts, the correlation between observed and modelled rotation is highly variable, varying between correlated ($r > 0$) and anticorrelated ($r < 0$) over small distances seemingly randomly.

There are some areas however, where the correlation is strong locally ($r \approx 1$). For three regions, Madagascar, South Mexico, and Hawaii, the strength of the correlation even varies clearly between the different orbits.

Starting with Madagascar, it can be seen that the correlation is locally strongest during the morning (descending orbit) just west of the northern tip of the island, as well as on most of the northwestern side. Given that the prevailing winds are coming from the southeast in October, this means that the correlation is strongest in the wake of the island.

A similar conclusion can be drawn for Hawaii, where the local correlation is again largest in the wake of the islands (prevailing winds from the northeast in July) for the descending orbit.

In case of the mountain-gap wind of South Mexico, the correlation is locally stronger both north and south of the gap, yet it is strongest for the evening observations (ascending orbit).

Overall, the correlation between ascending and descending orbits for the Western North Atlantic does not vary that much in strength. The correlation is stronger on the northern side of the basin and bands of strong correlation jump out. These probably are the tracks of fronts and depressions, which the model covers reasonably well. Close to the US East Coast, the correlation is predominantly positive as well.

It is as of yet unclear why the three regions that depict topography-induced turbulence show a time dependence in the correlation between observations and collocated model fields, while this dependence cannot be found in the Western North Atlantic region.

Comparing the spatial averages of the correlation coefficients (Table 5), it can be seen that the regional mean r is largest for the Gulf Stream region and lowest for Hawaii and Madagascar. This is in line with Belmonte Rivas and Stoffelen [2019] and Miguel Fernández [2023], who found that the correlation between observations and ERA-products/ECMWF-Ops are lower in the tropics, since the models are biased in the ITCZ. From Miguel Fernández [2023], it

Table 5: Spatially averaged values of the Pearson correlation coefficient (r) per region and satellite orbit for their focus month. All values are for observations made by MetOp-C.

Region	Month	r (descending orbit)	r (ascending orbit)
South Mexico	January	0.221	0.230
Gulf Stream	April	0.366	0.370
Hawaii	July	0.166	0.191
Madagascar	October	0.158	0.173

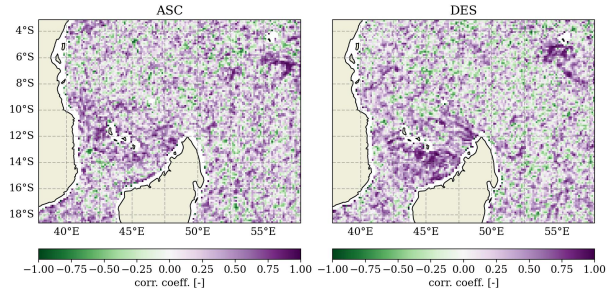

(a) North Madagascar – October

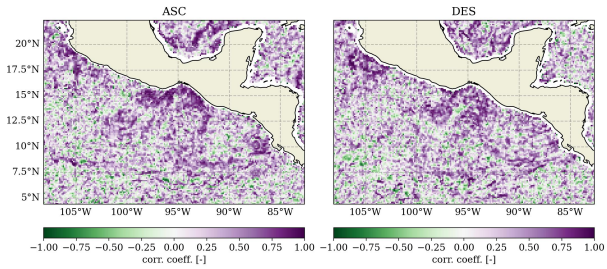

(b) Tehuano Wind – January

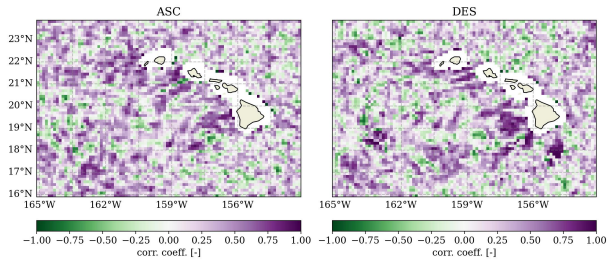

(c) Hawaii – July

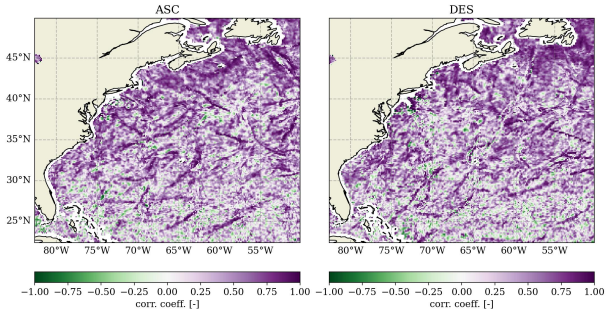

(d) The Western North Atlantic – April

Figure 17: The temporal correlation between MetOp-C vorticity observations and collocated NWP model fields for the focus regions over their selected month in 2022. The plots represent data from the ascending (left) and descending (right) orbit.

should also be noted that the correlation for the HY-satellites is significantly higher, compared to ASCAT measurements from MetOp. This can be allocated to the fact that HY's HSCAT instrument has a coarser resolution. It also yields less extreme measurement values than ASCAT, which are thus more in line with the models (which also do not produce that many extreme values).

4.3 Case: North Madagascar

The first case entails the ocean just north of Madagascar. During the month of October, the strong southeast trade winds prevail over the Indian Ocean near Madagascar. The mountain range close to the east coast of the island deflects the wind northward. Off the northern tip of the island, this deflected flow results in turbulence, which is not that dissimilar to the tip

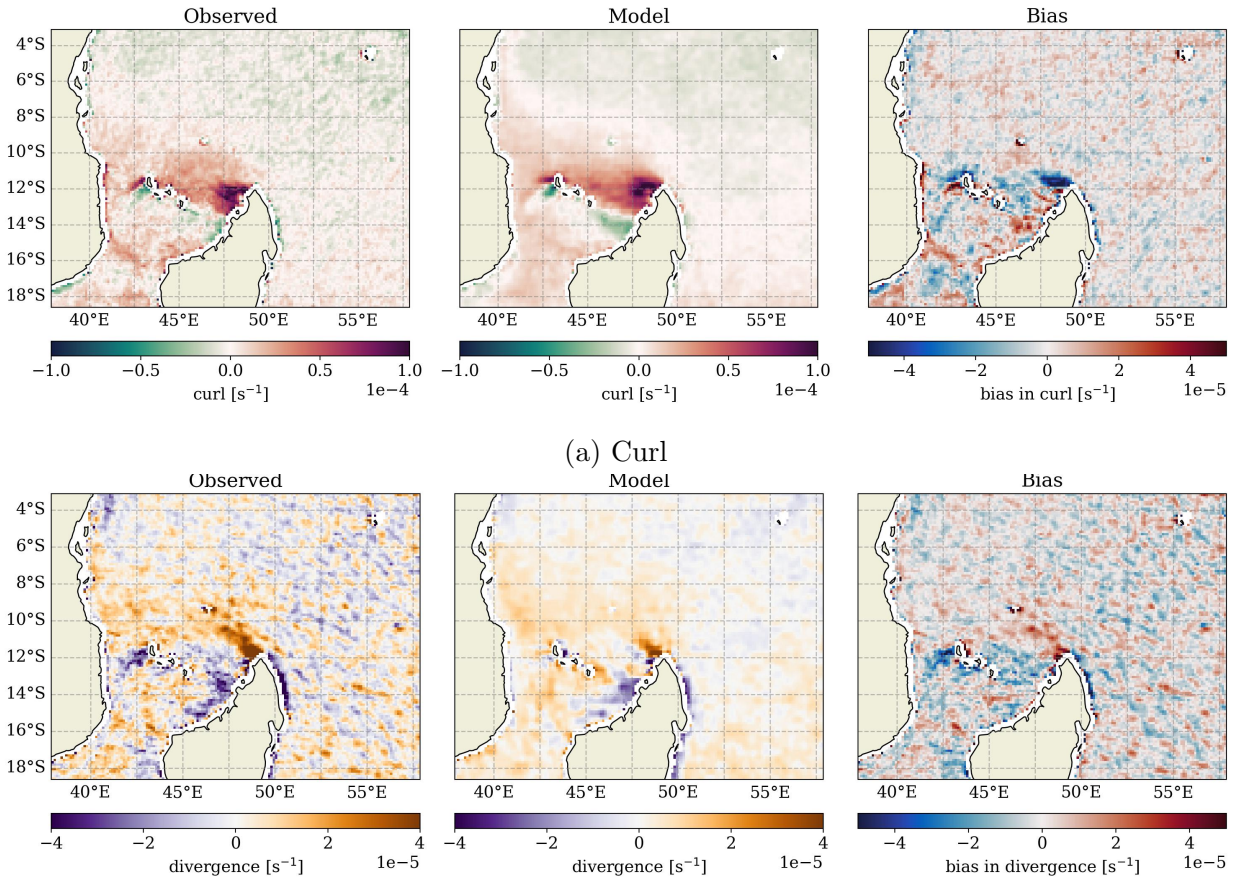

(a) Curl

(b) Divergence

Figure 18: Mean rotation (a) and divergence (b) fields and biases for October 2022 for the northern part of Madagascar. Observations originate from ASCAT measurements of both the ascending and descending orbits of MetOp-B and C.

jets that occur near Southern Greenland and the Irminger Sea. [Våge et al., 2016]

4.3.1 General patterns

Figure 18 shows the general rotation and divergence patterns of the wind near Madagascar. The dominant wind direction over the Indian Ocean near Madagascar is from the southeast. So the mountain range close to the east coast of Madagascar deflects the wind northward. This flow results in turbulence in the form of an island wake, but unlike for Hawaii, the turbulence near Madagascar is not symmetrical and does not result in a vortex street.

The mean wind rotation field of October (Fig. 18a) shows a strong positive rotation on the northwestern side of the tip of the island in both the ASCAT observations and the model fields. They are similar in shape, but the model fields are stronger, resulting in a negative rotation bias on the tip of the island. On the southern flank of the positive rotation wake, between Madagascar and the Comoros (the small islands), there is a net negative rotation field. It is stronger in the model fields, resulting in a positive model bias in this area. Though it is not very visible because of the masking of the ASCAT observations close to land, but

close to the northeastern shore there is also a negative curl present in the observations. This is not fully represented in the model fields, again resulting in a negative bias for this area.

The divergence fields for both observations and the model show that there is strong convergence east and northwest of the island, while there is divergence off the northern tip (Fig. 18b). The model fields in both divergence and convergence are weaker than the ASCAT observations, resulting in a positive bias on the northern tip and a negative bias on the east coast of the island.

Both the convergence and negative curl close to the eastern shore of Madagascar indicate that the southeasterly trades are deflected northward. The strong positive rotation and divergence off the northern tip indicate a turbulent wake. The anticlockwise rotation of this wake is explained by wind shear, the deflected wakes are stronger on the east side of the island than on its lee-side. The negative rotation field between the Comoros and Madagascar can be explained best by the collision of two air masses with opposing wind directions.

The topography of Madagascar is an important factor in the formation and structure of the Findlater Jet, as well as the modulation of the ITCZ in the Indian Ocean. This is shown by Moore [2013], who demonstrated that during the boreal summer months (and by extension October), there is a bifurcation of the air flow around the island. A large part of the trade winds are deflected northward around the island and bend around the northern tip, while a smaller part is deflected southward. This southward flow bends around the southern tip and then moves north again through the Mozambique Channel (west of Madagascar) to rejoin the northern air flow and form the Findlater Jet.

4.4 Case: South of Mexico

As mentioned in Section 1.4.1, the mountain-gap wind named the Tehuano Wind is located South of Mexico. This semi-regular meteorological event occurs most often in winter, hence the focus lies on January 2022 for this case.

4.4.1 General patterns

Similar to the turbulent flow of a jet into a fluid, the flow is expected to be strongly divergent close to the outlet. In both the observations and model fields of the divergence, close to the shore the divergence is strongest (Fig. 19b). The observations and model fields are very similar and do not result in a large bias, apart from the (semi)-random bias due to smoothing in the model.

The rotation is strongest on the sides of the gap wind, since there the flow is decelerated due to wind shear. In case of the Tehuano, there is a strong negative curl on the west side and a strong positive curl on the east side (Fig. 19a). Again, observations and collocated model fields agree very well in this case, so the model biases near the gap do not stand out from the surroundings compared to the monthly means (less than 10% of the mean values).

4.4.2 Specific coordinate analysis

Given that the Tehuano Wind is a semi-regular event, it is prudent to study the time series of the individual measurements as well. Two specific locations were chosen for this analysis.

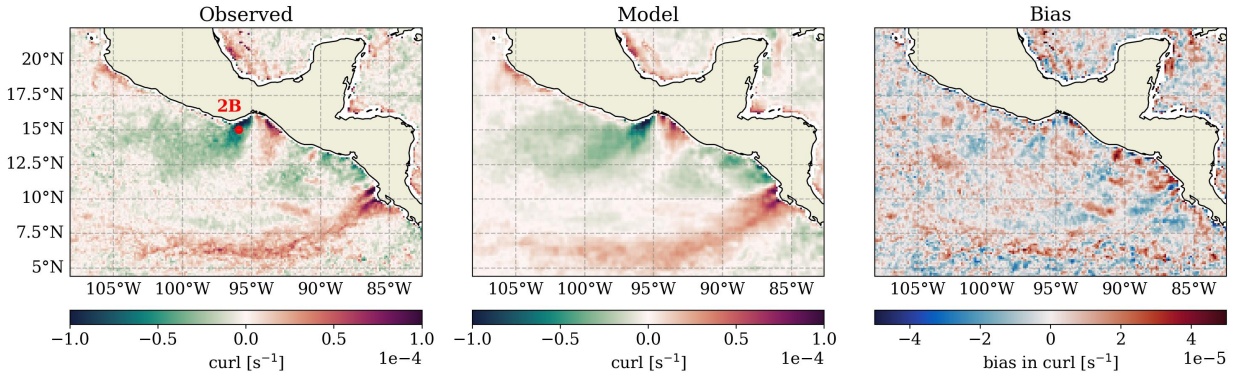

(a) Curl

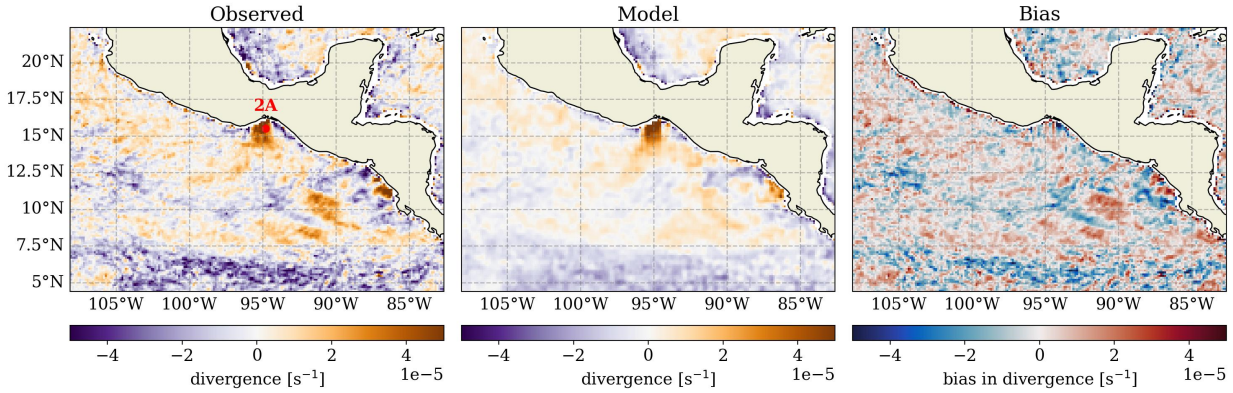

(b) Divergence

Figure 19: Mean rotation (a) and divergence (b) fields and biases for January 2022 of the Pacific Ocean south of Mexico. Observations originate from ASCAT measurements of both the ascending and descending orbits of MetOp-B and C.

The first notable coordinate (2A) is located 50 km due south of the gap, where the divergence is strongest. The second point (2B) is located about 75 km southwest of the gap, focusing on the turbulence that occurs at the sides of the gap wind, in this case the negative rotation wake. (See Fig. 19 for the exact locations of points 2A and 2B)

Five separate gap-wind events can be recognised in the time series of the meridional wind (Fig. 20a). During these events, each with a length of about four days, the winds become strongly negative, reaching values close to -20 m/s at their peak. The divergence becomes more strongly positive during these events (Fig. 20b). The observations from the HY-satellites follow the model values most closely, while the MetOp observations show the most extreme values. The scatterplot of the observations with their collocated model values (Fig. 21a) corroborates this, showing that the linear fits of the HY-satellites lie closer to the $x = y$ line of ideal model fitting.

The time sequence for the rotation, shown in Fig. 20c, also distinguishes the five gap wind events, yet they are slightly harder to see. The observations and model values again match well. HY still matches the model values better (especially HY-2B and 2C, see Fig. 21b)

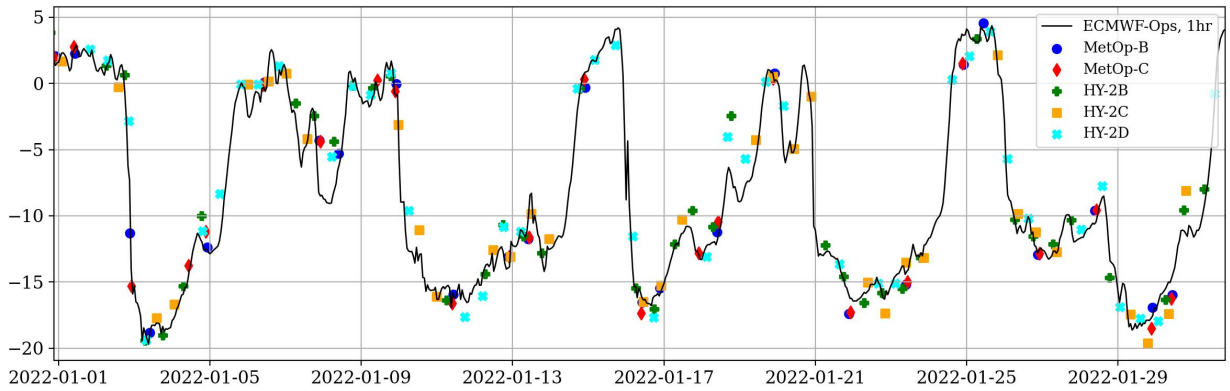

(a) Time series meridional wind (point 2A)

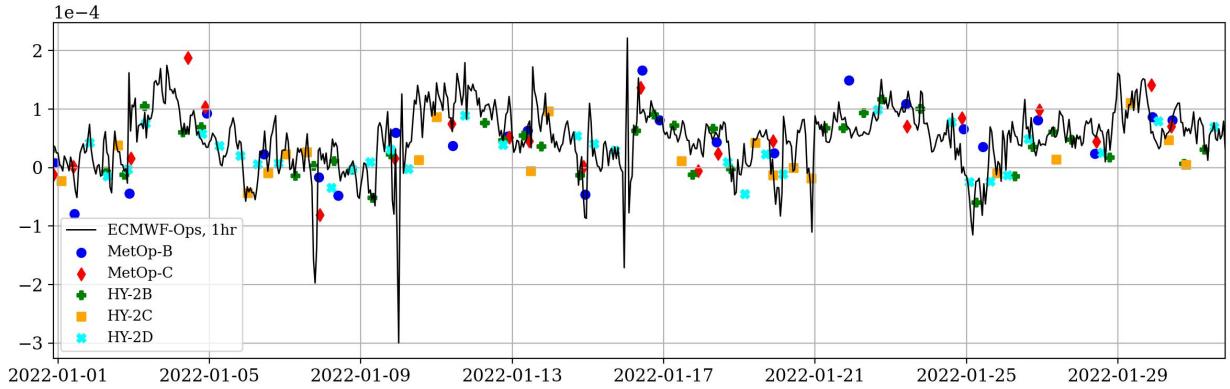

(b) Time series divergence (point 2A)

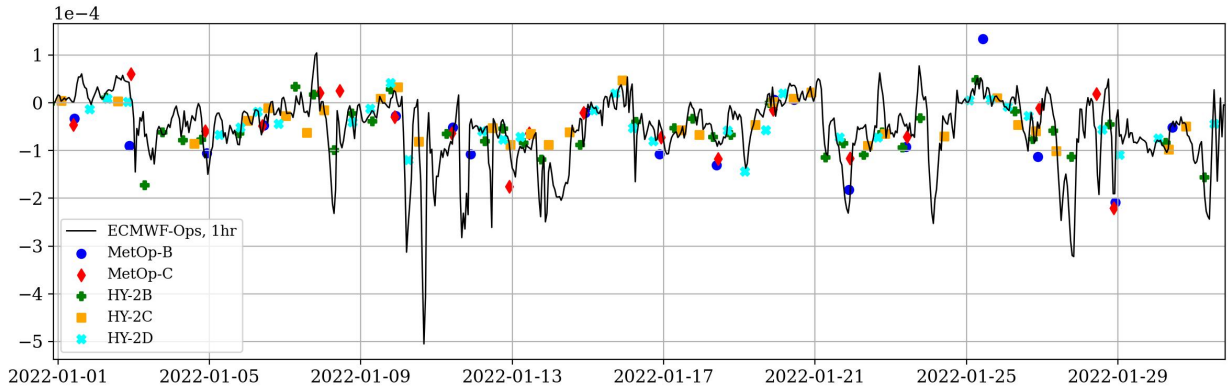

(c) Time series curl (point 2B)

Figure 20: Time series of all scatterometer measurements of two specific locations near the Tehuano Wind for January 2022, along with the time series of the ECMWF-Ops fields. The time series encompass the meridional component of the gap wind 50 km south of the Chivela Pass (location 2A) (a) as well as the divergence (b) and the wind rotation of the gap wake 75 km southwest of the Pass (location 2B) (c).

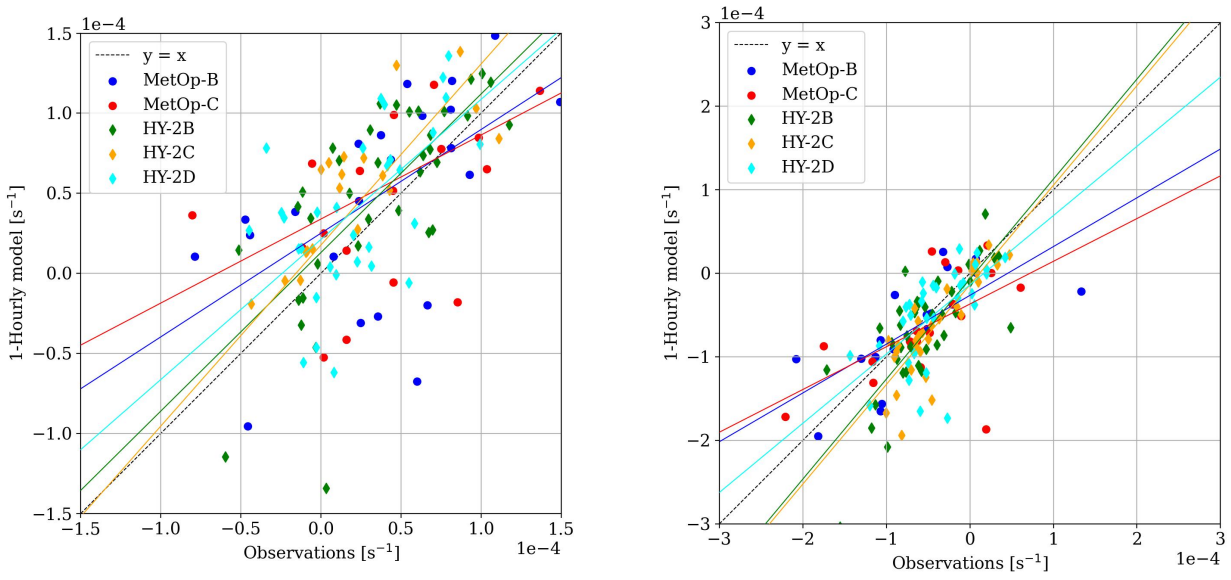

(a) Divergence (point 2A)

(b) Curl (point 2B)

Figure 21: Scatterplots of all observations against their collocated hourly model values of ECMWF-Ops corresponding with the time series of Fig. 20b/c: (a) the divergence and (b) the rotation fields.

The fact that HY correlates better can also be concluded by the calculated correlation coefficients (Table 6), with generally higher correlation values for HY satellites. However, the number of available data points must be taken into account. Since MetOp has a narrower swath, it scans each area less often than HY-satellites do.

4.4.3 SST: Coastal upwelling

Figure 22 shows the observed and modelled SST-fields for the Pacific Ocean south of Mexico as well as the calculated absolute SST-gradient, following Eq. 4. The values correspond with measurements made during the descending orbit of MetOp-B, so they represent the situation of about 9:30 in the morning in January.

It can clearly be seen that the mean SST is lower over the area where the gap-wind rules (Fig.22a). This drop in SST is most likely due to coastal upwelling because the gap wind blows the coastal surface waters seaward, which are then resupplied from deeper ocean layers. The drop in SST is significant: up to about 5 °C in the observations and 3 °C in the model, with respect to surrounding waters. Nevertheless, the bias is not that significant, mainly due to a slight difference in the SST-distributions between observations and the model.

The calculated SST-gradient distribution (Fig. 22b) supports the findings of the SST-fields: a stronger SST-gradient for the observations than for the model and a slightly different distribution. The model is slightly more centered below the gap, while the observations are slightly slanted towards the east.

The slightly eastward slanted upwelling area is also seen by Santiago-García et al. [2019], where they demonstrate that the upwelling due to the Tehuano is actually a upwelling/downwelling

Table 6: Correlation coefficients (r), mean biases (δ) and the number of data points (N) between observations and collocated ECMWF-Ops fields for each specific coordinate of the South Mexico region.

	point 2A, divergence			point 2B, curl		
Satellite	$\boldsymbol{r}$	δ [$\mathbf{10^{-5}}$ $\mathbf{s^{-1}}$]	$\boldsymbol{N}$	$\boldsymbol{r}$	δ [$\mathbf{10^{-5}}$ $\mathbf{s^{-1}}$]	$\boldsymbol{N}$
MetOp-B	0.58	-0.95	24	0.71	-0.17	18
MetOp-C	0.50	-0.86	21	0.56	1.11	19
HY-2B	0.71	-1.26	36	0.69	1.83	39
HY-2C	0.65	-2.02	20	0.85	2.16	32
HY-2D	0.61	-1.80	32	0.64	0.66	32

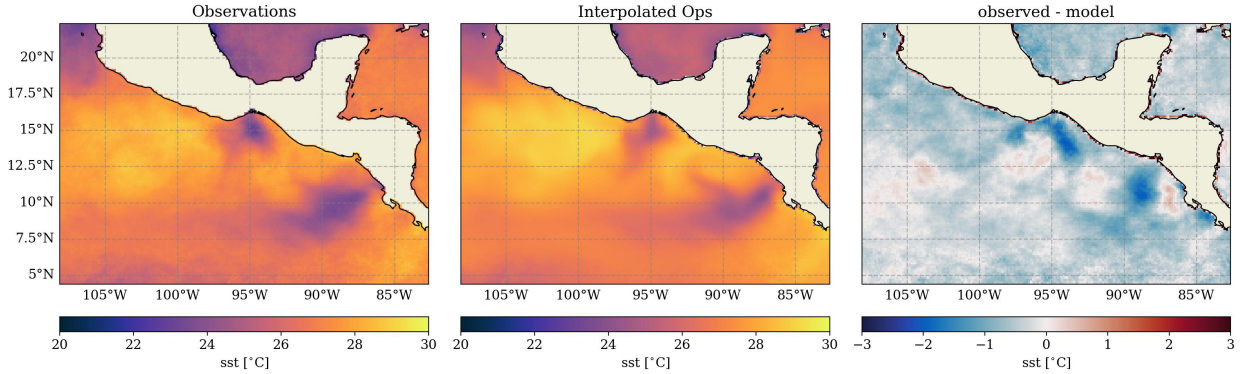

(a) SST

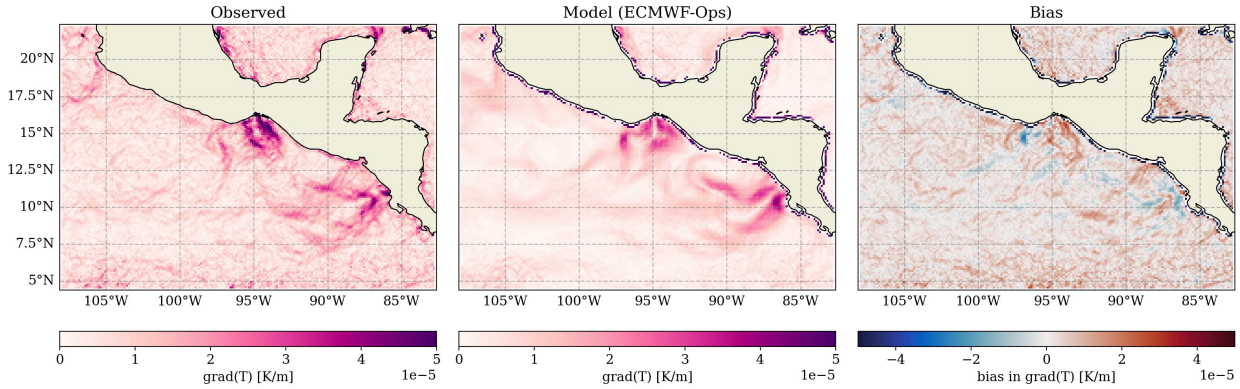

(b) Absolute SST-gradient

Figure 22: The observed and modelled SST-fields and their bias for the Pacific Ocean near the South of Mexico (a) as well as the calculated SST-gradient for these fields (b). The observations are measured by the AVHRR on MetOp-B in the descending orbit and the SST-fields are the average of January 2022

dipole, with downwelling occurring in the anticyclonic eddy (forced by the negative wind curl on the west side of the gap wind) and upwelling in the cyclonic eddy (forced by the positive

wind curl on the east side).

4.5 Case: Hawaii

As mentioned in Section 3.2.1, the island chain of Hawaii is a special place where there is a combination of turbulent wakes on the lee-side of the islands and gap winds in the channels between them. These are all induced by the northeasterly trade winds, which are strongest in July.

For easier reference: the five largest islands from west to east are Kauai, Oahu, Molokai, Maui and the Isle of Hawaii (generally known as Big Island).

4.5.1 General patterns

The prevailing northeastern winds in the subtropical Pacific are blocked and broken by the islands of Hawaii, resulting in a turbulent wake behind each of the islands (Fig. 23). Turbulence in fluid flows is most clearly visible in the rotation fields, since fluid motion is circular by nature.

Figure 23a shows an alternating band of positive and negative rotation on the leeward (southwestern) side of the islands, extending more than 300 km behind the islands. This is found for both the observed and model fields, though the observed rotation reaches farther than the rotation in the model fields. When looking in the same direction as the flow, the positive (anticlockwise) rotation is found behind the right side of the wake while a negative (clockwise) rotation is found on the left side. This pattern clearly indicates the presence of von Kármán vortices behind each island (see Fig. 6c in Section 1.3.1). The strength of the rotation patterns is similar for both the observations and model values, mainly in the wake of Big Island. The modelled wakes behind Maui/Molokai and Kauai are slightly stronger while the model wake behind Oahu is slightly weaker. Apart from these facts, the observed wakes also reach a little bit farther compared to the model wakes. Another difference is that the wakes in the model fields, especially in case of Big Island, are oriented slightly more westward in the model fields. This results in some strong positive biases locally, close to the islands.

An in situ measurement series of the wind wakes behind Kauai and Oahu has been done by Yang et al. [2008]. Several cruises with continuous wind measurements were done behind each island. The results of this study agree with the ASCAT measurements of July 2022, including the direction of the wake and the vortex patterns involved.

The divergence fields for July are shown in Figure 23b. In the observations, there is a strong trail of convergence leeward of each island, also stretching out for up to 300 km behind Big Island, just like the rotation wake. Just behind the straits, especially between Big Island and Maui, there is significant divergence, which is partly obscured by the data-mask close to the shores. These strong convergence and divergence patterns are not found in the collocated model fields, where there is only weak convergence on the south side of Big Island and a bit of divergence near the straits. This difference between observed and modelled fields results in a very significant bias in the divergence: negative in the wakes of the islands and positive in between.

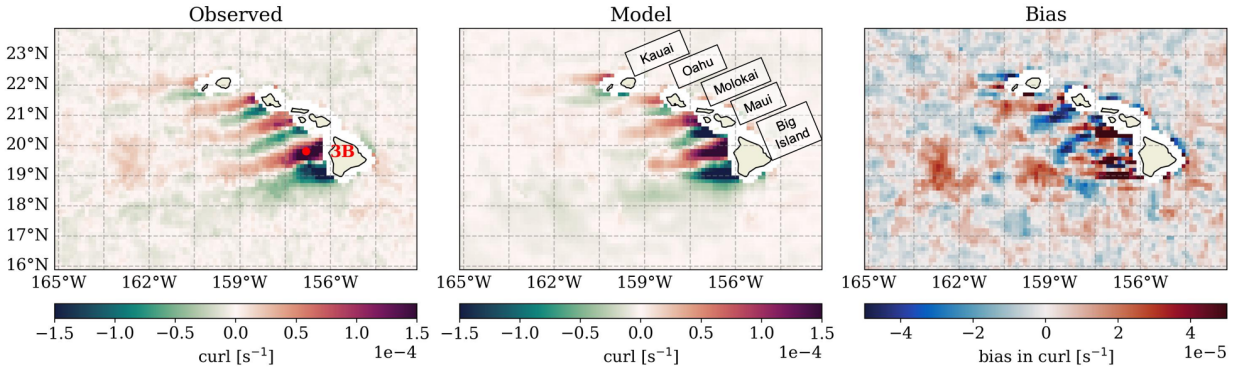

(a) Curl

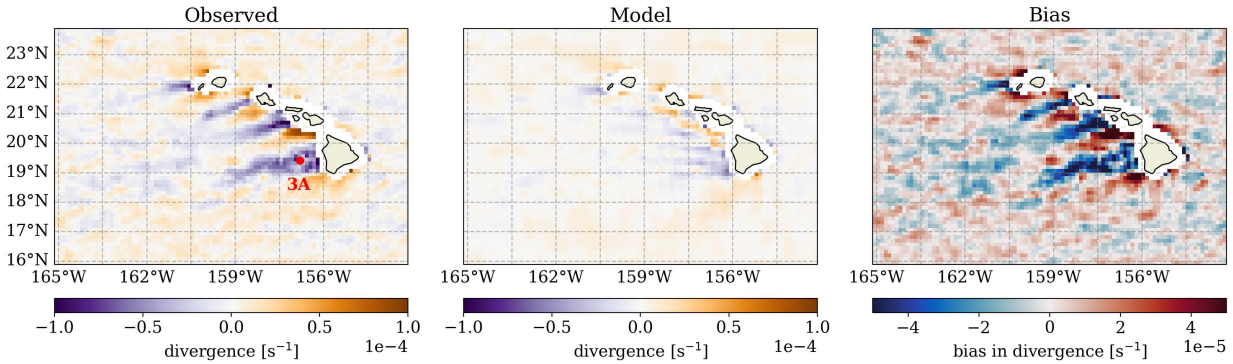

(b) Divergence

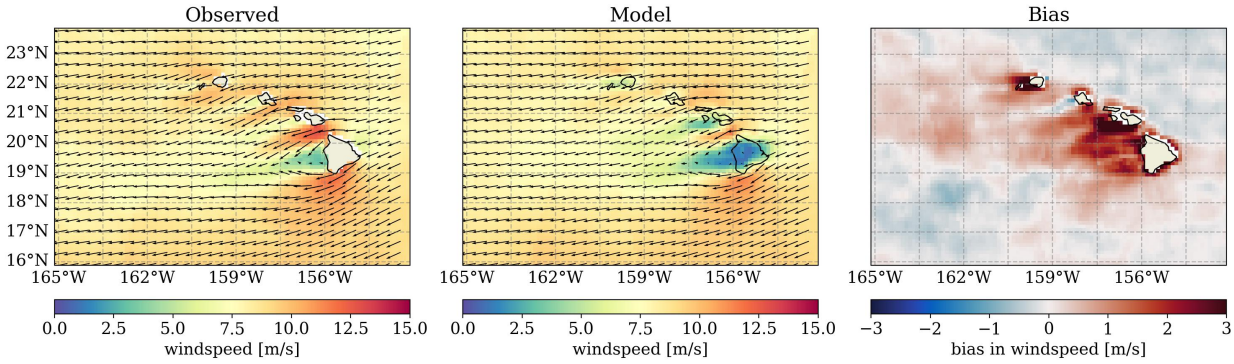

(c) Wind speed and vectors

Figure 23: Mean rotation (a), divergence (b) and wind vector fields (c) and their biases for July 2022 of the Pacific Ocean near Hawaii. Observations originate from ASCAT measurements of both the ascending and descending orbits of MetOp-B and C.

The strong divergence near the channels, together with the strong wind acceleration (Fig. 23c) indicate the presence of gap winds. These gap winds between the islands are also studied by Hitzl et al. [2014], where they focused on the Alenuihāhā Channel between Big Island and Maui. They combined numerical simulations with observations from NASA's QuikSCAT scatterometer and in situ measurements. The 2 km resolution model they used was able to resolve the wind field accurately, which is not the case for ECMWF-Ops as they underestimate the acceleration of the gap wind in the channel (Fig. 23c). This underestimation is likely a problem caused by the lower resolution of the ECMWF-Ops model. It is still notable, since in the previous case (the Tehuano Wind near Mexico), it was proven that the model can accurately model gap winds.

4.5.2 Specific coordinate analysis

The first coordinate of interest for Hawaii is located in the wake of Big Island (3A, see Fig. 23b), in the center of the divergence trail. In Figure 24a, divergence observations of all satellites are plotted as a function of measurement time, as well as the hourly ECMWF model fields. The first thing to note is that the ASCAT measurements, and especially those

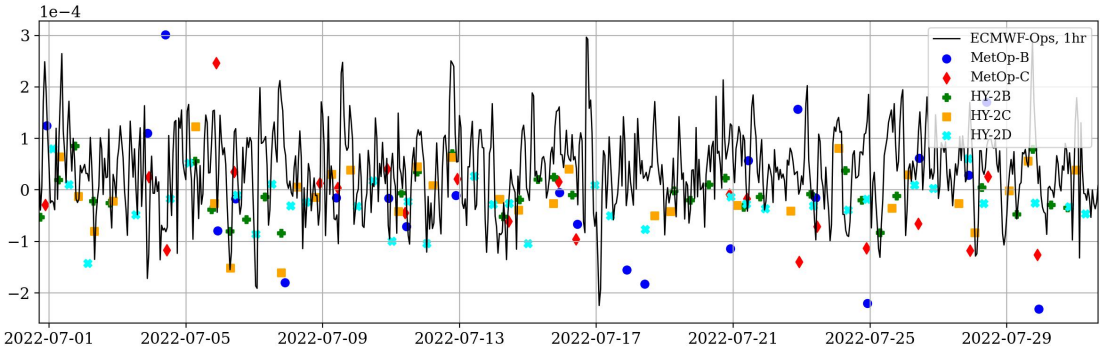

(a) Time series divergence (point 3A)

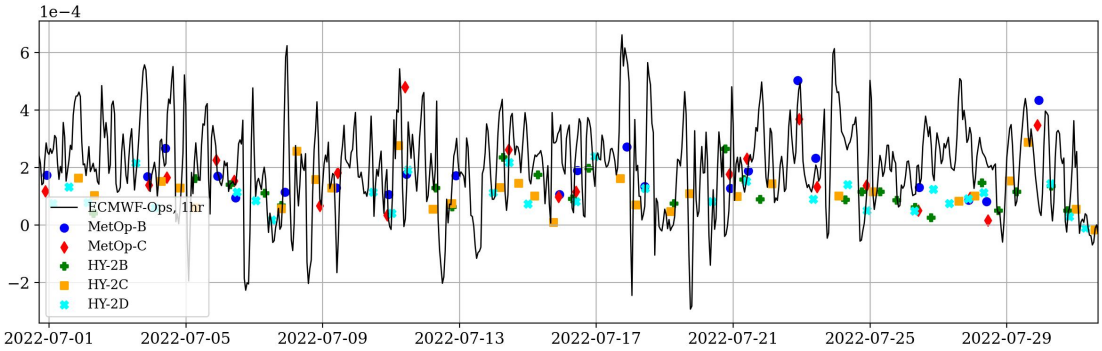

(b) Time series curl (point 3B)

Figure 24: Time series of all scatterometer measurements of specific locations in the wake of Big Islands, covering July 2022, along with the time series of the ECMWF-Ops field. The time series of location 3A is the divergence (a) and for location 3B, the focus lies on the rotation (b).

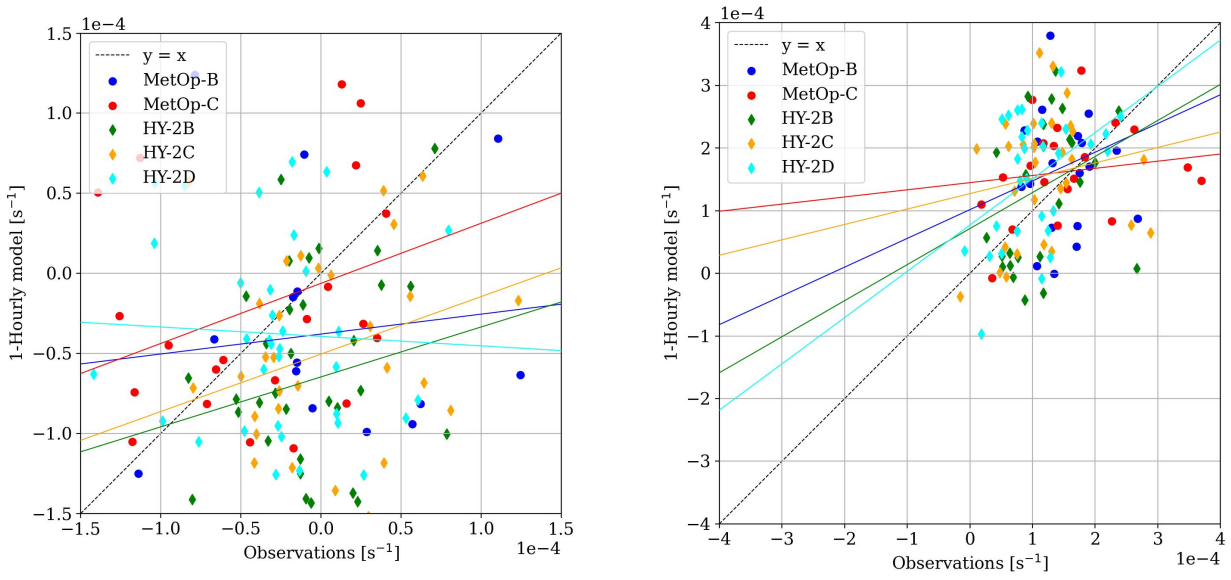

(a) Divergence (point 3A)

(b) Curl (point 3B)

Figure 25: Scatterplots of all observations against their collocated hourly model values of ECMWF-Ops corresponding with the time series of Fig. 24: (a) the divergence and (b) the rotation fields.

of MetOp-B, show the most extreme values, which would result in large biases. The HY-satellites stick closer to the model values. Most observations are slightly lower than the modelled values, which are highly variable around zero.

In locations where the divergence is high, rotation is usually lower and vice versa. So, the second location of interest for Hawaii (3B), with the focus on the wind rotation, is positioned at the same longitude as the first location, but slightly north of it, such that it is positioned in the middle of the positive rotation trail behind Big Island (Fig. 24b). At this location the observations match the model fields well, both are predominantly positive, but the observations are again slightly weaker and show a little less variability. Though to a lesser extent than for the divergence in the previous case, MetOp-B again shows the most extreme values.

The high variability in the model fields of the wind divergence and rotation at both locations can be explained by different turbulent vortices passing over. These fluctuations of the model fields also make it difficult to compare them with the observations accurately except for the most general patterns. Therefore, a closer comparison of the observations with their collocated model values is necessary. Figure 25 shows the scatterplots that correspond to the time series of Figure 24.

The scatterplot of the divergence time series (Fig. 25a) shows that the observations and the model data do not match well at all, which is not at all surprising, since it was previously demonstrated that the operational model does not resolve wind convergence well (Fig. 23b). In this instance, the Haiyangs perform worse than ASCAT of MetOp-C. This is reinforced by the correlation coefficients for each satellite, found in Table 7. A linear fit of the MetOp-C data with the model fields yields a slope closest to the $y = x$ line, has the lowest systematic

bias and has the highest correlation coefficient ($r = 0.43$). It should be noted though that the number of observations of MetOp-C at this location is also the lowest at 22 data points for July 2022.

The scatterplot for the wind rotation time series at location 3B (Fig. 25b) shows a little less spread, compared to the divergence, with the observations and model values mostly having the same sign. Still, the linear fits and correlations are far from ideal. The values of r range from 0.17 (HY-2B) to 0.43 (HY-2D and MetOp-B). Given that HY-2D also has the regression coefficient that is closest to 1 (0.74), it shows that this satellite performs best in this case.

Table 7: Correlation coefficients (r), mean biases (δ) and the number of data points (N) between observations and collocated ECMWF-Ops fields per satellite for each specific coordinate of the Hawaiian region.

	point 3A, divergence			point 3B, curl		
Satellite	$\boldsymbol{r}$	δ [$\mathbf{10^{-5}}$ $\mathbf{s^{-1}}$]	$\boldsymbol{N}$	$\boldsymbol{r}$	δ [$\mathbf{10^{-5}}$ $\mathbf{s^{-1}}$]	$\boldsymbol{N}$
MetOp-B	0.24	2.40	23	0.43	-0.13	22
MetOp-C	0.43	-1.01	22	0.18	0.79	21
HY-2B	0.21	5.90	35	0.27	-2.20	26
HY-2C	0.35	4.51	32	0.17	-3.79	30
HY-2D	-0.04	1.27	36	0.43	-4.96	30

4.5.3 Model Topography

The turbulent wake and von Kármán vortex streets behind the islands of Hawaii are topography-induced: the trade winds are broken by the mountainous islands. If the model orography is inaccurate, this could well result in a very different wake.

In Figure 26, the orographies of the ECMWF model (a), the high resolution ETOPO model (b) and the difference between them (c) are plotted. Given the high resolution of the ETOPO model, these values can be seen as an approximation of the observed surface height. The difference in Fig. 26c is defined as ETOPO minus ECMWF-Ops values.

Before the different orographies are compared, it should be noted that at a 0.125° resolution, the islands of Molokai and Maui (together with the smaller island of Lanai) appear as one larger island in both models, which could be the reason of the stronger wake behind these islands in the model fields, and the strong resulting biases.

There are some significant differences between the orographies of two models (Fig. 26c). In some grid cells, mainly on Big Island and Maui, the difference in surface height is as large as 500 m in favour of the HR model. Given that the Mauna Kea at Big Island is 4207 m high, this is quite significant. Some locations on Big Island and Maui show a bias in favour of the ECMWF model of about 200 m. Finally, it is shown that the orography of Kauai is significantly lower in the operational model.

From these results, it can be concluded that the orography of the islands is smoothed significantly in the ECMWF model. This would undoubtedly influence the turbulent air flows around the islands, but it is not likely that it would cause large-scale biases. However,

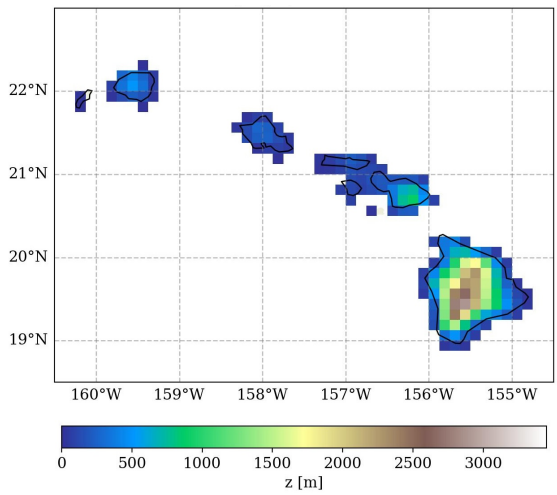

(a) ECMWF-Ops

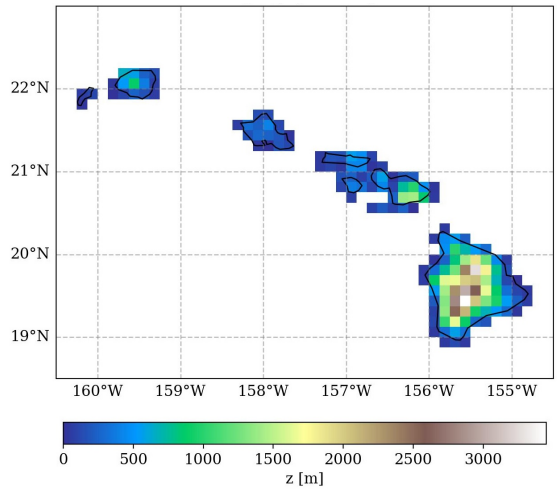

(b) ETOPO – reshaped

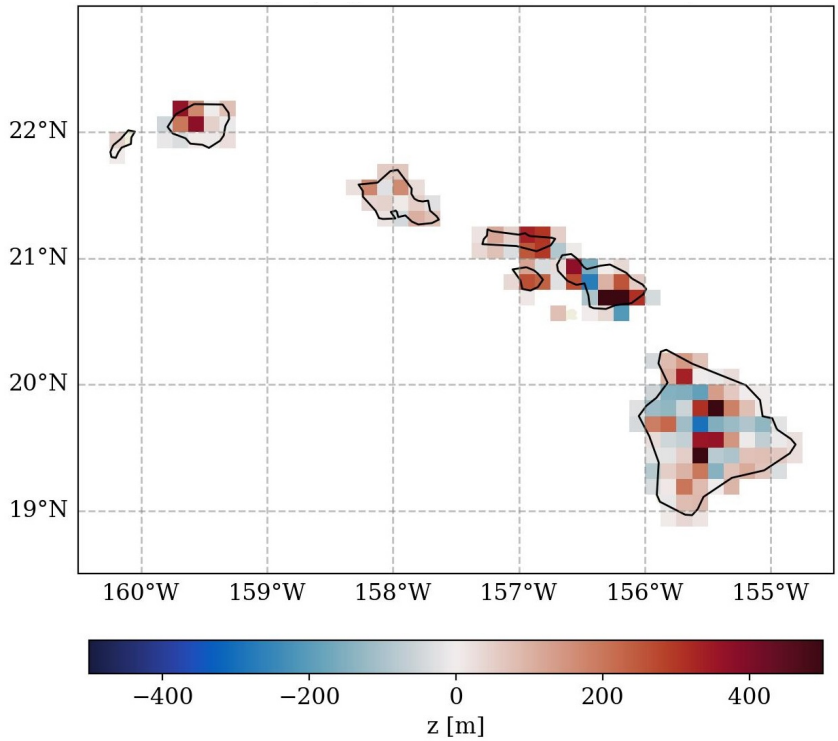

(c) Bias (ETOPO - ECMWF)

Figure 26: Orography from the ECMWF model (a), the high-resolution ETOPO model (b) and the difference between the two orographies. All models are reshaped to a 0.125° resolution.

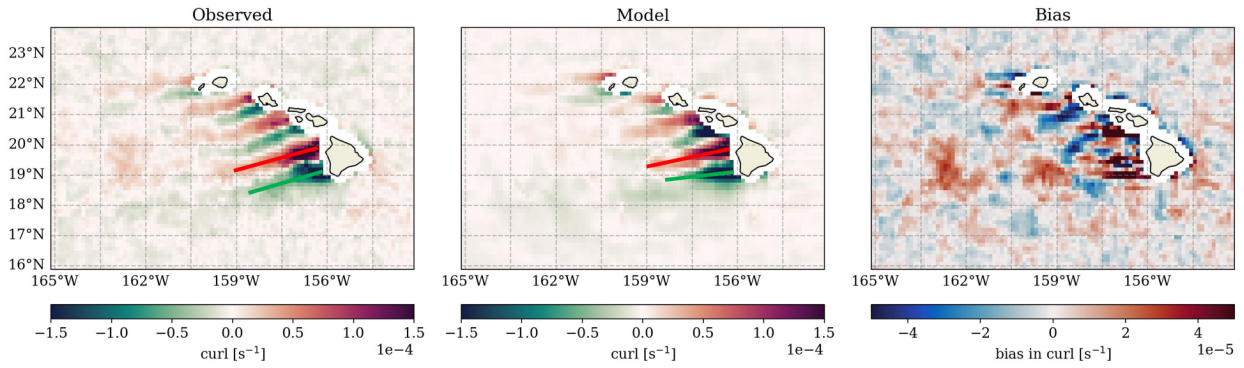

Figure 27: Mean rotation fields and biases for July 2022 of the Pacific Ocean near Hawaii, measured by ASCAT for both orbits. The orientations of the turbulent wakes of Big Island in the observations and model fields are indicated.

it may be the cause for the small difference in orientation of the wakes behind the island. As seen in Fig. 27, the modelled curl in the wake of Big Island is oriented slightly more westward compared to observations. This westward orientation is stronger in the negative curl part of the modelled wake. These different orientations of the turbulent wake cause the irregular biases on the lee-side of Big Island.

4.6 Case: The Western North Atlantic

In the Western North Atlantic, the motion of the atmosphere is heavily influenced by the sea. The Gulf Stream stimulates the formation of fronts and depressions in the North Atlantic storm track, and the SST-gradient of the Gulf Stream itself also influences the flow of the surface winds.

4.6.1 General patterns

Figure 28 shows the mean rotation and divergence fields of the Western North Atlantic for April 2022. Starting with the rotation (Fig. 28a), it can be seen that the background rotation is negative as explained by the general atmospheric circulation (Section 1.1.1). In the observations, there is a narrow band of strong negative and positive rotation running parallel to the coastline of the US East Coast. This band of positive and negative rotation is positioned roughly over the Gulf Stream and is not found in the collocated model fields, resulting in a strong bias just off the US East Coast. Further north, along the storm track around 40° N, there are a lot of clusters of positive wind curl. They are more defined in the observations and smoothed out in the modelled fields, resulting in some stronger biases over the storm track.

It should be mentioned that near the American cities Washington DC, New York and Boston (between 35° and 40° N), there is a lot of radio-interference. Both large harbour radars and radio reflectance on large skyscrapers distort the signal of ASCAT. These contaminated data points are filtered out in processing, but have as result that the number of valid data

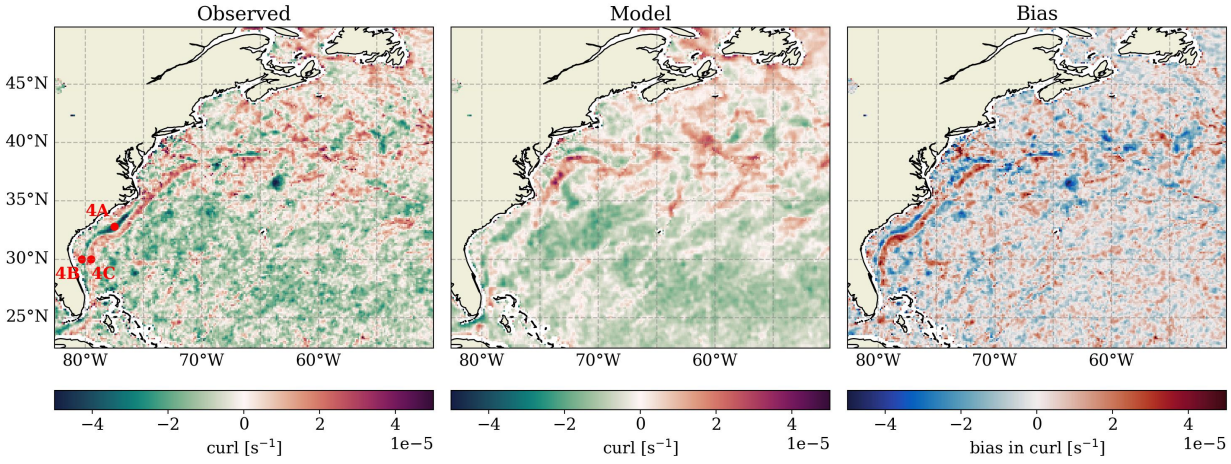

(a) Curl

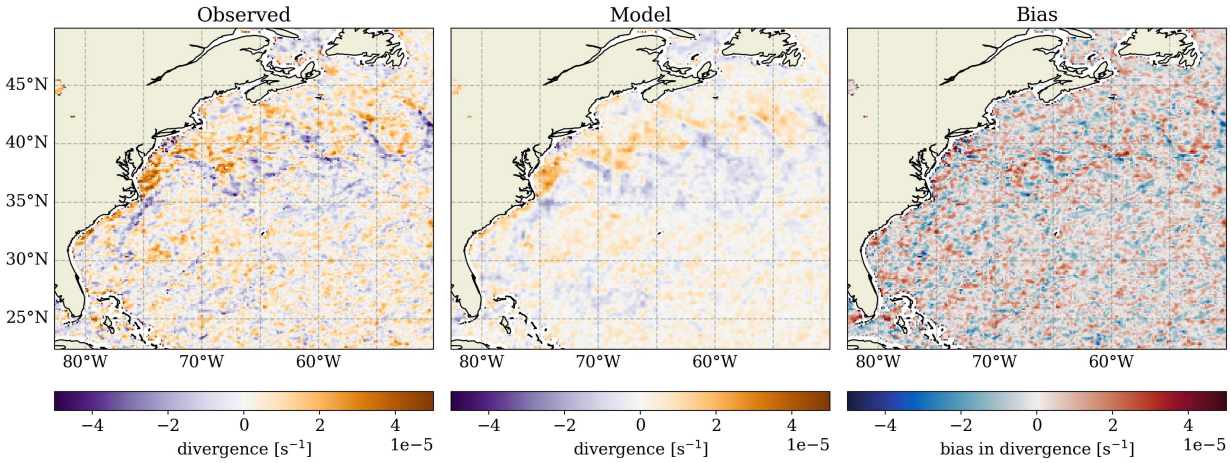

(b) Divergence

Figure 28: Mean rotation (a) and divergence (b) fields and biases for April 2022 for the Western part of the North Atlantic. Observations originate from ASCAT measurements of both the ascending and descending orbits of MetOp-B and C.

points in this region is significantly lower. It's range mostly misses the curl-band, but it should still be mentioned. The exact distributions can be seen in Appendix C (Fig. 41).

The divergence fields display strong convergence along the storm track (Fig. 28b), a good indication of weather fronts and atmospheric low pressure areas (along with the positive rotation from the previous paragraph). Overall, the patterns are similar between observations and model, but the model shows again weaker divergence and is smoothed. The divergence bias is not clearly defined over the whole region, yet slightly stronger over the storm track.

Table 8: Regression slopes (α), correlation coefficients (r), mean biases (δ) and the number of data points (N) between observations and collocated ECMWF-Ops rotation fields per satellite for each specific coordinate of the Western North Atlantic. The [*] signifies the scale and unit of the bias: [10^{-5} s^{-1}].

	Point 4A				Point 4B				Point 4C			
Satellite	$\boldsymbol{\alpha}$	$\boldsymbol{r}$	δ [*]	$\boldsymbol{N}$	$\boldsymbol{\alpha}$	$\boldsymbol{r}$	δ [*]	$\boldsymbol{N}$	$\boldsymbol{\alpha}$	$\boldsymbol{r}$	δ [*]	$\boldsymbol{N}$
MetOp-B	0.411	0.70	-2.89	24	0.174	0.20	-2.96	25	0.120	0.16	2.39	24
MetOp-C	0.187	0.32	-1.89	25	0.718	0.73	-3.28	26	0.329	0.39	1.84	24
HY-2B	0.673	0.51	-0.98	37	0.486	0.51	-0.29	23	0.620	0.67	1.38	36
HY-2C	0.629	0.64	-0.64	40	0.720	0.61	-0.27	21	1.156	0.73	0.05	45
HY-2D	0.497	0.49	-1.24	42	0.652	0.68	0.46	18	0.925	0.79	0.55	37

4.6.2 Specific coordinate analysis

In the Gulf Stream Region, the biases in the curl are most significant, as was shown in the previous section. Thus, a closer analysis of specific coordinates on this 'curl-band' near the Gulf Stream is performed. Three points of interest are chosen in this case: two in the negative part of the band (at 33.5° N and 30° N, locations 4A and 4B respectively) and one in the positive part (location 4C, 80 km east of location 4B). The measured and modelled rotation of these locations are plotted as function of time for the month April (Fig. 29).

Comparing the three rotation time series, the first thing that stands out is that ASCAT observations again show more extreme values. They are more strongly negative in case of points 4A and 4B and more positive in case of point 4C. The Haiyang observations follow the model more closely, yet they still tend to be slightly lower than the model fields in case of points 4A and 4B, and slightly higher in case of point 4C.

These findings are further reinforced by the linear regression statistics (Table 8). The regression slopes of the HY satellites are closer to 1 for all points and the correlation coefficients are usually higher as well. For location 4B, however, MetOp-C observations fit best with their collocated model values, with both a slope close to 1 ($\alpha = 0.718$) and the highest correlation coefficient for this location ($r = 0.73$). It should be noted however, that for that same location, the number of valid data points for the HY satellites is significantly lower compared to the other locations. This is probably caused by the coastal masking, which filters out extreme values near the shores and over land lest they interfere with the rest of the data.

4.6.3 SST: air-sea coupling

Because air-sea interactions are an important part of the atmospheric dynamics in the Western North Atlantic, the SST fields of both satellite observations and the operational model first need to be studied before it can be coupled to the near-surface wind fields.

In both the observations and model fields of the SST in April 2022 (Fig. 30a), the Gulf Stream can clearly be distinguished along the US East Coast. Water of about 25 °C is transported from the Gulf of Mexico, along the coast until it detaches from the continent at 35° N and then meanders eastwards. It forms a barrier between the cold waters in the north

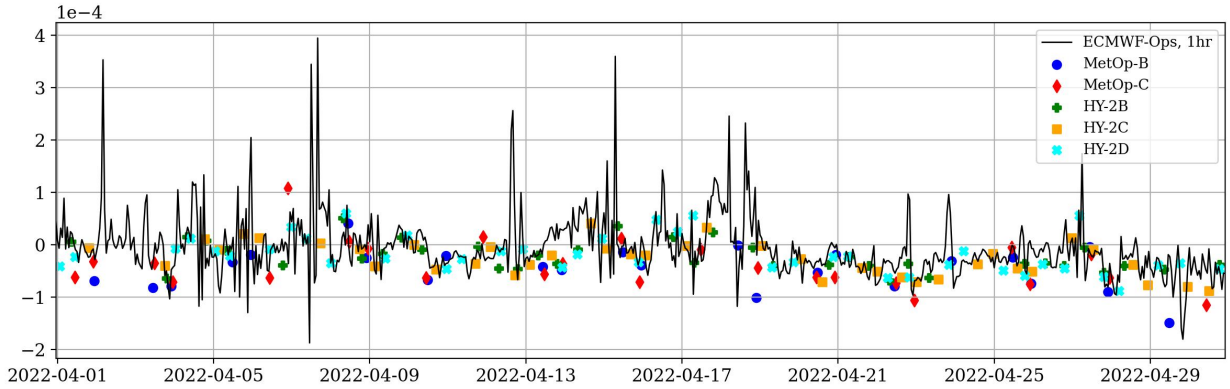

(a) Point 4A

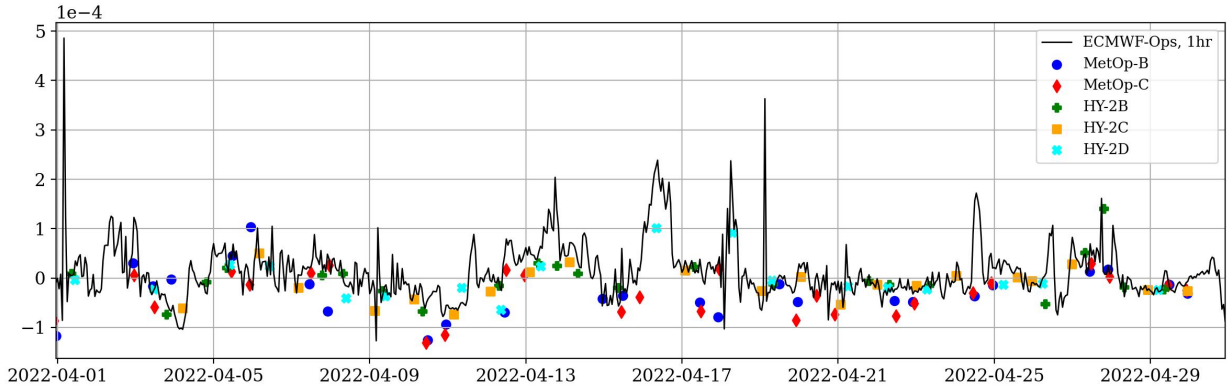

(b) Point 4B

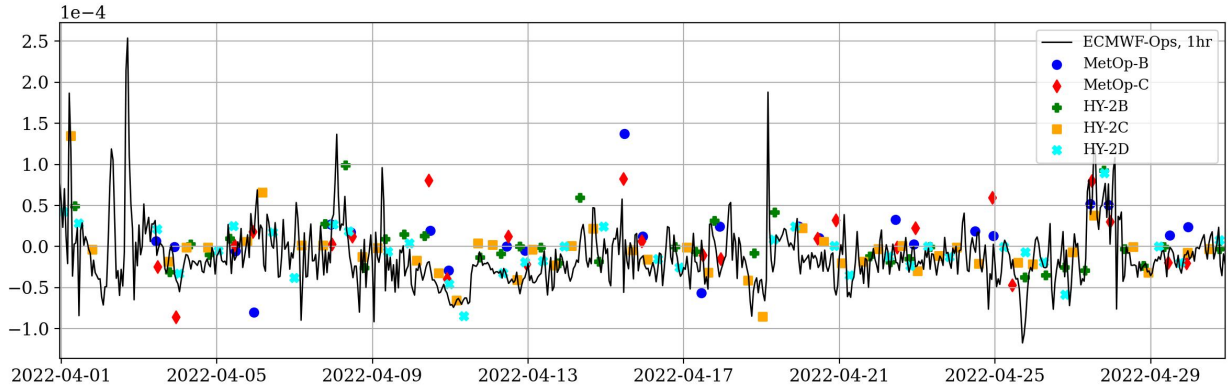

(c) Point 4C

Figure 29: Time series of all scatterometer measurements from April 2022 of specific locations on the rotation band in the Gulf Stream area, along with the time series of the ECMWF-Ops field. Points 4A (a) and 4B (b) are located on the negative side of the rotation band, while point 4C (c) is located on the positive side.

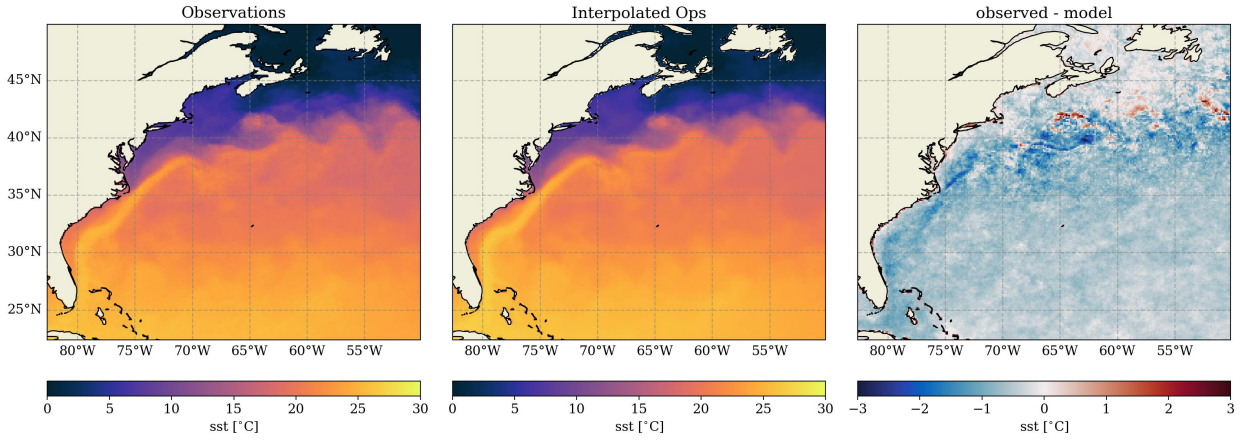

(a) SST

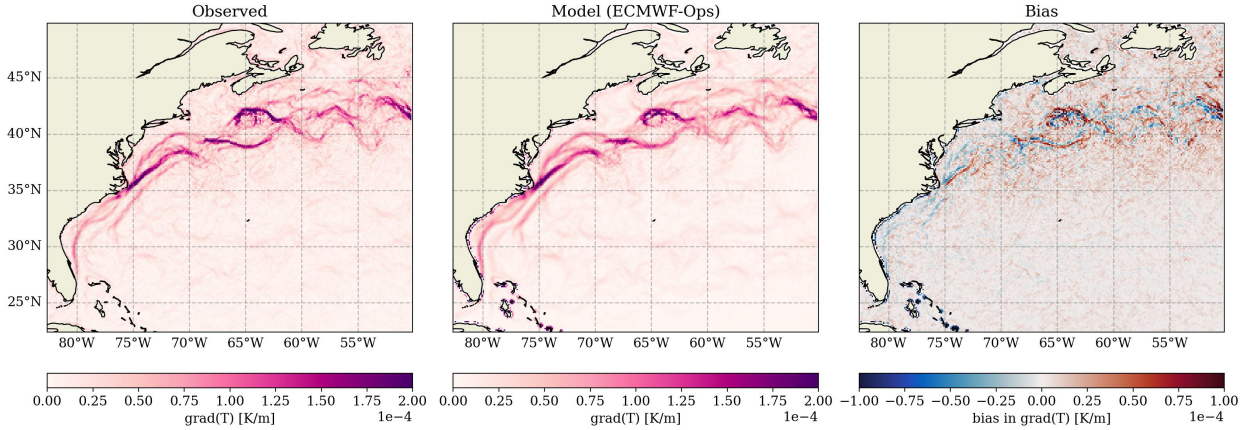

(b) Absolute SST-gradient

Figure 30: The observed and modelled SST-fields and their bias for the Western North Atlantic (a) as well as the calculated SST-gradient for these fields (b). The observations are measured by the AVHRR sensor on MetOp-B in the descending orbit. The SST-fields are the average of April 2022.

and the warmer waters of the subtropical Atlantic. Between the model and observations no significant differences can be found where the Gulf Stream is still attached to the continent, the observed Gulf Stream only appears slightly colder than the modelled one, but the biases are minor. There are some strong local biases in the eastward track after detachment, but that is to be expected, since the Gulf Stream creates eddies and meanders here so some slight variations are bound to occur.

Please note that there is a background bias in the SST of about -0.5 °C (average over the domain [65° - 50°W, 23° - 35°N]) in favour of the model, meaning that observations in the SST are slightly lower compared to the model fields. This is the case for the SST bias of both regions studied (Fig. 22a and Fig. 30a). These background biases likely developed because the SST-sensor measures the temperature at around 0.2 m depth, while the definition of SST

from the ECMWF is the average temperature of the top 1.5 m of the ocean. Also keep in mind that the measurements are from MetOp-B, a Sun-synchronous satellite that passes over at 9:30 AM local time each day, which means that the upper layer of the ocean has been cooling overnight. Nevertheless, a constant bias of -0.5 °C is still substantial.

Figure 30b shows the calculated absolute SST-gradient (a plot of its zonal and meridional components separately can be found in Fig. 42 of Appendix D). Again, in the area where the largest biases in the rotation occur, the part of the Gulf Stream that is still attached to the continent, there are no significant biases, only showing that the observed gradients are slightly weaker, since the observed SST was lower as well. The meandering part of the Gulf Stream does show some strong local SST-gradient biases in the same locations where the SST-biases are found.

As was first noted when discussing the general patterns of the wind rotation fields of the Western North Atlantic, the strong dual curl-band near the US East Coast appears to be positioned roughly over the attached part of the Gulf Stream (Fig. 28a in Section 4.6.1). Plotting the contours of the absolute SST-gradient over the mean rotation fields shows that they do indeed fit very well together for the observations (Fig. 31). Focusing on the attached part of the Gulf Stream, the strong SST-gradients are positioned on either side of the positive part of the rotation band, and directly over the negative rotation part of the band on the west-side. This is not seen in the model fields, even though the SST-gradients follow the same pattern.

The wind vector response to a positive SST-gradient on the NH is to accelerate and deflect to the right (negative rotation), while its response to a negative SST-gradient is to decelerate and deflect to the left (positive rotation, see Fig. 9 and Section 1.4.3). Taking a closer look at the attached part of the curl-band (Fig. 32) and focusing on the area around 33° N, it can be seen that the mean north wind is first deflected westward as it passes over a positive SST-gradient, resulting in the negative part of the rotation band. Then, when it crosses the negative SST-gradient, the wind is deflected eastward, creating the positive part of the rotation band. These motions are in line with the air-sea coupling described by O'Neill et al. [2010]. It can thus be concluded that this coupling most likely occurs over large parts of the Gulf Stream.

While the mean wind flow of the model is similar to the observations, it does not follow the same mechanism of air-sea coupling as seen in the observations when passing over strong SST-gradients. This shows that the air-sea coupling is not fully resolved in the ECMWF operational model, resulting in the large bias that was found.

This is further reinforced by the work of Tsartsali et al. [2022], where they computed the correlations between the wind stress divergence and downwind SST-gradient anomalies as a measure of air-sea coupling. They performed this for different types of NWP models, including ECMWF-Ops at a 0.25° resolution. They showed that there is a strong correlation present over the Storm track (detached part of the Gulf Stream), yet no correlation over the attached part of the Gulf Stream, further underlining the incompleteness of the air-sea coupling in the ECMWF operational model.

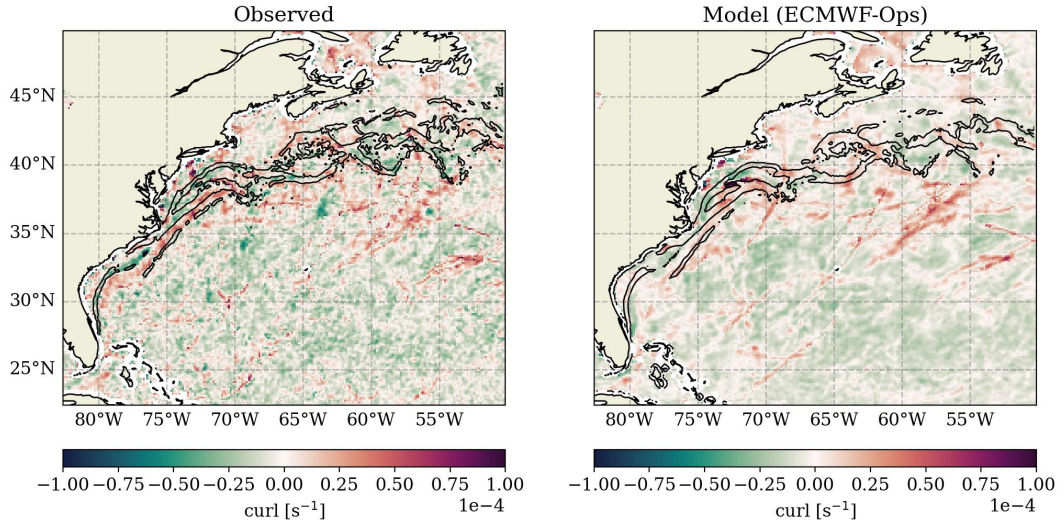

Figure 31: Mean observed and modelled wind curl for April 2022. The contours show the absolute SST-gradient for the same month at the level 6.0×10^{-5} K/m. Observations are from the descending orbit of MetOp-B (ASCAT for rotation and AVHRR for SST-gradients).

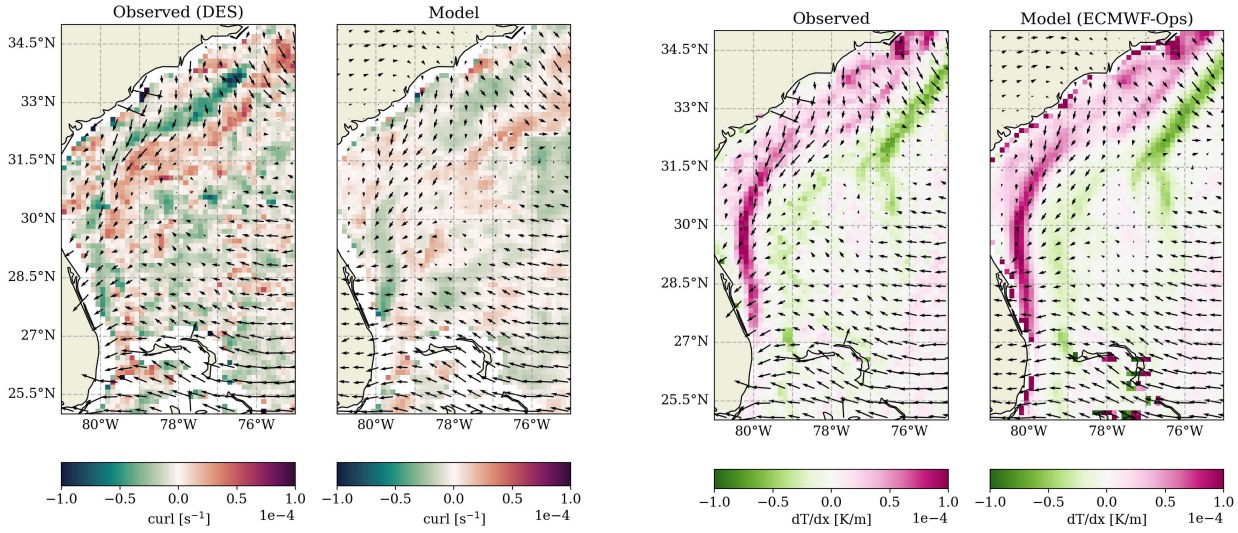

(a) vorticity and wind vector field

(b) $\partial T/\partial x$ and wind vector field

Figure 32: Close-up of the lower part of the Gulf Stream, just off the coast of Florida. Again observations are from the descending orbit of MetOp-B versus the collocated model fields from ECMWF-Ops. Subfigure (a) shows the mean rotation and wind vector field, while (b) shows the mean zonal SST-gradient and wind vector field.

4.7 Interpolation analysis

This final section of the results discusses the effects of different interpolation schemes that are used in this project. As explained before, the modelled fields in the Level 3 wind products from KNMI are collocated to the measurements during the L2-phase, so an additional spatial interpolation is performed on these fields. Therefore, they are compared with ECMWF-Ops fields that are collocated with the observations when they are already on the same grid as the L3 product. The fields that are studied in this section are the monthly mean rotation fields. For completeness, the monthly mean for the complete operational model dataset is also included.

In this section, when discussing the L3 model fields, the collocated model fields that are included in KNMI's Level 3 product are meant. When discussing the collocated or interpolated ECMWF-Ops fields, the collocated fields from the hourly operational model, performed for this study, are meant.

Figure 33 shows the monthly mean morning values (descending orbit, MetOp-B) of the rotation for July near Hawaii. The mean fields of the observations (a), the collocated model values from the L3 wind product (b), the complete hourly ECMWF-Ops model field (c) and the collocated values from the ECMWF-operational model (d) are plotted respectively.

It can be seen that apart from some low level noise in the interpolated operational model the differences between two collocated models are minimal. This noise originates from the spatial derivative calculation procedure of KNMI while converting the model from a Gaussian grid to a regular lat-lon grid. There is some more detail in the interpolated ECMWF-Ops fields, however, compared to the fields of the L3 model. Comparing all mean fields with the complete dataset (c) clearly shows the effect of collocation. The wakes are all very straight and there is hardly any background rotation present, unlike in the observations and the collocated models.

The same procedure is done for the Gulf Stream region in April (Fig. 34). This reinforces the notion that there is slightly more detail in (d) compared to (b), as the fields from the L3 model appear to be a bit more smoothed. Yet apart from that, all the same structures are found in both model fields.

The difference between the mean of the continuous dataset and the observations/collocated datasets is striking in this case. It is a clear case of taking the mean of a whole dataset compared to only a few snapshots. The different fronts are still recognisable in (b) and (d), indicated as a band of strong positive curl, but they are completely smoothed out in (c). It is a clear indicator why collocation is necessary for observation-model comparisons.

Finally, looking at the mean rotation fields of the complete ECMWF-Ops dataset (Fig. 34c), it can be seen that there are some rotation patterns visible over the Gulf Stream. The dual curl-band near the US East Coast as seen in the observations (Figs. 34a and 28a) is not present, but there seems to be a net negative rotation present. More strikingly, there is a clearly defined curl-band present over the Gulf Stream after detachment (between 35° and 40° N), with a negative northern side and a positive southern side. This indicates that there is some air-sea coupling present in the model, even though it is incomplete. This detached

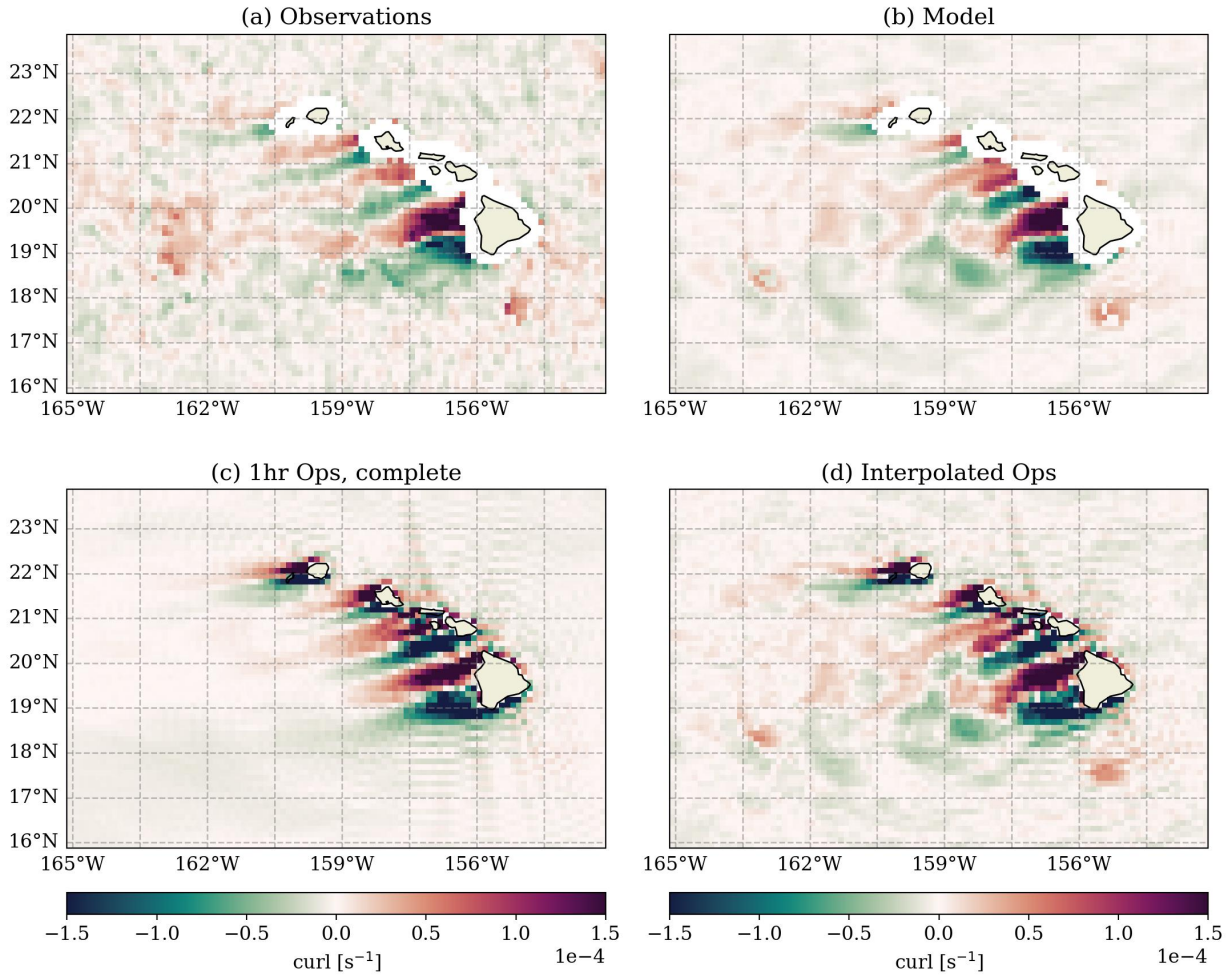

Figure 33: The July 2022 mean rotation fields near Hawaii. Observations (a) are from the descending orbit of MetOp-B. The other plots are the L3 collocated data (b), the complete ECMWF hourly model field (c) and the collocated ECMWF-Ops field (d).

part of the curl-band is not clearly visible in the observed fields, because they are obscured by the rotation of weather fronts which are formed over the storm track.

This concealment of that part of the Gulf Stream track is a result of a limit in the number of data points in one month. In the yearly mean rotation field (Fig. 40 in Appendix B), it is seen that the first 1000 km after the detachment of the Gulf Stream, the rotation band is still present, as is the large bias.

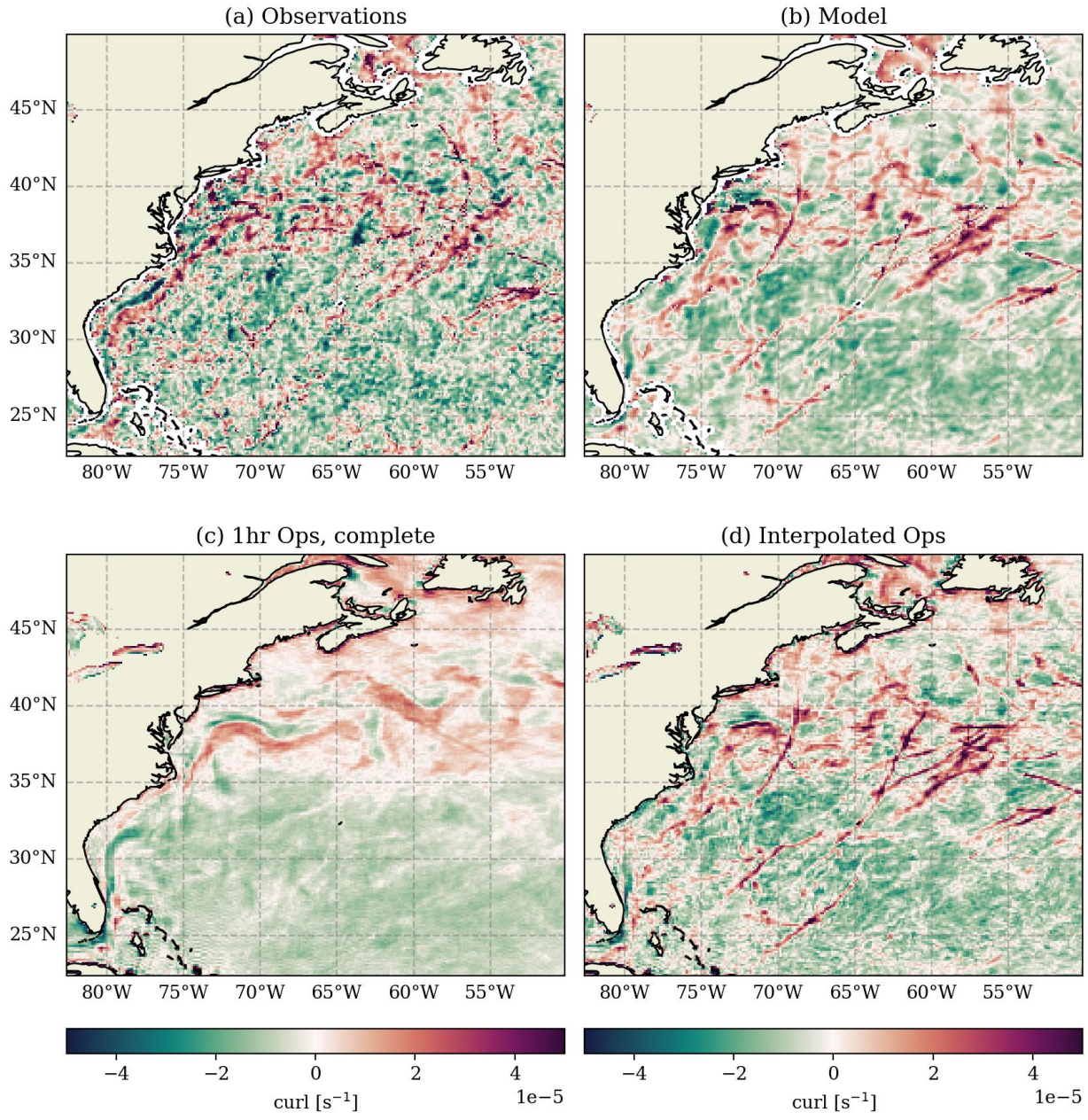

Figure 34: The April 2022 mean rotation fields for the Western North Atlantic. Observations (a) are from the descending orbit of MetOp-B. The other plots are the L3 collocated data (b), the complete ECMWF hourly model field (c) and the collocated ECMWF-Ops field (d).

5 Discussion

This study covers the intricacies of global and regional wind rotation and divergence patterns, measured by ASCAT and HSCAT scatterometers, as well as their bias with the ECMWF operational forecast model. Even though the availability of satellite wind observations is a huge step up compared to only using scarce in situ observations, there are still some limitations involved.

5.1 Limitations

The first thing to note is that the effective resolutions of ECMWF-Ops and ASCAT measurements are very different. This culminates into the large local variability in the global mean bias distributions of the wind rotation and divergence (Figs. 15e and 16e in Section 4.1.2). Similar variability is seen in the background of every other bias plot throughout this research. The smaller-scale motions (<100 km) are not effectively resolved by the model. This is to be expected, since modelled structures usually have to be at least a few grid cells in size, so with a grid cell size of 9 km this quickly leads to structures being at least one order of magnitude larger. Further improvement of the global forecast model resolution would help, but this is limited by the availability of computational power.

Another thing of note is that there are some significant differences between the HSCAT observations from the HY-satellites and the ASCAT observations from MetOp. ASCAT observations tend to show more variability, more extreme values and weaker correlations with model fields, while HSCAT is more in line with the model. These findings are also confirmed by Miguel Fernández [2023]. It is generally assumed for ASCAT observations to be the most accurate, since HSCAT's shorter wavelength means it has trouble looking through rainclouds, missing most of the extreme values in both wind divergence and rotation. This has as a result that even though the correlations between ASCAT and ECMWF-Ops are relatively low, their larger biases are of more importance for model validation than the biases resulting from HSCAT (which feels counterintuitive).

Furthermore, it should be noted that while satellite wind observations in this research are regarded as the most accurate reference, this is not always the case. The satellite measurements do have a small bias compared to in situ measurements, mainly buoy data. It should be mentioned though, that buoys are not perfect either and they also represent different spatial scales than scatterometer observations. In case of ASCAT on MetOp-C on a 0.25° resolution (observations from February-April 2019), the average wind speed bias compared to buoy data is 0.04 m/s, with a standard deviation in u and v of 1.51 m/s and 1.80 m/s respectively. [Verspeek et al., 2019] For the 0.125° resolution, the bias and standard deviations are even slightly larger: 0.08 m/s, 1.59 m/s and 1.89 m/s respectively. Similar values can be found for HSCAT in Verhoef et al. [2022], but in this case the buoy validation bias of the wind speed is negative and slightly stronger (-0.22 m/s for HY-2B, 0.25°, over Jan-Jun 2022), while the standard deviations are of a similar magnitude as for ASCAT. These wind speed biases indicate that ASCAT winds are slightly too strong, while HSCAT winds are slightly too weak compared in situ measurements, which would undoubtedly also influence the wind rotation and divergence fields.

Finally, the resolution differences between HSCAT and ASCAT probably also causes some differences in the results, especially in the wind rotation fields over the Gulf Stream. The rotation is calculated using the four nearest grid points and the effects of the air-sea coupling (negative/positive rotation of the wind field due to a positive/negative SST-gradient) can be very subtle. So, for the larger grid size of HSCAT, these deflections may be lost.

5.2 Further research

This study mainly focused on regional wind divergence and rotation biases during the month they were most significant. Yet, many of these atmospheric phenomena vary with the seasons. So, it would be interesting to study if these biases are seasonally dependent as well and if they are the same if conditions in two different months are similar.

Adding to that, it would be interesting to see if the air-sea coupling in the Gulf Stream area is also affected by seasonal variability. Given that the dual curl-band is present year-round, it would be interesting to study for what season/month it is strongest or if there are any differences between April and October, when the Atlantic is warming and cooling down respectively, or between summer and winter, when temperatures are at their peaks and lows.

Furthermore, this study focused on the model biases between scatterometer observations and the global operational forecasting model of ECMWF. Studying the biases between these observations and different (regional) models might lead to very different results, which could help with improving both the scatterometer calibrations and said models.

For the island wakes near Hawaii, it could be interesting to study the effects of a more accurate island-topography in the model on the wind wakes and if it resolves the slightly different orientation of the modelled wake.

Finally, concerning ECMWF-Ops, it could be investigated if the modelled divergence (or more specifically the modelled convergence) as well as the air-sea coupling could be improved. Since they are both present in the model, yet they usually are too weak or incomplete: wind divergence is weaker throughout and largely absent in Hawaii's wake, while the air-sea coupling is only present over the start of the detached part of the Gulf Stream.

6 Conclusions

The first conclusion that can be drawn is admittedly not one of the main goals of this research. Yet it can clearly be concluded that both ASCAT observations and NWP models (ECMWF-Ops versus ERA5 and ERA-Interim) have improved markedly with respect to the results of Belmonte Rivas and Stoffelen [2019].

On a global scale, the ASCAT biases in the wind rotation and divergence are relatively small. Apart from some local variability, the mean biases are on the order of 10 % of the observed field. For the wind rotation, the model fields are a little weaker around the mid-latitudes and a little stronger in the polar regions. The strongest global biases in the wind divergence fields are located near the areas of convergence: the ITCZ and the sub-polar low-pressure areas, indicating that global convergence is underestimated in ECMWF-Ops.

Eddy flows are also weaker in ECMWF-Ops, mainly resulting in positive eddy biases for both the global eddy divergence and rotation, further underlining that the NWP model shows less variability.

The first of the regions discussed is Madagascar, during the month October, where a turbulent wake is formed just off its northern tip. This strong wake with positive rotation, which is stronger in the model fields, resulting in a negative rotation bias. At the same time there is a net divergence at the tip, which is weaker in the model fields, yielding a small positive divergence bias.

The Tehuano Wind near Mexico over the month January is the second case that is discussed. Both, the wind rotation biases and divergence biases for the gap wind do not stand out in the surrounding bias. This indicates that the Tehuano Wind is well resolved in ECMWF-Ops, which is further reinforced by studying every individual observation from HSCAT and ASCAT at two specific locations. The coupling between the SST and air motions in the form of upwelling show some differences between measurements from AVHRR and model fields, but these are mainly in the spatial distribution and less so in the strength/magnitude.

For Hawaii in July, the third case, the wind phenomenon studied is a combination of turbulent island wakes and gap winds, which together manifested in the form of von Kármán vortex streets. ECMWF-Ops was well able to resolve these wakes, yet they are oriented slightly more westward compared to the observed wakes from ASCAT, resulting in some irregular bias patterns. These variations of the wake orientation are likely caused by the smoothing of the island topography in the model, allowing the winds to bend around the islands a little differently.

The divergence near the gaps between the islands, and the convergence at the center of each island wake, as seen in the observed fields, were not well represented in the model fields, resulting in some very large divergence biases on the lee-side of Hawaii.

Large temporal variability in both the wind divergence and rotation of the island wake makes the comparison between individual observations and model values very difficult. Especially the ASCAT-model correlation is low, yet the monthly mean values are very similar.

The final case, the Western North Atlantic, shows the most notable bias on the global scale. This bias is present throughout the year, but the focus lies on April. Over the Gulf Stream, where it is still attached to mainland America, there is a very clear dual curl-band formed, with strong negative rotation on the west-side and strong positive rotation on the east-side. These patterns are seen in the ASCAT observations, but not in the model fields, resulting in a large bias over the Gulf Stream.

This curl-band is formed due to small adjustments a wind vector makes when it passes over a gradient in the sea surface temperature, inducing a negative rotation when it passes from colder waters to warmer waters, and a positive rotation passing from warmer to colder waters. This air-sea coupling could be missing in the model fields because the SST-field is notably different, but after comparing the SST-fields and gradients from AVHRR observations with ECMWF fields, it was proven that this is not the case. It can thus be concluded that these air-sea interactions are not fully resolved in ECMWF's operational model. They are partly, however, since this band does show up in the mean rotation field of the complete ECMWF-Ops forecast for the month April, but only for the first 1000 km after detachment from the continent.

Stronger convergence and divergence is also found over this detached part of the Gulf Stream, which is commonly known as the North Atlantic Storm Track. Apart from some slightly weaker model fields, which are smoothed as well, there are no significant divergence biases in this region for the month April.

Correlations between ASCAT observations of MetOp-C and their collocated model fields for the focus months are relatively low. There is a lot of variability between weak/moderate correlation and anticorrelation. Yet for the areas of interest, the strong island wake behind Hawaii and Madagascar, the turbulent outflows of the Tehuano wind and the weather fronts in the North Atlantic, the correlations are strong. For some reason, the island wakes correlate more strongly during the morning, while the rotation of the Tehuano Wind correlates more strongly during the evening. For the Western North Atlantic, correlations are similar throughout the day.

Finally, the effects of different collocation schemes were tested for wind rotation observations of MetOp-B's descending orbit. The model fields that were collocated during the L2 phase of the wind product (which has undergone one temporal and two spatial interpolation steps) is compared with model fields that were collocated for this project (one spatial and one temporal interpolation, since they were already on the same grid as the observations). The resulting fields are very similar for both collocated models, with the model from the L3 product being a little more smoothed, as is expected with one more interpolation included. It can be concluded that less interpolation steps will result in more accurate/sharper collocated fields, but that the differences in this case are minimal. Including the temporal mean of the complete hourly ECMWF-Ops forecast shows the importance of collocation, since these fields are very different compared to both the observations and the collocated model fields.

Acknowledgements

First of all, I would like to thank my daily supervisor at KNMI, Rianne Giesen, for her guidance and support during my internship, for helping me get acquainted in the field of scatterometry and for including me in the KNMI-trip to Zuid-Limburg. I very much enjoyed my time working at KNMI.

Also, I would like to thank Ad Stoffelen and Michiel Baatsen for their many helpful tips and suggestions, given during our monthly meetings.

Lastly, many thanks to Daniëlle Bintanja and Nick Romijn, who gave this thesis a once over and pointed out many pesky typos I certainly would have missed, and to my parents, for always supporting me and giving me the opportunity to follow my own path.

Bibliography

M. Belmonte Rivas and A. Stoffelen. Characterizing era-interim and era5 surface wind biases using ascat. *Ocean Science*, 15(3):831–852, 2019. doi: 10.5194/os-15-831-2019. URL https://os.copernicus.org/articles/15/831/2019/.

BoM-AG. Frontal systems, 2021. URL http://www.bom.gov.au/climate/about/australian-climate-influences.shtml?bookmark=fronts. Accessed: 2024-07-08.

C3S. Sea surface temperature daily data from 1981 to present derived from satellite observations., 2024. Accessed: 2024-03-25.

L. Cavaleri, M. Bajo, F. Barbariol, M. Bastianini, A. Benetazzo, L. Bertotti, J. Chiggiato, C. Ferrarin, F. Trincardi, and G. Umgiesser. The 2019 flooding of venice and its implications for future predictions. *Oceanography*, March 2020. URL https://doi.org/10.5670/oceanog.2020.105.

C. Cenedese and A. L. Gordon. ocean current - encyclopedia britannica, 2024. URL https://www.britannica.com/science/ocean-current. Accessed: 2024-06-05.

S. Dunlop. *Weather, A Very Short Introduction*. Oxford University Press, Oxford, 1 edition, 2017.

DWD. Numerical weather prediction models, 2018. URL https://www.dwd.de/EN/research/weatherforecasting/num_modelling/01_num_weather_prediction_modells/num_weather_prediction_models_node.html. Accessed: 2024-06-11.

ECMWF. Implementation of ifs cycle 47r3, 2023. URL https://confluence.ecmwf.int/display/FCST/Implementation+of+IFS+Cycle+47r3.

ESA, 2020. URL https://www.esa.int/Enabling_Support/Space_Transportation/Types_of_orbits. Accessed: 2024-05-28.

EUMeTrain. Tutorial on satellite derived wind products - chapter 2, 2017. URL https://resources.eumetrain.org/data/4/438/print_2.htm#header. Accessed: 2024-06-05.

D. E. Hitzl, Y.-L. Chen, and H. V. Nguyen. Numerical simulations and observations of airflow through the alenuihāhā channel, hawaii. *Monthly Weather Review*, 142(12):4696 – 4718, 2014. doi: 10.1175/MWR-D-13-00312.1.

J. Miguel Fernández. Ocean surface wind properties of different scatterometer observation types and numerical weather prediction model fields. Master's thesis, Utrecht University, 6 2023.

G. W. K. Moore. Impact of the high topography of madagascar on the structure of the findlater jet. *Geophysical Research Letters*, 40(10):2367–2372, 2013. doi: https://doi.org/10.1002/grl.50399.

NASA. Data processing levels - earth data, 2021. URL https://www.earthdata.nasa.gov/engage/open-data-services-and-software/data-information-policy/data-levels. Accessed: 2024-06-16.

A. Nekrasov, A. Khachaturian, E. Abramov, O. Markelov, and M. Bogachev. On sea ice measurement by a c-band scatterometer at vv polarization: Methodology optimization based on computer simulations. *Remote Sensing*, 11:2518, 10 2019. doi: 10.3390/rs11212518.

NOAA-NCEI. Etopo 2022 15 arc-second global relief model, 2022. Accessed: 2024-03-25.

Offshore123. Map of large-scale surface currents, 09 2021. URL https://www.offshoreengineering.com/oceanography/map-large-scale-surface-currents/.

OSI SAF. Product user manual for global ocean l3 wind, 11 2022.

L. W. O'Neill, D. B. Chelton, and S. K. Esbensen. The effects of sst-induced surface wind speed and direction gradients on midlatitude surface vorticity and divergence. *Journal of Climate*, 23(2):255 – 281, 2010. doi: 10.1175/2009JCLI2613.1. URL https://journals.ametsoc.org/view/journals/clim/23/2/2009jcli2613.1.xml.

M. W. Santiago-García, A. F. Parés-Sierra, and A. Trasviña. Dipole-wind interactions under gap wind jet conditions in the gulf of tehuantepec, mexico: A surface drifter and satellite database analysis. *PLOS ONE*, 14(12):1–23, 12 2019. doi: 10.1371/journal.pone.0226366. URL https://doi.org/10.1371/journal.pone.0226366.

D. Smith. Tracing the tehuano. *Sensing our Planet*, pages 38–41, 2015.

S. Soisuvarn and S. Oudomying. Characterization of the tropical cyclones wind radii in the north western pacific basin using the ascat winds data products. In *2018 Progress in Electromagnetics Research Symposium (PIERS-Toyama)*, pages 1428–1433, 2018. doi: 10.23919/PIERS.2018.8597959.

A. Stoffelen. *Scatterometry*. PhD thesis, Utrecht University, 1998.

H. Tange. Thermohaline circulation of the oceans, 2020. URL http://www.coastalwiki.org/wiki/Thermohaline_circulation_of_the_oceans. Accessed: 2024-06-20.

E. E. Tsartsali, R. J. Haarsma, P. J. Athanasiadis, A. Bellucci, H. de Vries, S. Drijfhout, I. E. de Vries, D. Putrahasan, M. J. Roberts, E. Sanchez–Gomez, and C. D. Roberts. Impact of resolution on the atmosphere–ocean coupling along the gulf stream in global high resolution models. *Climate Dynamics*, 58(2):3317–3333, 6 2022. doi: https://doi.org/10.1007/s00382-021-06098-9.

A. Verhoef, J. Verspeek, and A. Stoffelen. *Scientific Validation Report (SVR) for the HY-2 winds*, 11 2022.

J. Verspeek, A. Verhoef, and A. Stoffelen. *ASCAT-C wind product calibration and validation*, 11 2019.

K. von Schuckmann, P.-Y. L. Traon, N. S. (Chair), A. Pascual, S. Djavidnia, J.-P. Gattuso, and M. Grégoire. Copernicus marine service ocean state report, issue 5. *Journal of Operational Oceanography*, 14(sup1):1–185, 2021. doi: 10.1080/1755876X.2021.1946240. URL `https://doi.org/10.1080/1755876X.2021.1946240`.

K. Våge, R. Pickart, G. Moore, M. Ribergaard, and H. Davies. The greenland tip jet and its effect on the irminger sea, 2016. URL `https://rpickart.whoi.edu/wp-content/uploads/sites/53/2016/04/Poster_TheGreenlandTipJet.pdf`. poster.

Y. Yang, J. Ma, and S.-P. Xie. Observations of the trade wind wakes of kauai and oahu. *Geophysical Research Letters*, 35(4), 2008. doi: https://doi.org/10.1029/2007GL031742.

Y. Zhang, B. Mu, M. Lin, and Q. Song. An evaluation of the chinese hy-2b satellite's microwave scatterometer instrument. *IEEE Transactions on Geoscience and Remote Sensing*, 59(6):4513–4521, 2021. doi: 10.1109/TGRS.2020.3008405.

A Global distributions

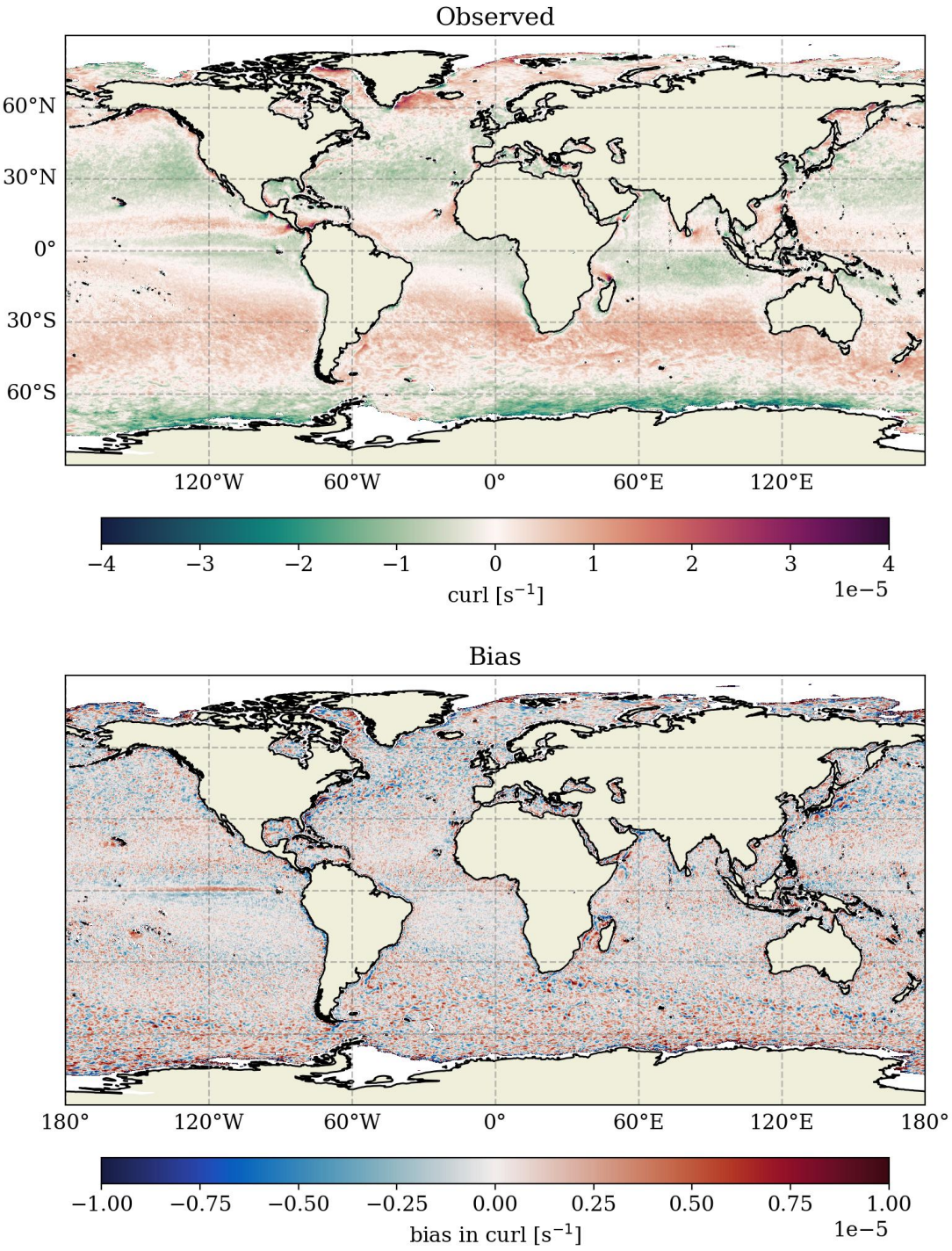

Figure 35: Spatial distribution of the 2022 mean MetOp-C wind curl observations (top, both orbits) and the corresponding bias with ECMWF model fields (bottom).

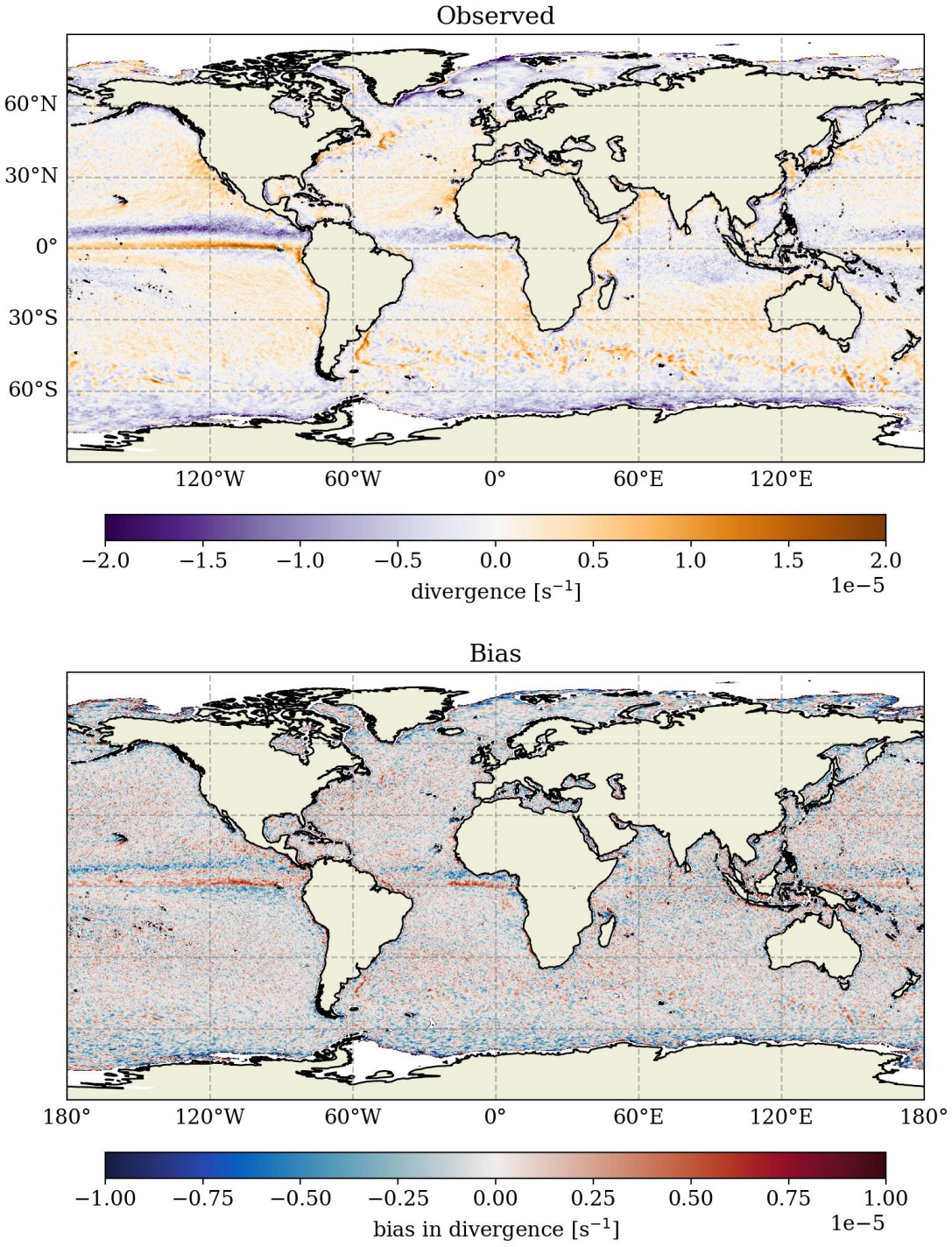

Figure 36: Spatial distribution of the 2022 mean MetOp-C wind divergence observations (top, both orbits) and the corresponding bias with ECMWF model fields (bottom).

B Regional yearly mean rotation fields

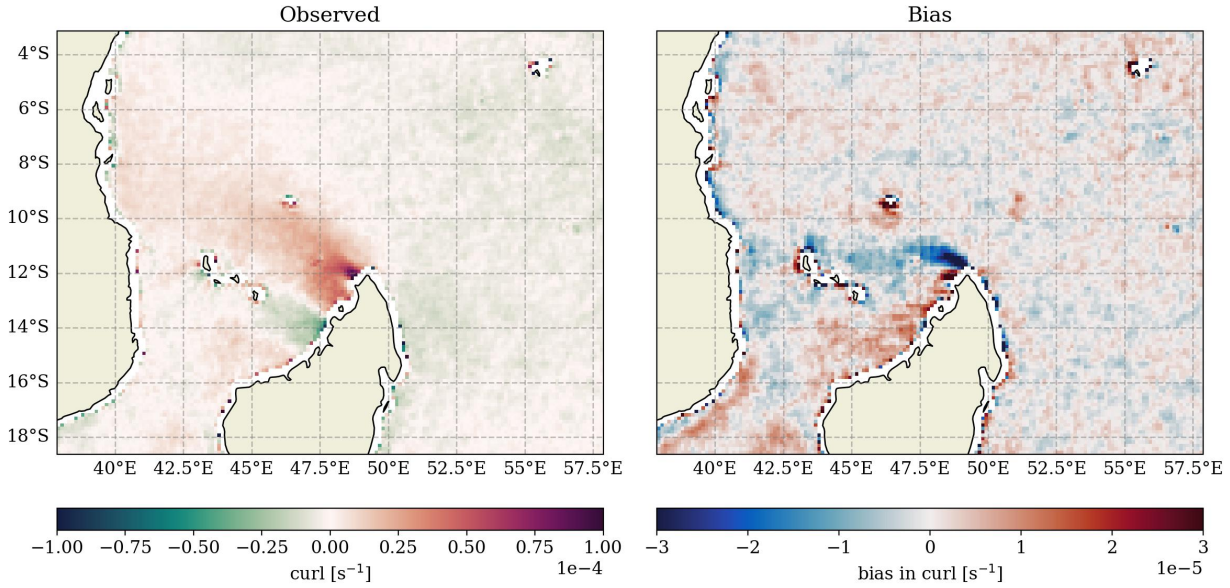

Figure 37: Yearly mean rotation fields and biases for 2022 for the region around North Madagascar. Observations originate from ASCAT measurements of both the ascending and descending orbits of MetOp-B and -C.

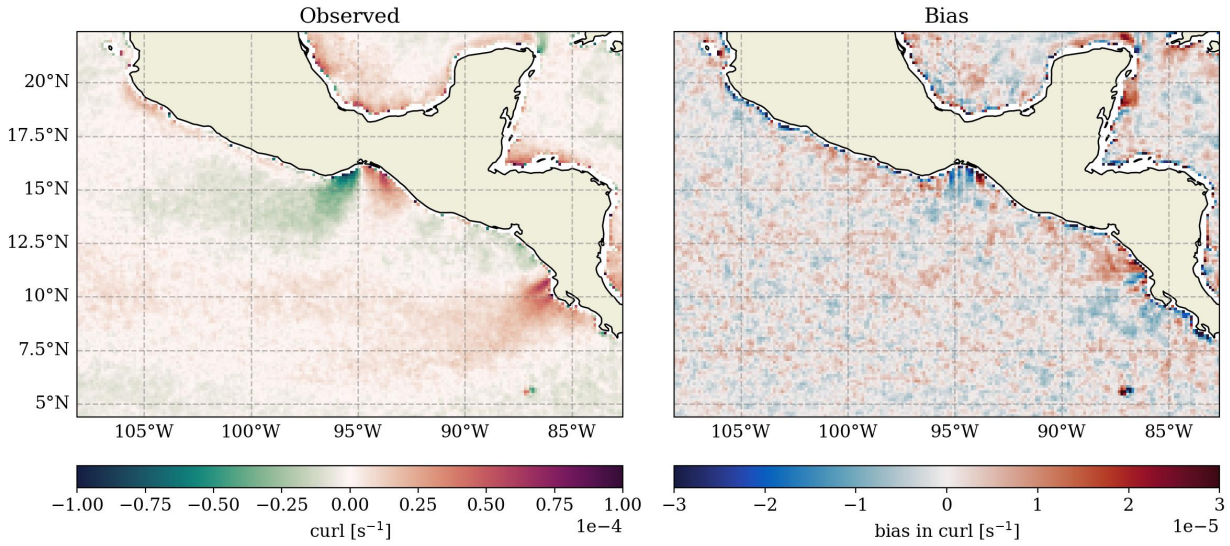

Figure 38: Yearly mean rotation fields and biases for 2022 for the Pacific Ocean south of Mexico. Observations originate from ASCAT measurements of both the ascending and descending orbits of MetOp-B and -C.

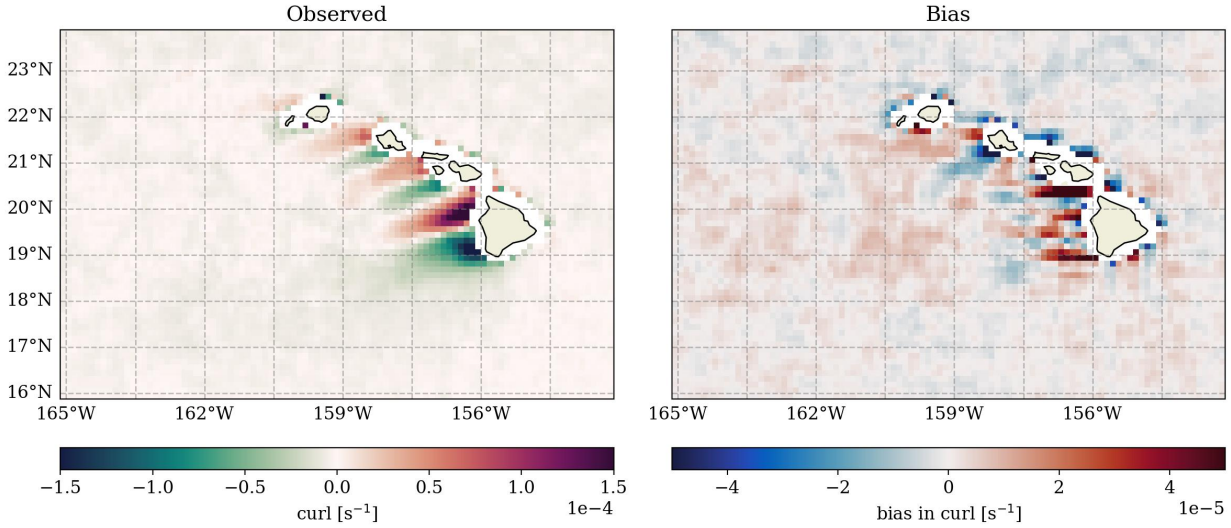

Figure 39: Yearly mean rotation fields and biases for 2022 for the region around Hawaii. Observations originate from ASCAT measurements of both the ascending and descending orbits of MetOp-B and -C.

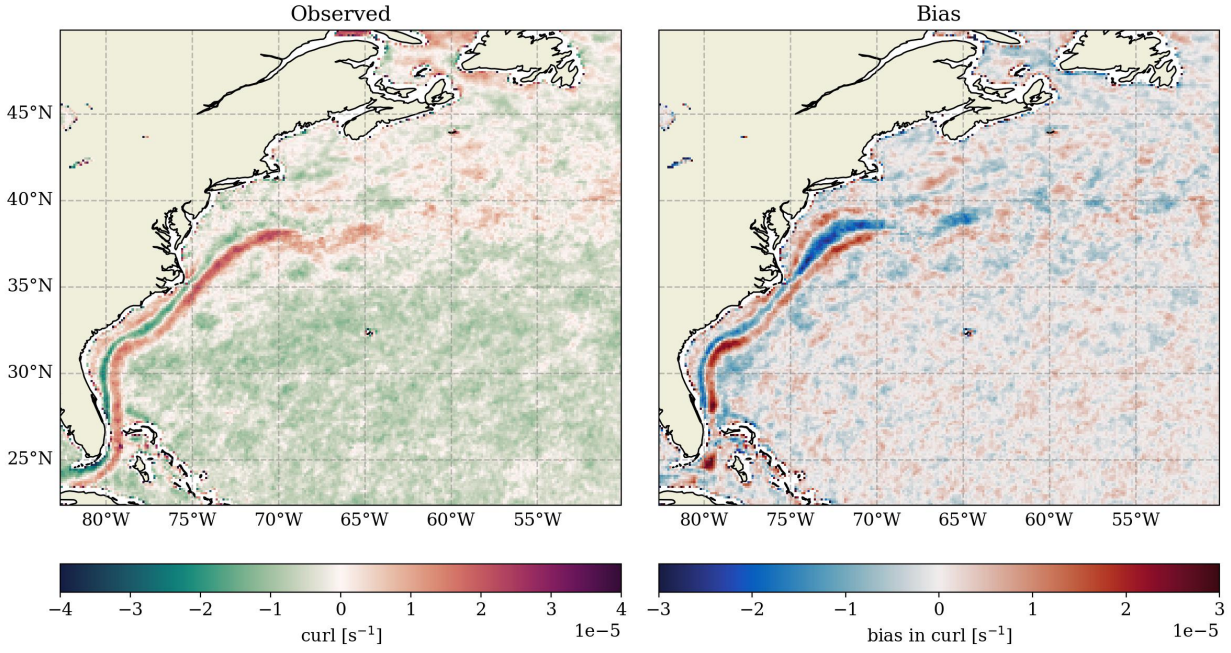

Figure 40: Yearly mean rotation fields and biases for 2022 for the Western North Atlantic. Observations originate from ASCAT measurements of both the ascending and descending orbits of MetOp-B and -C.

C Western North Atlantic: Valid data points

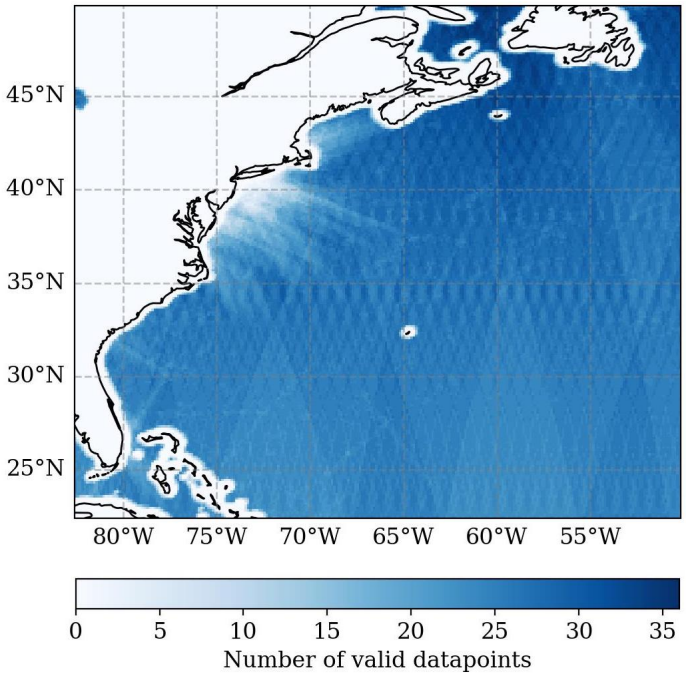

(a) MetOp-B

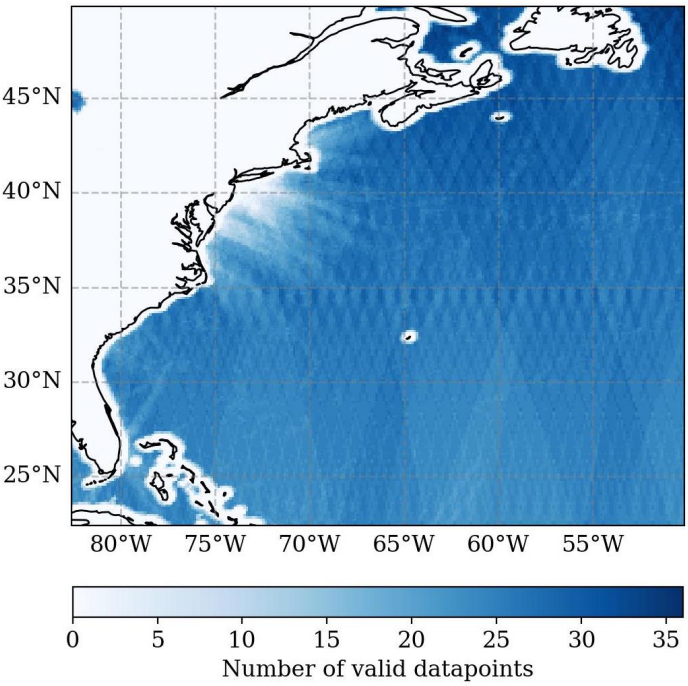

(b) MetOp-C

Figure 41: Number of valid data points from ASCAT measurements of the Western North Atlantic in April. The data represents the wind curl and encompasses both orbits of MetOp-B (a) and MetOp-C (b).

D Western North Atlantic: SST-gradient

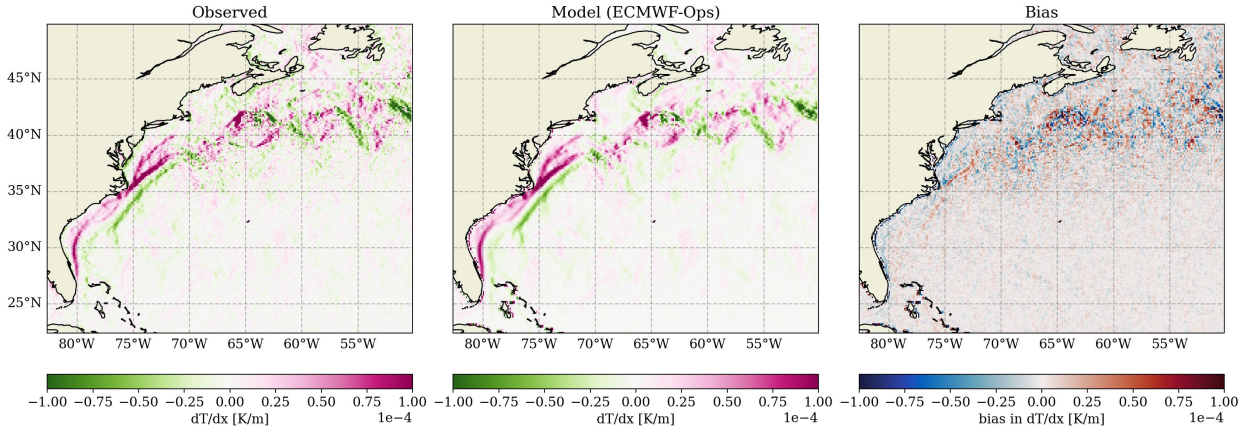

(a) dT/dx

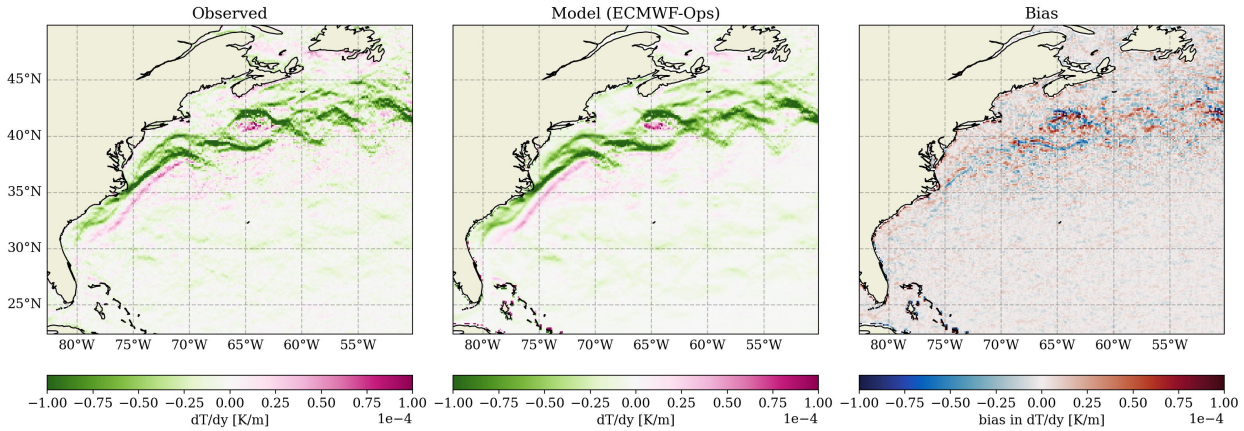

(b) dT/dy

Figure 42: The x- (a) and y-components (b) of the SST-gradient for the Western North Atlantic. The observations are measured by MetOp-B in the descending orbit and the SST-fields are the average of April 2022

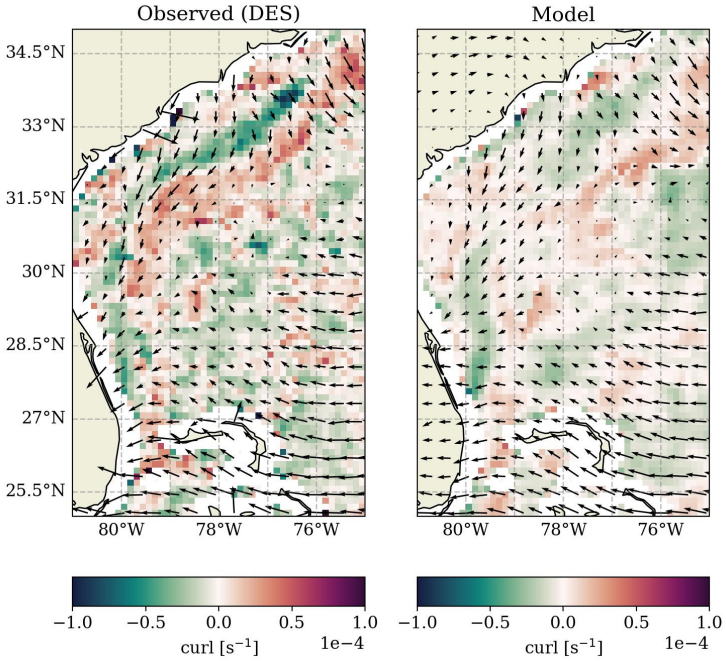

(a) vorticity and wind vector field

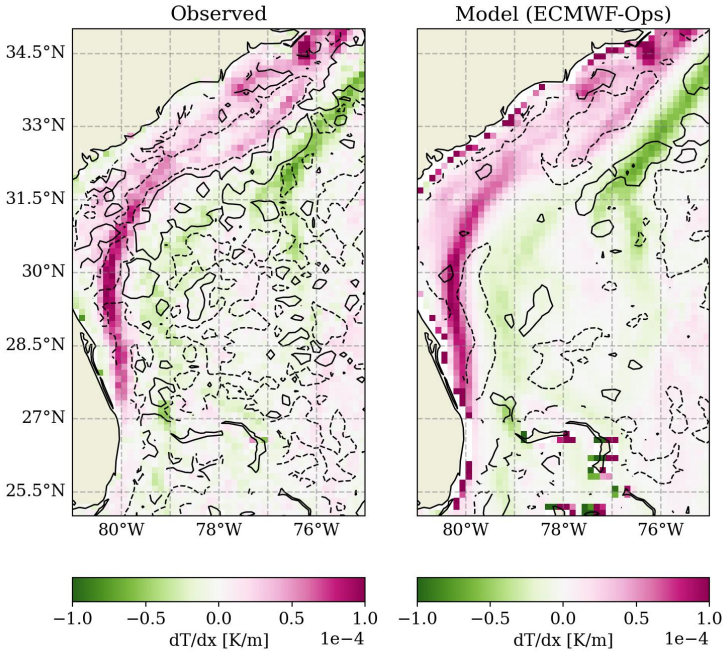

(b) $\partial T/\partial x$ and vorticity contours

Figure 43: Close-up of the lower part of the Gulf Stream. Observations from the descending orbit of MetOp-B versus the collocated model fields from the ECMWF-Ops. Subfigure (a) shows the mean rotation and the wind vector field, while (b) shows the mean zonal SST-gradient with vorticity contours at levels -1.2×10^{-5} s^{-1} (dashed) and 1.2×10^{-5} s^{-1} (solid).